



# Nanoscale spatially-resolved characterization of photovoltaic devices and materials

authored by

Abel Roigé Godia

A thesis submitted in fulfillment of the requirements  
for the award of the degree of Doctor of Philosophy  
in the Autonomus University of Barcelona

PhD Program in Materials Science and Technology

Bellaterra, December 2014



La present memòria es presenta per aspirar al grau de doctor i ha estat escrita per:

Abel Roigé Godia ,

sota la supervisió i direcció de:

Dr. Lourdes F. Vega

Dr. Ramon Alcubilla González ,

i sota la tutela de:

Dr. Javier Rodríguez Viejo

Bellaterra, 4 de decembre de 2014



*"I'd put my money on the sun and solar energy. What a source of power! I hope we don't have to wait until oil and coal run out before we tackle that."*

Thomas Alva Edison, in conversation with Henry Ford and Harvey Firestone, March 1931



# Agraïments

En primer lloc vull agrair a MATGAS i a la seva directora, la Dr. Lourdes Vega, per donar-me l'oportunitat de desenvolupar aquest treball, i per totes les facilitats i comoditats mostrades durant tot aquest temps.

També vull agrair al Dr. Ramon Alcubilla per haver confiat en les possibilitats d'aquesta col·laboració, i especialment per la seva atenció, ajuda i suport durant la part final d'aquest treball.

De forma molt especial vull agrair al Dr. Oriol Ossó tot el que m'ha ensenyat durant tots aquests anys. Gràcies per compartir amb mi tants coneixements i consells precisos, i sobretot, gràcies per haver-me guiat en els inicis de la meua etapa professional.

També voldria agrair la tasca desenvolupada per altres persones que han col·laborat en la realització d'aquest treball. En primer lloc al Dr. Mariano Campoy Quiles per compartir amb mi una col·laboració que va ser l'inici de tot plegat, i sobretot, pel seu tracte excepcionalment proper i natural. De forma molt especial, també vull agrair al Dr. Alejandro R. Goñi tota la seva ajuda durant aquests anys. Gràcies per mai haver tingut un no per resposta, i per tots els invaluables coneixements transmesos en totes i cadascuna de les reunions i discussions plegats.

De forma molt destacada també vull agrair i donar les gràcies a tots els col·laboradors del departament d'Enginyeria Electrònica de la Universitat Politècnica de Catalunya. Al Dr. Pablo Ortega, al Dr. Cristobal Voz i al Dr. Isidro Martín. Moltíssimes gràcies per dedicar-me tant temps i per compartir amb mi tantes mostres, tantes reunions i tantes correccions de manuscrits. Sense la vostra ajuda, aquest treball no hauria tirat endavant.

También quiero agradecer muy especialmente al Dr. José Alvarez y al Dr. Jean-Paul Kleider por darme la oportunidad de realizar una fantástica estancia de tres meses en el *Laboratoire de Génie Electrique de Paris*. José, gracias por

haberme dedicado tanto tiempo y por haberme facilitado tanto las cosas en París. Fueron tres meses que siempre recordaré.

I would also like to thank my office mates in the LGEP. Hakim, Baptiste, Amir, Sofia, Thomas and Oriol, thank you to make me feel so fine during my research stay. I am sure we will meet more times in the future.

També vull agrair als meus companys de MATGAS pel seu suport durant aquests anys. Aida, Emili, Sandra, Aurora, Pilar, gràcies per fer tot això una mica més fàcil, més proper i més humà.

I no em puc oblidar de tots els amics que he conegut durant aquest temps. Sense cap mena de dubte aquesta ha estat l'època més intensa i didàctica de la meva vida, i això ha estat així gràcies a vosaltres. Santi, Antoni, Pedro, Thomas, Gabriel, espero que estiguem on estiguem mai deixem de veure'ns i saber de nosaltres.

Gràcies també a la meva família. Als meus pares, al meu germà i a la meva germana. Tots ells, des de fa molt de temps, porten sent els responsables de la forma, intenció i caràcter del resultat obtingut en aquest treball.

I finalment, el que faltava per no poder oblidar mai aquests anys és haver-te conegut a tu. Gràcies Elena per tota la teva ajuda i per ensenyar-me cada dia allò que és veritablement important.



# Contents

<b>Contents</b>	<b>viii</b>
<b>1 Introduction</b>	<b>1</b>
1.1 Thesis objectives . . . . .	4
1.2 Thesis outline . . . . .	5
<b>2 Crystalline-Si photovoltaics</b>	<b>7</b>
2.1 Introduction . . . . .	8
2.1.1 Commercially produced c-Si solar cells . . . . .	9
2.1.2 Decreasing wafer thickness . . . . .	10
2.1.3 Passivated Emitter and Rear Cell (PERC) concept . . . . .	11
2.2 Surface passivation . . . . .	12
2.2.1 Description of bulk recombination mechanisms . . . . .	12
2.2.1.1 Radiative recombination . . . . .	14
2.2.1.2 Auger recombination . . . . .	15
2.2.1.3 Recombination via defects . . . . .	16
2.2.1.4 Dependence of the excess carrier density on life-time . . . . .	17
2.2.2 Surface recombination . . . . .	18
2.2.2.1 Surface Recombination Velocity . . . . .	19
2.2.2.2 Reduction of surface recombination . . . . .	20
2.2.2.3 Surface passivating materials . . . . .	22
2.2.3 Surface passivation by $\text{Al}_2\text{O}_3$ . . . . .	23
2.2.3.1 Origin of intrinsic negative charge . . . . .	25
2.2.3.2 Increase of passivation performance by annealing . . . . .	25
2.3 Laser-Fired Contact (LFC) approach . . . . .	26
2.3.1 Key features of Laser-Fired Contacts (LFCs) . . . . .	27
2.3.2 Considerations of LFCs formation . . . . .	29

2.3.3	Optimization of LFC . . . . .	29
2.3.3.1	Recombination at the laser-processed surface . .	30
<b>3</b>	<b>Characterization techniques</b>	<b>33</b>
3.1	Photoluminescence (PL) spectroscopy . . . . .	34
3.1.1	PL for the study of passivated c-Si . . . . .	34
3.1.1.1	Brief description about steady-state conditions .	34
3.1.1.2	Qualitative determination of passivation efficiency	35
3.1.1.3	Quantitative determination of lifetime . . . . .	36
3.1.2	Micro-PL spectroscopy . . . . .	36
3.1.2.1	Spatially-resolved carrier profiles in micro-PL experiments . . . . .	39
3.1.3	Low-temperature micro-PL spectroscopy . . . . .	44
3.1.3.1	Free-bound (FB) transitions . . . . .	44
3.1.3.2	Excitons . . . . .	45
3.2	Raman spectroscopy . . . . .	46
3.2.1	Fundamentals of Raman spectroscopy . . . . .	47
3.2.2	Raman spectrum of c-Si . . . . .	48
3.3	Scanning probe microscopies . . . . .	50
3.3.1	Kelvin Probe Force Microscopy (KPFM) . . . . .	51
3.3.2	Conductive atomic force microscopy . . . . .	53
3.4	Other characterization techniques . . . . .	53
3.4.1	Quasi-steady state photoconductance . . . . .	53
3.4.2	Capacitance-Voltage curves . . . . .	54
3.4.2.1	Oxide charge determination . . . . .	55
<b>4</b>	<b>Cross-sectional KPFM study of Al/SiO<sub>2</sub>/c-Si stacks</b>	<b>57</b>
4.1	Introduction . . . . .	58
4.2	Experimental details . . . . .	58
4.2.1	Materials and samples . . . . .	58
4.2.2	Measurement modes . . . . .	59
4.2.3	Equipment and measurement details . . . . .	60
4.3	Towards reaching the MOS interface . . . . .	60
4.3.1	Orientation-induced Si work function variations . . . . .	61
4.4	MOS cross-section SP map . . . . .	63
4.5	SP under a varying bias . . . . .	65
4.5.1	KPFM spectroscopy . . . . .	67
4.6	Chapter summary . . . . .	69

<b>5</b>	<b>Low-temperature micro-PL in Al<sub>2</sub>O<sub>3</sub>-passivated c-Si wafers</b>	<b>71</b>
5.1	Introduction . . . . .	72
5.1.1	Electron-Hole Liquid (EHL) . . . . .	72
5.2	Experimental methodology . . . . .	74
5.2.1	Materials and samples . . . . .	74
5.2.2	Measurement details . . . . .	75
5.2.3	Cooling procedure . . . . .	76
5.3	PL down to 40 K . . . . .	77
5.4	PL below 40 K . . . . .	78
5.4.1	Correlation between EHL PL intensity and passivation efficiency . . . . .	82
5.4.1.1	Al <sub>2</sub> O <sub>3</sub> charge density under illumination . . . . .	86
5.5	Chapter summary . . . . .	87
<b>6</b>	<b>High-resolution spatially-resolved characterization of LFCs</b>	<b>89</b>
6.1	Introduction . . . . .	90
6.2	Local impact at the LFCs surroundings . . . . .	90
6.2.1	Experimental details . . . . .	91
6.2.1.1	Sample details . . . . .	91
6.2.1.2	Measurement procedure . . . . .	93
6.2.2	Impact of the laser pulse on the passivation layer . . . . .	94
6.2.2.1	Laser power dependence . . . . .	96
6.2.2.2	Laser wavelength dependence . . . . .	97
6.2.2.3	SiC <sub>x</sub> capping layer influence . . . . .	98
6.2.3	Impact of the laser pulse on the c-Si bulk . . . . .	101
6.2.4	Estimation of passivation performance reduction . . . . .	103
6.2.5	Effective surface recombination velocity at the laser-processed surface . . . . .	105
6.3	Doping profiles in laser-fired contacts . . . . .	107
6.3.1	Experimental methodology . . . . .	108
6.3.1.1	Materials and samples . . . . .	108
6.3.1.2	Equipment details . . . . .	108
6.3.2	Characterization by micro-Raman spectroscopy . . . . .	109
6.3.2.1	Doping profiles . . . . .	109
6.3.2.2	Vertical XZ Raman maps . . . . .	112
6.3.2.3	Crystalline fraction of LFCs . . . . .	114
6.3.2.4	Doping level quantification . . . . .	115

6.3.2.5	Induced stress at the laser processed region . . .	117
6.3.3	Doping profiles studied by micro-PL . . . . .	119
6.3.4	LFCs characterized by C-AFM measurements . . . . .	122
6.4	Chapter summary . . . . .	125
<b>7</b>	<b>Conclusions and future work</b>	<b>127</b>
7.1	Conclusions . . . . .	127
7.1.1	Kelvin Probe Force Microscopy . . . . .	127
7.1.2	Low-temperature micro-PL . . . . .	128
7.1.3	Micro-PL for the study of LFCs . . . . .	128
7.1.4	Micro-Raman for the study of LFCs . . . . .	129
7.2	Future work . . . . .	129
	<b>Bibliography</b>	<b>130</b>
<b>A</b>	<b>Surface vs bulk phase transitions in organic PV thin films</b>	<b>145</b>
A.1	Introduction . . . . .	146
A.1.1	Semiconducting properties . . . . .	146
A.1.2	Morphology: the key feature . . . . .	147
A.1.3	Post-deposition annealing treatments . . . . .	148
A.1.4	Geometric confinement . . . . .	148
A.1.5	Aim of the study . . . . .	149
A.2	Methodology . . . . .	150
A.2.1	Sample preparation . . . . .	150
A.2.2	Experimental techniques . . . . .	151
A.2.2.1	Temperature-dependent AFM . . . . .	151
A.2.2.2	Temperature-dependent micro-Raman . . . . .	152
A.3	PFO films phase transition . . . . .	153
A.4	P3HT:PCBM blend films phase transition . . . . .	155
A.5	Appendix summary . . . . .	161
	<b>Bibliography</b>	<b>163</b>
	<b>List of publications</b>	<b>167</b>
	<b>List of acronyms</b>	<b>169</b>
	<b>List of symbols</b>	<b>173</b>

# 1

## Introduction

In a World where energy demands associated to living standards are steadily increasing over the years, and the high concentrations of Green House Gases (GHGs) in the atmosphere present a serious threat to the health, prosperity, and stability of human communities [1], the use of sustainable energy sources must be considered a vital necessity.

Solar photovoltaic (PV) systems represent a sustainable and clean source of power generation, which can be applied in both residential and industrial infrastructures. An illustrative measure of the potential of solar energy is obtained as follows [2]: The World current energy consumption is  $4.1 \times 10^{20}$  Joules/year, which is equivalent to a continuous power consumption of 13 TW. Thus, considering that the earth surface receives an average of 120000 TW from the sun, the entire global energy needs can be satisfied covering 0.16 % of earth surface with solar panels with 10% efficiency.

The wide variety of solar cell technologies are commonly divided into three main families: 1) 1<sup>st</sup> generation solar cells are mainly based on crystalline-silicon (c-Si) wafers, whether single- or multi-crystalline. This is the most common and mature technology, and efficiency of current c-Si PV panels has reached values above 20%. 2) 2<sup>nd</sup> generation solar cells are presented in form of 1-2  $\mu\text{m}$ -thick films and avoid the use of silicon wafers. The combination of

using less material and lower cost manufacturing processes allows to produce panels at a much lower cost. However, their efficiency (10-15 %) is lower than 1<sup>st</sup> generation solar cells. Typically, amorphous silicon (a-Si), Cadmium Telluride (CdTe), and Copper Indium Gallium Selenide (CIGS) are the main solar cells considered in this category. 3) 3<sup>rd</sup> generation solar cells are made from a variety of new materials besides silicon and may include novel nano-structures such as nanotubes, nano wires and quantum dots. One interesting example in this category are organic PV (OPV) cells, which are deposited from solution and exhibit interesting properties like low-cost and flexibility.

As shown in Figure 1.1, the global PV capacity has shown an exponential growth during the last years. This growth is projected to continue until reaching values of 4600 GW of installed PV capacity by 2050 [3]. By far, global PV market is currently dominated by 1<sup>st</sup> generation c-Si modules, and the reduction of production costs can be considered one of the key reasons of the significant growth of PV capacity over the last years. In particular, the cost of PV modules has been divided by five in the last six years.

In order to expand this position and to improve the competitiveness of solar technology in front of other energy production alternatives, the generation cost of solar electricity must reach grid parity. This is, the net amortized cost for the production of solar electricity must be equal to the price of electricity generated

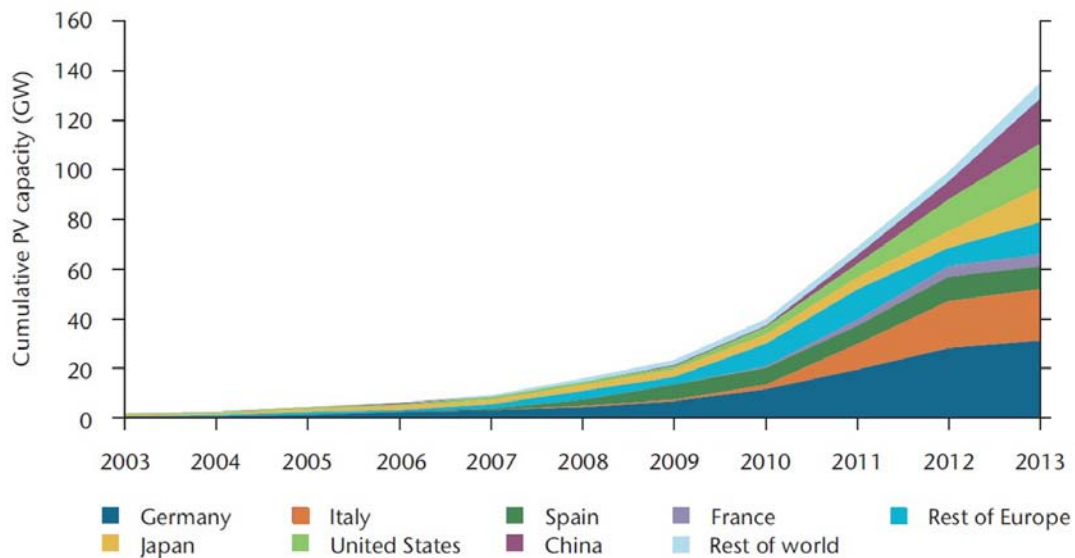


**Figure 1.1:** Global cumulative growth of PV capacity from 2003 to 2013 [3].

---

by today's conventional sources. In order to achieve this goal, the cost per produced watt ( $\text{€}/W_p$ ) must be further reduced. Hence, in parallel with the reduction of production costs, the increase in PV modules efficiency also plays an important role.

During the last years, PV technology has experienced an important evolution, resulting in the design of more complex and efficient architectures. In this context, material and device characterization becomes an important task not only for quality control in an expanding industry, but also remains at the very heart of further technological progress. This scenario is clearly captured by Figure 1.2. In this figure we represent the number of scientific publications during the last years that, in addition to the term 'solar cell', contain other words like 'characterization', 'Atomic Force Microscopy (AFM)' or 'high resolution', in their title or abstract. As we can observe, a steadily increase of scientific works during the last years have been focused on solar cell characterization.

In addition, since ultimate PV technologies are based on thinner architectures and smaller structures, also high-resolution characterization techniques such as AFM, which can be considered the workhorse technique of high-resolution microscopies, are progressively getting more importance in the sci-

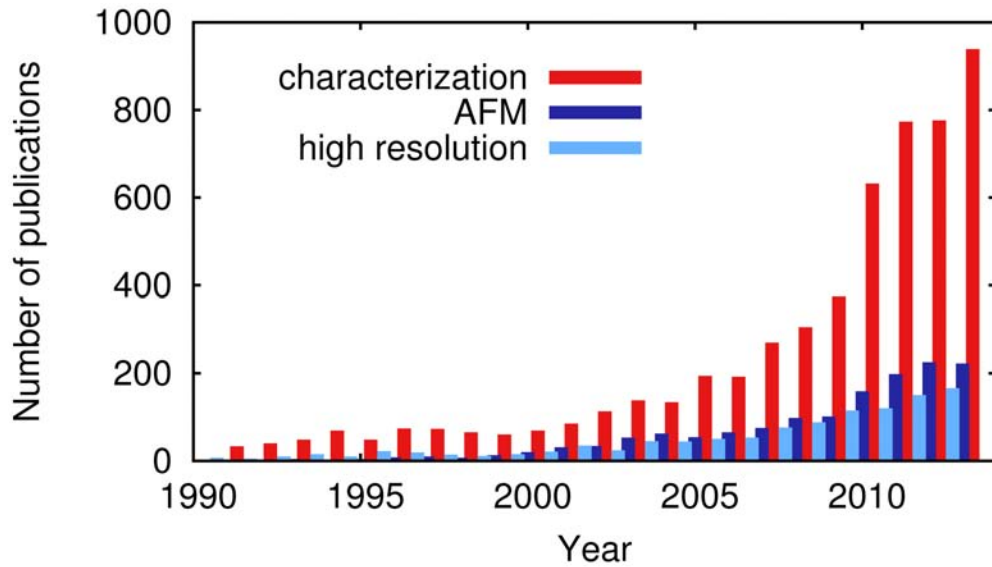


**Figure 1.2:** Number of publications from 1990 that in addition to the term 'solar cell', contain other words like 'characterization', 'AFM' or 'high resolution' in their title, abstract or key word list.

entific production in the PV field.

The effects and results of this increased number of scientific works are evident. For instance, in the case of c-Si, the recent and tremendous evolution in PV technology has lead to achieve efficiencies up to 25% [4], which are closer to the theoretical limit, i.e. 29.8% [5]. In this sense, the study of PV materials and devices by novel and advanced experimental techniques should be also considered the base of further technological progress of less-mature solar cell technologies.

## 1.1 Thesis objectives

This Thesis is focused on the application of advanced characterization techniques such as scanning probe microscopies, or micro-Raman and micro- photoluminescence spectroscopies to carry out a detailed and comprehensive study of PV materials and devices. The high-resolution and spatially-resolved capabilities of these techniques, allow us to obtain unique and exclusive information of material properties and device operation, which can not be deduced by other conventional (macroscopic) techniques. Thus, the obtained information will help to determine some key insights for the improvement and optimization of the studied PV devices.

The work is mainly focused on the study of two specific parts of current p-type c-Si solar cell architectures:

- rear passivation layer: In this case, the experiments are focused on studying the properties of the dielectric/silicon interface.
- laser-processed rear local base contacts: Here, we study two important features of the laser-processed contacts. First, we evaluate the impact of the laser processing on the passivation layer. Second, we characterize the properties of the highly-doped regions created below the contacts.

Additionally, in the appendix of this work, the same characterization techniques are nimbly applied for the study of micro-structural properties of organic PV (OPV) thin films. With this, we intend to demonstrate the versatility of the different experimental tools used in this Thesis.



## 1.2 Thesis outline

In Chapter 2, some of the most important features about the operation principles of c-Si solar cells are introduced. Emphasis has been put on two specific parts of PV devices that are of interest for this work: 1) the rear surface passivation layer and 2) the rear local point contacts, the so-called Laser-Fired Contact (LFCs).

In Chapter 3, the different characterization techniques used in this Thesis are presented. Special importance has been given to those features and peculiarities which make these techniques suitable tools to obtain unique and valuable information about PV devices and materials.

Chapter 4 and Chapter 5 are focused on the study of rear passivation layers employed in p-type solar cells. In Chapter 4, we use Kelvin Probe Force Microscopy (KPFM) to perform a high-resolution spatially-resolved study of the potential profile across the Metal-Oxide-Semiconductor (MOS) structure we can found at the rear side of many solar cells. On the other hand, in Chapter 5, we present a low-temperature micro-Photoluminescence (PL) spectroscopy study of  $\text{Al}_2\text{O}_3$ -passivated c-Si wafers.

Chapter 6 presents an extensive and exhaustive study of local base contacts typically used in the rear side of p-type c-Si solar cells. In particular, their characterization by micro-Raman and micro-PL spectroscopies with lateral resolutions down to  $1\text{ }\mu\text{m}$ , has allowed us to obtain for the first time unique and relevant information about specific key features of LFCs.

In Chapter 7, the most important conclusions concerning the characterization of c-Si devices are summarized.

Finally, in the appendix A, we present our study on organic thin films. As introduction, in the first part to the appendix, the most important peculiarities of OPV systems are introduced and compared with inorganic PV (IPV) systems.



# 2

## Crystalline-Si photovoltaics

*In this chapter, some important concepts concerning the operation principles of crystalline-Si (c-Si) solar cells are introduced. The goal is to give to the reader an useful conceptual background that will serve to understand the studies and results presented in this thesis. In the first section, important c-Si solar cells technologies such as the screen-printed solar cell and the Passivated Emitter an Rear Cell (PERC) concepts are addressed. This will serve as an introduction to the different fundamental parts of a c-Si solar cell, as well as to present the importance of surface passivation to develop high-efficiency c-Si solar cells. In the second section, the different recombination losses that can be present in a c-Si solar cell are reviewed, and also, the different available strategies to reduce such recombination losses. In particular, we focus on the use of  $\text{Al}_2\text{O}_3$  passivation layers. Finally, in the third section, we introduce the most important features of the Laser-Fired Contact (LFC) approach which is one of the most promising alternatives to develop base local contacts through the rear passivated surface of PERC solar cells.*

## 2.1 Introduction

Crystalline-silicon (c-Si) photovoltaics is the working horse of the photovoltaic market since their invention in the 1950's. Nowadays, c-Si solar cells represent by far the largest share to the World's Photovoltaic (PV) facilities, reaching up to 90% of the World's PV market for terrestrial applications [6].

The raw and most basic structure of a c-Si solar cell is based on the junction of a p-type and a n-type c-Si layer, the so-called p-n junction. Basically, a p-n junction is obtained by the diffusion of dopant atoms through one of the surfaces of a base c-Si wafer. Thus, phosphorous is usually used for creating n+ zones in p-type c-Si wafers, whereas Boron is employed for creating p+ regions in n-type c-Si wafers.

Three main processes take place in a solar cell for converting solar energy into electricity. These are: 1) absorption of photons and generation of electron-hole pairs, which at room temperature are immediately separated by the effect of thermal energy, 2) collection of photo-generated minority carriers (electrons in the p-type layer and holes in the n-type layer) by the p-n junction, and conversion to majority carriers by the effect of the p-n junction built-in electric field, and finally 3) movement of carriers towards their respective electrodes. Taking these processes into consideration, as depicted in Figure 2.1, the most

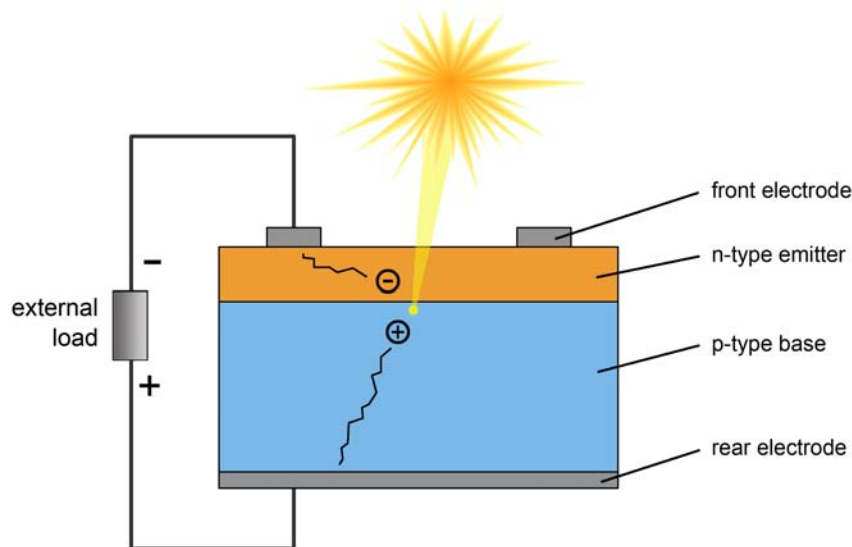


**Figure 2.1:** Sketch showing a cross-section of the basic structure of a c-Si solar cell. This is, front electrode/p-n junction/rear electrode.

## 2.1. Introduction

---

basic structure that is required in a c-Si solar cell is the following: electrons electrode/n-type c-Si layer/p-type c-Si layer/holes electrode. Starting from this basic solar cell scheme, commercially-available solar cell concepts show much more complex structures with a significant increase in the number of layers. The main goal of these complex cell architectures is to increase the device conversion efficiency. Some of these solar cell structures are introduced in the following sections.

### 2.1.1 Commercially produced c-Si solar cells

Among the large number of different solar cell concepts, the so-called screen-printed solar cells, have been one of the most used alternatives. This cell concept was developed in the 1970's and has dominated the terrestrial PV market in the last three decades. Since costs reduction has been always considered a paramount requirement for PV manufacturers, the low fabrication cost of this cell structure associated to a simple structure and a technologically feasible fabrication process, can be considered one of the most important reasons for the commercial success of the screen-printed c-Si solar cells.

Figure 2.2 shows a scheme of a standard screen printed p-type c-Si solar cell [7]. Its key features are the following: concerning the front side it features a surface textured highly doped  $n^{++}$  emitter coated by a silicon nitride ( $\text{SiN}_x$ ) films that acts as Anti-Reflection (AR) and passivation coating. Screen-printed metal grids are used as front electrode. Concerning the back side of the cell,

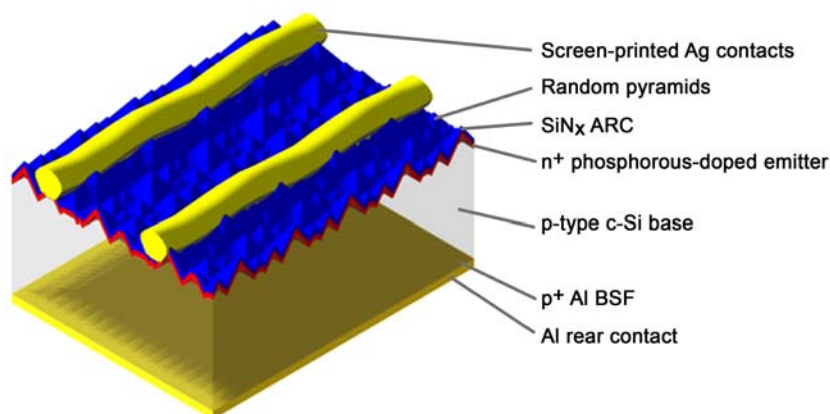


**Figure 2.2:** Scheme representing the structure and different parts of a screen-printed solar cell [7].

a complete Al film is screen-printed onto the back c-Si base. The cell is subsequently fired to enable the alloying of Al with c-Si. This creates a p+ Al-doped Si region below the back surface, which induced back surface passivation by the so-called Back-Surface Field (BSF) mechanism [8]. The BSF passivation is a key feature of the screen-printed solar cell concept.

### 2.1.2 Decreasing wafer thickness

In order to improve the competitiveness of solar technology in front of other energy production alternatives, the total cost per produced watt ( $\text{€}/W_p$ ) must be reduced. This can be achieved by improving the energy efficiency conversion, as well as by reducing the production costs of the solar panels. As the cost of the c-Si wafer is an important part of the complete solar cell module cost, an immediate solution for reducing PV panel costs consists on reducing the thickness of the wafers used for producing solar cells. Moreover, the emergence during the last decades of new and advanced cutting techniques have greatly contributed to the use of thinner wafers as an effective solution to reduce production costs.

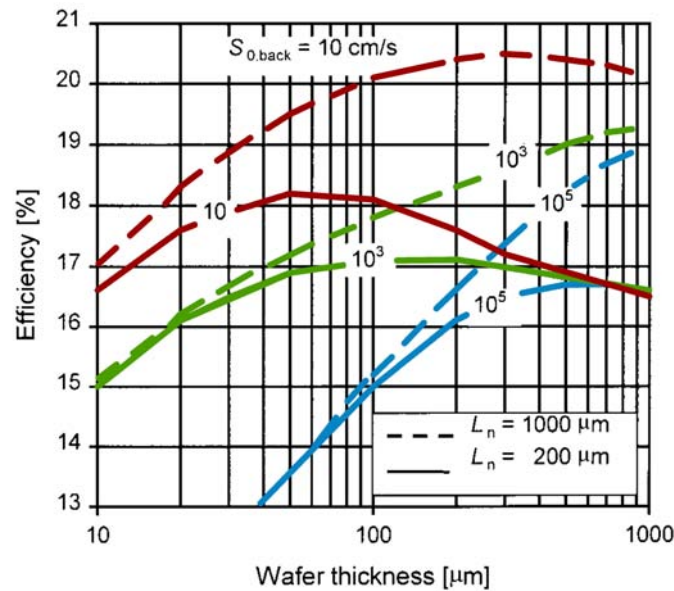


**Figure 2.3:** Simulated efficiencies at 1-sun as a function of the wafer thickness of an n<sup>+</sup>p c-Si solar cell. The influence of both the carrier diffusion length and the back surface recombination velocity is represented. Extracted from [9].

## 2.1. Introduction

---

For a long time, most of commercial c-Si solar cells were based on low-quality c-Si. In such devices, the conversion efficiency was limited by bulk recombination, hence, new and better strategies to reduce surface recombination were not required. However, by the progressive reduction of wafer thickness, the surface to volume ratio increased, and surface recombination started to limit the device conversion efficiencies. Thus, for solar cells based on thinner wafers, the use of high-performance surface passivation strategies is considered of paramount importance in order to achieve reasonable conversion efficiencies. Such scenario is clearly illustrated in Figure 2.3, where the efficiency at 1-sun for a n+p c-Si solar cell as a function of the wafer thickness [9] is depicted. As it can be observed, for solar cells with a thickness below 200  $\mu\text{m}$ , conversion efficiencies above 18% can only be achieved if recombination velocities at the back surface are in the range of 10 cm/s.

### 2.1.3 Passivated Emitter and Rear Cell (PERC) concept

The use of efficient rear passivation strategies is mandatory for the development of new high-efficiency solar cells structures. Among them, the so-called Passivated Emitter and Rear Cell (PERC) concept [10], and its improved version, the Passivated Emitter and Rear Locally diffused (PERL) cell [11], are the most promising alternatives as demonstrated by the fact that the current world record efficiency for c-Si solar cells has been achieved by a PERL structure [12]. Due to the presence of the back surface passivation layer, an important difference between these solar cells structures and the screen-printed solar cell concept (Section 2.1.1), is the necessity to create rear point contacts at the rear side with the aim to contact the metal electrode with the c-Si base throughout the back dielectric passivation layer. Figure 2.4 shows a scheme of a standard p-type PERC solar cell featuring local rear contacts. The key characteristics of this solar cell structure are the following: regarding the front side, the cell shows the same architecture than that observed by the screen-printed cell (Section 2.1.1). This is, a surface textured highly doped  $n^{++}$  emitter coated by a silicon nitride ( $\text{SiN}_x$ ) films and screen-printed metal grids that act as front electrode. Respect the back side, it features a rear surface passivation layer and an Al rear contact deposited onto the rear dielectric film. In addition, local base contacts are processed through the passivation layer in order to contact the rear Al electrode and the p-type c-Si base. Both, the rear surface passivation layer and the rear local contacts, are considered features of paramount

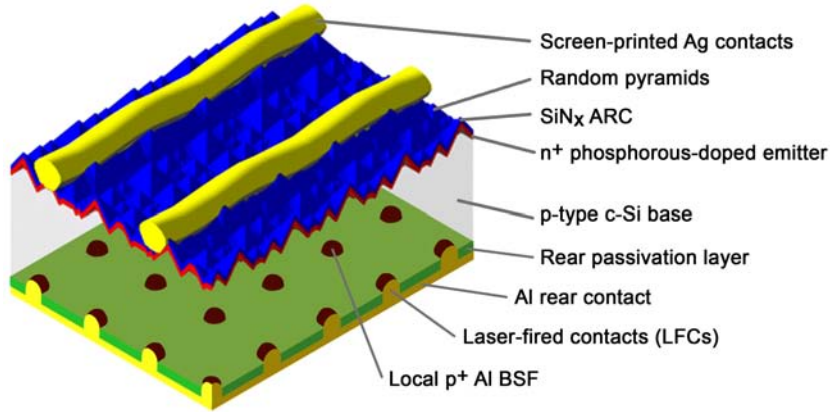


**Figure 2.4:** Scheme representing the structure of a PERC solar cell with rear local contacts processed by laser firing [7].

importance for the good operation of these promising solar cell structures. It is worth to mention that the detailed study of these two important solar cell parts by high-resolution experimental techniques is the main goal of the first part of this thesis. The most relevant concepts concerning the features and operation principles of both the rear surface passivation layer and the rear local contacts are addressed in the following sections.

## 2.2 Surface passivation

Surface passivation is the strategy employed to reduce the recombination rate of photo-generated charge carriers (electron and holes) at the surface, and therefore, it is used to increase the conversion efficiency of solar cells [13]. Before to introduce the different technological approaches that can be used to passivate the surface of a c-Si wafer, the fundamental aspects of the different recombination mechanisms in c-Si are presented in the following sections.

### 2.2.1 Description of bulk recombination mechanisms

Under a constant light illumination and assuming steady state conditions, charge carriers in excess, electron and holes, are photo-generated in c-Si. The opposite mechanism to that photo-generation is the annihilation of electrons and holes. The rate at which such charge carriers are annihilated, i.e. the



## 2.2. Surface passivation

---

recombination rate, is defined by:

$$U = \frac{\Delta n}{\tau}, \quad (2.1)$$

where  $\tau$  is the characteristic lifetime of the photo-generated charge carriers, and  $\Delta n$  is the excess minority carrier density, which as we will see in the following lines it can be referred to both electron or hole excess carrier densities.

In c-Si, recombination between electron and holes takes place by three different fundamental mechanisms:

1. Band-to-band radiative recombination
2. Auger recombination
3. Recombination via defects (Schockley Read Hall theory)

Hence, taking into account the three different recombination mechanisms, the recombination rate at the Si bulk ( $U_{\text{bulk}}$ ) can be defined as:

$$U_{\text{bulk}} = U_{\text{rad}} + U_{\text{Aug}} + U_{\text{SRH}} = \frac{\Delta n}{\tau_{\text{rad}}} + \frac{\Delta n}{\tau_{\text{Aug}}} + \frac{\Delta n}{\tau_{\text{SRH}}}, \quad (2.2)$$

where  $U_{\text{rad}}$ ,  $U_{\text{Aug}}$  and  $U_{\text{SRH}}$  are the recombination rates assigned to the three different recombination mechanisms, and  $\tau_{\text{rad}}$ ,  $\tau_{\text{Aug}}$  and  $\tau_{\text{SRH}}$  are the corresponding lifetimes. Then, the lifetime within the c-Si bulk ( $\tau_{\text{bulk}}$ ) is defined by:

$$\frac{1}{\tau_{\text{bulk}}} = \frac{1}{\tau_{\text{rad}}} + \frac{1}{\tau_{\text{Aug}}} + \frac{1}{\tau_{\text{SRH}}}. \quad (2.3)$$

From Equations (2.2) and (2.3) we can deduce that the process with a shorter lifetime will roughly determine the recombination rate. The two first mechanisms depend exclusively on the number of electrons and holes, hence, for a given doping density and a given illumination level they are intrinsic to the material. In contrast, the later mechanism depends on the level of defects, so it can be reduced by reducing the level of defects during the manufacture process.

The free carrier concentration are given by:

$$n \equiv n_0 + \Delta n \approx N_D + \Delta n \quad \text{for n-type material}, \quad (2.4)$$

and

$$p \equiv p_0 + \Delta p \approx N_A + \Delta p \quad \text{for p-type material}, \quad (2.5)$$

where  $n_0$  ( $p_0$ ) is the electron (hole) concentration at equilibrium,  $N_D(N_A)$  is the donor (acceptor) density and  $\Delta n$  ( $\Delta p$ ) is the excess carrier density (also called injection level) for electron (holes). In the absence of trapping effects or any electric field, both excess carrier densities are equal, i.e.  $\Delta n = \Delta p$ , since generation involves the creation of electron-hole pairs.

### 2.2.1.1 Radiative recombination

Radiative recombination is the inverse process of optical generation. It occurs when an electron from the conduction band recombines with a hole in the valence band, resulting in the creation of a photon with an energy close to the band gap energy. The radiative recombination rate ( $U_{\text{rad}}$ ) depends explicitly on the availability of electrons and holes and it is given by:

$$U_{\text{rad}} = B \Delta n (\Delta n + N_A), \quad (2.6)$$

where  $B$  is the coefficient of radiative recombination and  $N_A$  is the doping density. As silicon is an indirect band-gap semiconductor, the process must be assisted by a phonon to conserve energy and momentum. Since the process involves four particles (one electron, one hole, one phonon and one photon) its probability is low.  $B$  coefficients in the range between  $1.1 \times 10^{-14}$  [14] and  $4.7 \times 10^{-15} \text{ cm}^3 \text{ s}^{-1}$  [15] have been experimentally determined. These low values of  $B$  lead to a negligible recombination rate compared to the other two recombination mechanisms that are going to be introduced below. It is worth

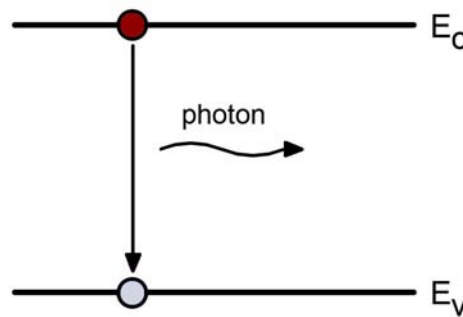


**Figure 2.5:** Scheme representing the radiative recombination between an electron and a hole.

## 2.2. Surface passivation

to mention that the photon emitted as a result of the electron-hole pair recombination can be reabsorbed before escaping from the silicon, which is called photon recycling effect.

### 2.2.1.2 Auger recombination

Auger recombination takes place when the excess energy resulting from the band-to-band recombination between an electron and a hole is transferred to a third charge carrier, being this third carrier an electron in the conduction band or a hole in the valence band [16]. Thus, we have two ways of Auger recombination depending on if the process involves two electrons or two holes, known as  $U_{eeh}$  and  $U_{ehh}$ , respectively. In its simplest analysis, the carriers are assumed to be non-interactive free carriers [17]. Hence, the recombination processes are proportional to the involved carrier densities:

$$U_{eeh} = C_n(n^2 p - n_0^2 p_0), \quad (2.7)$$

$$U_{ehh} = C_p(np^2 - n_0 p_0^2), \quad (2.8)$$

where  $C_n$  ( $C_p$ ) is the Auger coefficient for electrons (holes),  $n$  ( $p$ ) is the electron (hole) density and  $n_0$  ( $p_0$ ) is the electron (hole) density at equilibrium. The total net Auger recombination ( $U_{Aug}$ ) must be the addition of these two processes:

$$U_{Aug} = U_{eeh} + U_{ehh} = C_n(n^2 p - n_0^2 p_0) + C_p(np^2 - n_0 p_0^2). \quad (2.9)$$

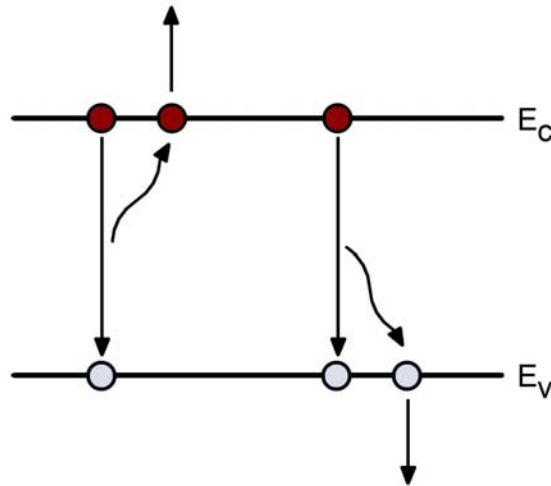


**Figure 2.6:** Scheme representing the two possible Auger recombination process between an electron and a hole.

### 2.2.1.3 Recombination via defects

Imperfections in the crystalline structure of silicon such as impurities, vacancies or dislocations, lead to a determined number of states within the band-gap that act as carrier traps for free electrons and holes. Recombination via defects is the recombination process that takes place through one of these defect states. In this case, the excess of energy is delivered by phonons. Band-to-band recombination can be considered quite improbable, since electron and holes involved in the recombination process are free, i.e. not coupled to the lattice. The probability is even lower for indirect band-gap semiconductors, because recombination must be assisted by phonons. In contrast, recombination via defects involves a defect state in the forbidden energy band-gap that is strongly coupled to the crystalline lattice. Hence, in this case, the probability of the process dramatically increases, resulting in the dominant recombination mechanism in indirect band-gap semiconductors.

Figure 2.7 depicts the four fundamental interactions between a defect centre and a charge carrier: (1) capture of an electron, (2) emission of an electron, (3) capture of a hole and (4) emission of a hole. A recombination process occurs when step (1) and (3) takes place. When a free carrier trapped in the defect releases its excess energy by a multi phonon emission process and is emitted into the same original energy band where it was captured from (steps (1) and (2), or (3) and (4)), the defect is called a trap and it does not contribute to carrier recombination.

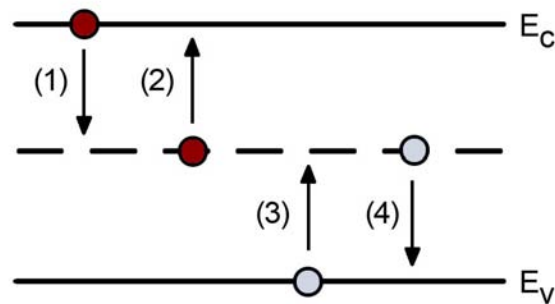


**Figure 2.7:** Fundamental possible interactions between a defect center and a charge carrier (electron or hole): (1) capture of an electron, (2) emission of an electron, (3) capture of a hole and (4) emission of a hole.

## 2.2. Surface passivation

---

The calculations of the net recombination rate was developed independently by Shockley and Read [18] and Hall [19] in the early 50's. This analysis on the probability of every possible interaction of the carrier with the defect. Considering different assumptions which were made to simplify the calculations, the net recombination rate ( $U_{SRH}$ ) for one trap located at an energy level of  $E_t$  is:

$$U_{SRH} = \frac{v_{th} N_t (np - n_i^2)}{\frac{n + n_1}{\sigma_p} + \frac{p + p_1}{\sigma_n}}, \quad (2.10)$$

being

$$n_1 = n_i e^{\frac{(E_t - E_i)}{kT}}, \quad (2.11)$$

and

$$p_1 = n_i e^{\frac{(E_i - E_t)}{kT}}, \quad (2.12)$$

where  $n_i$  is the intrinsic carrier density,  $E_i$  is the intrinsic energy level,  $\sigma_n$  ( $\sigma_p$ ) are the capture cross sections of the defect for electron (holes),  $v_{th}$  is the thermal velocity of charge carriers ( $10^7$  cm s<sup>-1</sup> in c-Si at 300 K) and  $N_t$  is the defect concentration per unit volume. Notice that under any injection level,  $U_{SRH}$  is proportional to the defect density  $N_t$ , as it was expected. In addition, the capture cross sections  $\sigma_p$  and  $\sigma_n$  represents the efficiency of the defect to capture electrons and holes. Hence, the higher the  $\sigma_p$  and  $\sigma_n$  values, the higher the net recombination rate.

### 2.2.1.4 Dependence of the excess carrier density on lifetime

As deduced from Equation, in the c-Si bulk, the recombination lifetime can be governed by different recombination mechanisms. The predominance of one or another mechanism can be determined, among others, by the level of excess carrier density. Such a dependence is shown in Figure 2.8, where the lifetime of a n-type c-Si wafer with  $B=4.7 \times 10^{-15}$  cm<sup>3</sup>s<sup>-1</sup>,  $C_p=2 \times 10^{-31}$  cm<sup>6</sup>s<sup>-1</sup> and different  $\tau_{SRH}$  is represented as a function of the excess carrier density. As it can be observed, for low carrier densities, bulk lifetime is mainly governed by recombination via defects. In contrast, for high carrier densities, bulk lifetime is mainly controlled by Auger recombination since the later is the predominant recombination process. The role of radiative recombination is significantly

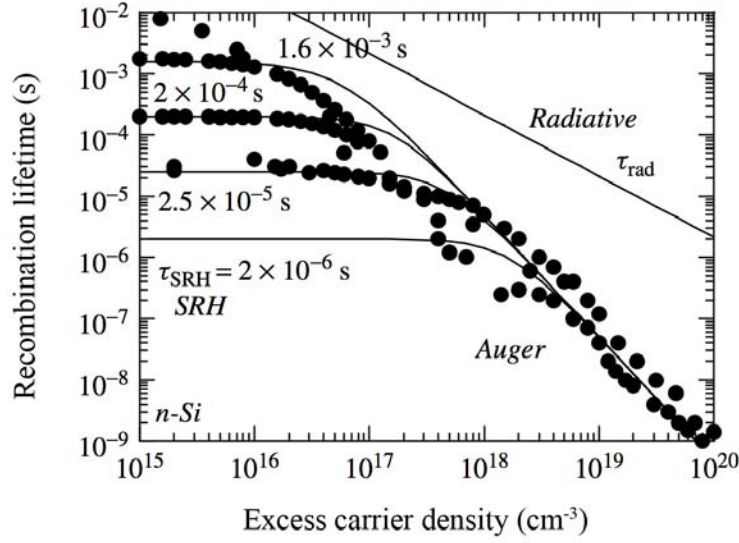


**Figure 2.8:** Recombination lifetime as a function of excess carrier density for n-type c-Si with  $B=4.7 \times 10^{-15} \text{ cm}^3 \text{s}^{-1}$  and  $C_p=2 \times 10^{-31} \text{ cm}^6 \text{s}^{-1}$ . Extracted from [20].

lower in the case of c-Si. Whereas recombination via defects is controlled by the quality of the material, Auger recombination is an intrinsic property of the semiconductor. Another important difference between low and high injection regimes is that for high excess carrier densities the high Auger recombination rate leads to a significant decrease of the recombination times. As we will see in the following chapter, most of the spectroscopic experiments shown in this thesis were carried out using a micro configuration setup, hence, were done at high injection conditions due to the strong focalization of the excitation light beam. It is important to remark that the high level of carrier densities achieved and the corresponding high level of Auger recombination rate has important implications in terms of the carrier diffusion length. It is worth to mention that despite data of Figure 2.8 was calculated for n-type c-Si, the main trends observed in the plot are also valid for p-type c-Si.

### 2.2.2 Surface recombination

At a semiconductor surface, the crystal lattice is broken. The termination of the crystalline network leads to a high density of defects within the forbidden band gap of the semiconductor, hence, a high recombination rate via defects is

## 2.2. Surface passivation

---

expected. As mentioned in section 2.2.1.3, recombination via defects is mathematically described by the Schokley-Read-Hall theory. Thus, in analogy to equation 2.10, the net recombination rate per unit area ( $U_s$ ) via a single-level surface state located at an energy  $E_t$  is given by:

$$U_s = \frac{v_{th} N_{st} (n_s p_s - n_i^2)}{\frac{n_s + n_1}{\sigma_p} + \frac{p_s + p_1}{\sigma_n}}, \quad (2.13)$$

where  $N_{st}$  is the density of effects per unit area and  $n_s$  ( $p_s$ ) is the density of electron (holes) at the surface. This equation is often presented as follows:

$$U_s = \frac{n_s p_s - n_i^2}{\frac{n_s + n_1}{S_{p0}} + \frac{p_s + p_1}{S_{n0}}}, \quad (2.14)$$

where  $S_{n0} \equiv v_{th} N_{st} \sigma_n$  and  $S_{p0} \equiv v_{th} N_{st} \sigma_p$  are the so-called fundamental recombination velocity of electron and holes, respectively.

### 2.2.2.1 Surface Recombination Velocity

In analogy to the bulk expression (see Equation (2.1)), a surface recombination velocity ( $S$ ) can be defined in the form:

$$U_s = S \Delta n_s, \quad (2.15)$$

where  $U_s$  is the surface recombination rate and  $\Delta n_s$  is the excess minority carrier density at the surface. However, in contrast to the flat band conditions at the bulk where  $\Delta n = \Delta p$ , an electric field is always present at the surface, and there is no analytical expression for the surface recombination velocity since  $\Delta n_s$  is far away from  $\Delta p_s$ . Due to the band bending conditions at the surface, it is useful to rewrite equation 2.15 by considering an effective surface recombination velocity ( $S_{eff}$ ) as follows:

$$U_s = S_{eff} \Delta n, \quad (2.16)$$

where in this case  $\Delta n = \Delta p$  corresponds to the minority carrier density at the limit of the space charge region created at the surface.

### Brief description of effective lifetime

In analogy to Equation 2.3, and taking into consideration the recombination that takes place at the surface, the effective lifetime of the minority carriers in the Si wafer ( $\tau_{\text{eff}}$ ) can be expressed as:

$$\frac{1}{\tau_{\text{eff}}} = \left( \frac{1}{\tau_{\text{rad}}} + \frac{1}{\tau_{\text{Aug}}} + \frac{1}{\tau_{\text{SRH}}} \right)_{\text{bulk}} + \frac{1}{\tau_s}, \quad (2.17)$$

where  $\tau_s$  is the lifetime at the surface. For a wafer symmetrically passivated showing low values of  $S_{\text{eff}}$ , i.e. below around  $250 \text{ cm s}^{-1}$ , Equation (2.17) can be read as:

$$\frac{1}{\tau_{\text{eff}}} = \frac{1}{\tau_{\text{bulk}}} + \frac{2S_{\text{eff}}}{W}, \quad (2.18)$$

where  $W$  is the wafer thickness.

#### 2.2.2.2 Reduction of surface recombination

From Equation (2.14) that gives the dependence between the surface recombination rate and the physical parameters of the surface, the two different technological strategies to reduce surface recombination can be deduced. These are: (1) the reduction of recombination velocities of electron and holes, and (2) the reduction of the concentration of one type of carriers:

1. **Reduction of  $S_{n0}$  and  $S_{p0}$ :** This strategy is based on decreasing directly the fundamental recombination velocities of electron and holes. Since  $v_{\text{th}}$  in Equation 2.13 is a constant of the semiconductor material and  $\sigma_n$  ( $\sigma_p$ ) are parameters intrinsically related to the type of defect, the reduction of  $S_{n0}$  and  $S_{p0}$  is mainly based on decreasing the density of surface states ( $N_{\text{st}}$ ). As schematically represented in Figure 2.9, a reduction of  $N_{\text{st}}$  would reduce the number of recombination processes marked by A arrows. From a technological point of view, this is achieved by the deposition or grown of a passivating layer over the c-Si surface.
2. **Reduction of electron or hole concentration:** As recombination via defects involves one electron and one hole, the higher recombination rate will be achieved in case of equal electron and hole densities at the surface. In contrast, if density of one type of carriers is drastically reduced at the surface, then surface recombination will be strongly reduced. As electrons as well as holes carry electrical charge, such a reduction of one



## 2.2. Surface passivation

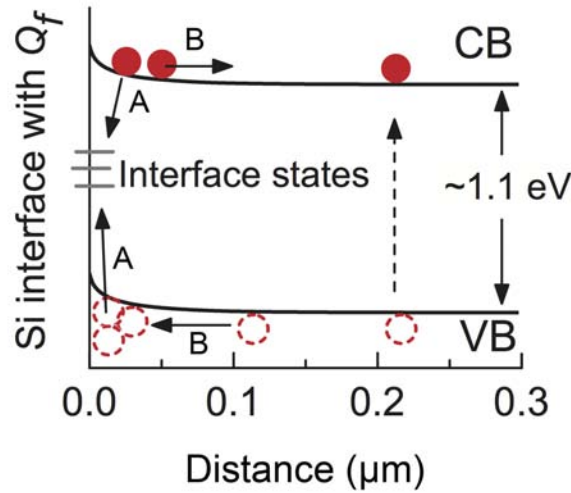


**Figure 2.9:** Band diagram within 300 nm below a p-type c-Si surface under the influence of a negative surface fixed charge of  $Q_f = 2 \times 10^{12} \text{ cm}^{-2}$ . Extracted from [21].

charge carriers can be achieved by the presence of an internal electric field below the semiconductor surface. This method is known as *field-effect passivation* and its effects are qualitatively described in Figure 2.9 by B arrows. Obviously, since the concentration of minority carriers is proportionally lower, the field-effect passivation will be more efficient if the built-in electric pushes away the latter charge carriers from the surface. Technologically there are two different methods to create an electric field at the sub-surface region:

◇ **Implementation of a doping profile below the silicon surface:** In this case, the built-in electric field is achieved by the non-uniform concentration of dopant atoms in a crystal lattice. The standard method to create such a doping profile is based on a diffusion process at high temperature ( $\sim 900^\circ \text{C}$ ). In case of doping impurities with the same polarity than c-Si wafer, a high-low junction ( $p^+p$  or  $n^+n$ ) is created. The most common application of a  $p^+p$  high-low junction can be found in the back contact of a solar cell for reducing the rear surface recombination. This specific structure is also known as Back Surface Field (BSF). Equivalently, if the high-low junction is located at the front surface of the solar cell, it is referred as Front Surface Field (FSF). In contrast, if the profile doping

impurities have a different polarity respect the dopant atoms of the c-Si wafer, then a p-n junction is implemented. In most cases, these junctions are contacted, so a part of passivating the semiconductor surface, they also separate the photo-generated charge carriers and work as injection junctions. In these cases, they are called emitters. In contrast, if the p-n junctions are not contacted, the resulting surface passivation scheme is known as floating-junction passivation.

◇ *Presence of electrostatic charges on an overlying insulator:* In practice, most insulator systems used for c-Si surface passivation such as silicon dioxide ( $\text{SiO}_2$ ) or silicon nitride ( $\text{SiN}_x$ ) lead to the formation of electrostatic charges within the insulator. These are generated by dangling bonds of Si atoms at/near the silicon-insulator interface. Apart from these materials, an extra fixed charge density can be introduced within any dielectric material deposited onto c-Si surface by using the corona charge technique consisting in an implantation of external ions on the insulator surface.

### 2.2.2.3 Surface passivating materials

The two fundamental passivation approaches mentioned above are often combined in order to achieve minimum surface recombination rates. For instance, the use of thermally grown  $\text{SiO}_2$  layers strongly reduces the number of surface states ( $N_{\text{st}}$ ) specially after their annealing in forming gas ( $\text{H}_2/\text{N}_2$ ), in which the introduced hydrogen passivates the electronically active defects [22]. In addition, due to fixed positive fixed charges,  $\text{SiO}_2$  also leads to a field-effect passivation mechanism which further reduce the recombination velocity at the surface. The combination of both passivation strategies in  $\text{SiO}_2$  layers provides excellent surface passivation, as demonstrated by very low  $S_{\text{eff}}$  values below  $10 \text{ cm s}^{-1}$  in n- and p-type c-Si wafers with resistivities in the range between 1-100  $\Omega \text{ cm}$  [23]. Despite the excellent c-Si surface passivation provided by thermally grown  $\text{SiO}_2$ , there are two important drawbacks associated to the required elevated processing temperatures that difficult the industrial implementation of thermally grown  $\text{SiO}_2$ . One is the high production costs associated to such as elaborate processing, and two is the possible bulk lifetime degradation induced by the use of high-temperature steps.

Another widely employed passivating dielectric material is hydrogenated amorphous silicon nitride ( $\text{a-SiN}_x\text{:H}$ ), for brevity,  $\text{SiN}_x$ , synthesized by Plasma

## 2.2. Surface passivation

---

Enhanced Chemical Vapor Deposition (PECVD) [24]. Due to the fact that a wide range of the material optical properties can be varied,  $\text{SiN}_x$  is the standard antireflection coatings in solar cells [25]. Films with higher nitrogen content exhibits refractive indices around 2, which results in optimal antireflection properties when applied on the front side of a solar cell. In addition, the nitrogen content is also determinant for the passivation mechanisms exhibited by  $\text{SiN}_x$  films. While for lower contents of nitrogen, the high levels of passivation are governed by chemical passivations, films that exhibit higher contents of nitrogen induce a significant amount of field-effect passivation with positive fixed charge densities in the order of  $10^{12} \text{ cm}^{-2}$ . This high positive fixed charge provides good field-effect passivation for lowly doped and highly doped n-type silicon [24]. However, passivation performance of  $\text{SiN}_x$  decreases for p-type silicon, specially for highly doped substrates.

During the last years,  $\text{Al}_2\text{O}_3$  is becoming one of the most studied materials for the rear surface passivation of p-type crystalline silicon (c-Si) wafers [21, 26].  $\text{Al}_2\text{O}_3$  offers a high negative fixed charge which induces a high field-effect surface passivation [27]. Furthermore, its field-effect passivation mechanism is combined with a relatively high level of chemical passivation (low level of surface defect density) [28, 29]. The good combination of both passivation processes leads to very low surface recombination velocities below  $10 \text{ cm s}^{-1}$  [30]. Since most of the experiments carried out in this thesis are focused on the study of p-type c-Si wafers passivated by a thin film of  $\text{Al}_2\text{O}_3$ , a detailed description of the features of this passivating insulator material is presented in the following section.

### 2.2.3 Surface passivation by $\text{Al}_2\text{O}_3$

The passivation properties of  $\text{Al}_2\text{O}_3$  were reported for the first time in 1989 by Hezel and Jaeger [31]. However, it was not until almost two decades after when  $\text{Al}_2\text{O}_3$  was demonstrated to be an excellent passivation material. In particular, it was in 2006 when Hoex et al. [32] and Agostinelli et al. [33] reported that  $\text{Al}_2\text{O}_3$  layers synthesized by Atomic Layer Deposition (ALD) could equalize the passivation performance of thermally grown  $\text{SiO}_2$ , which had been considered for a long time the workhorse material for surface passivation.  $\text{Al}_2\text{O}_3$  can be considered an exceptional passivating material as it uniquely features a combination of:

- field effect passivation by negative fixed charge

- low interface defect density
- good stability during processing,

being the former the key condition that has boost to  $\text{Al}_2\text{O}_3$  as the most promising and studied passivating material during the last decade. This fact can be explained by two trends. The first one is that due to cost-drive reduction of the solar cell thickness, the well-established rear passivation scheme by Al-based BSF was required to be replaced by novel and more efficient passivation strategies such as dielectric passivating layers. Due to inversion layer shunting, a-SiN<sub>x</sub>:H was not a suitable candidate for the rear side of p-type wafers. On the other hand, thermally grown  $\text{SiO}_2$  was also not a suitable choice due to elevated fabrication costs, and possible adverse impacts associated to the use of high processing temperatures ( $\sim 950\text{--}1100^\circ\text{C}$ ). Thus, attention of PV manufacturers rapidly shifted to  $\text{Al}_2\text{O}_3$  as an ideal candidate for passivating the p-type Si rear surface. The second trend, which has a direct implication from the first, is that the negative fixed charge offered by  $\text{Al}_2\text{O}_3$  represented also a suitable solution to passivate p+ emitters in n-type Si solar cells. Figure 2.10 represents the influence of a negative fixed surface charge on the electron and hole density distribution within 300 nm below the surface. The corresponding band bending is also shown. As it can be seen, in case of p-type c-Si, the increase of holes near the surface leads to accumulation conditions. As minority carrier density

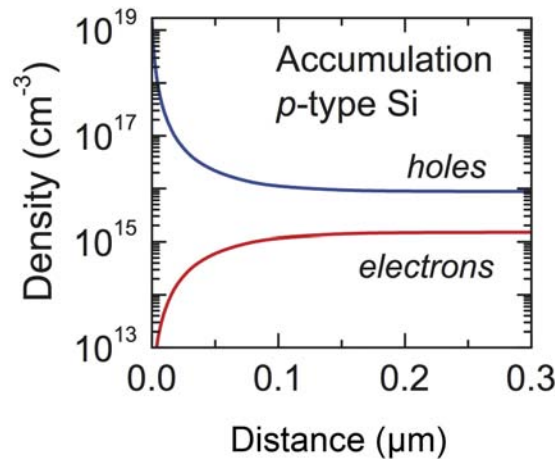


**Figure 2.10:** Electron and hole carrier densities within 300 nm below a p-type c-Si surface under the influence of a negative surface fixed charge of  $Q_f=2\times 10^{12}\text{ cm}^{-2}$ . Extracted from [21].

## 2.2. Surface passivation

---

$n_s$  decreases strongly close to the surface, surface recombination is drastically reduced. In addition, the good chemical passivation offered by  $\text{Al}_2\text{O}_3$  further reduces recombination by decreasing recombination via interface states.

### 2.2.3.1 Origin of intrinsic negative charge

Despite the origin of the negative fixed charge ( $Q_f$ ) formation in  $\text{Al}_2\text{O}_3$  has not been clearly established yet, the presence of point defects as vacancies and interstitials is believed to be the most probable origin of charge traps [34]. Experimentally, it is difficult to determine the presence and type of point defects in ultra thin films. Nevertheless, various simulation studies have given an insight about the possible formation of such a charge traps. In particular, some reported calculations have proven that Al vacancies and O interstitials produce levels in the  $\text{Al}_2\text{O}_3$  bandgap below the midgap, and therefore, are likely candidates to trap negative charges [35, 36].

### 2.2.3.2 Increase of passivation performance by annealing

As-deposited  $\text{Al}_2\text{O}_3$  layers synthesized by thermal-ALD show reasonable good level of surface passivation, as demonstrated by values of surface recombination velocities ( $S$ ) down to  $30 \text{ cm s}^{-1}$ . However, after annealing at temperatures around  $400^\circ\text{C}$ , low  $S$  values down to  $5 \text{ cm s}^{-1}$  and  $2 \text{ cm s}^{-1}$  were obtained for p-type and n-type c-Si, respectively [37]. Thus, it is clear that annealing treatments are required to activate passivation of  $\text{Al}_2\text{O}_3$  layers.

A standard annealing treatment consists on anneal the  $\text{Al}_2\text{O}_3$  layer in forming gas (a gas mixture of  $\text{N}_2$  and  $\text{H}_2$ ) at a temperature range between  $350$  and  $450^\circ\text{C}$  for 10-30 min. Shorter annealing times of 2-5 min have demonstrate to be sufficient to fully activate the passivation capabilities [21]. In its as-deposited state,  $\text{Al}_2\text{O}_3$  layers evidence relatively low interface trap density ( $D_{it}$ ) values in the order of  $3 \times 10^{11} \text{ eV}^{-1} \text{ cm}^{-2}$ , which explains the moderate level of surface passivation prior to annealing [38]. Thus, the key effect induced by annealing is the increase of negative fixed charge ( $Q_f$ ). Before annealing treatment,  $\text{Al}_2\text{O}_3$  layer exhibits  $Q_f$  values in the order of  $-1 \times 10^{11} \text{ cm}^{-2}$ , which increases up to values around  $-5 \times 10^{12} \text{ cm}^{-2}$  after annealing [39, 40]. The increase in  $Q_f$  is observed to happen during the initial annealing step between  $300$  and  $400^\circ\text{C}$ , and after that appeared to be relatively independent for annealing temperatures above  $400^\circ\text{C}$  [41].

Despite of less importance than that observed for field-effect passivation,

annealing treatments also induce improvements in the chemical passivation of  $\text{Al}_2\text{O}_3$  layers. It is well known that Si/ $\text{Al}_2\text{O}_3$  interface exhibits defect states correlated to trivalent bonds in Si atoms [42]. Such trivalent Si interface traps are chemically active, but they can be passivated by hydrogen. In fact, it has been shown that hydrogenation of the interface play an important role in the chemical passivation of the  $\text{Al}_2\text{O}_3$ /c-Si interface [43]. In contrast to field-effect passivation which is expected to be relatively stable at temperatures above 400 °C, chemical passivation has been shown to be sensitive to the annealing temperature [44]. For annealing temperatures below a critical value, diffusion of hydrogen atoms to the  $\text{Al}_2\text{O}_3$ /c-Si interface is expected to take place, inducing a reduction of the interface states. However, the use of higher temperatures that optimum, could eliminate those passivating hydrogen atoms form the interface, inducing a drastic increase of the surface recombination velocities.

## 2.3 Laser-Fired Contact (LFC) approach

Since novel high-efficiency c-Si solar cell technologies feature rear surface passivation, local point contacts are required to extract the photo-generated charge carriers through the rear dielectric film. In this sense, the so-called Laser-Fired Contact (LFC) approach [45, 46] has emerged as a very promising alternative for the creation of back contacts in PERC solar cells. LFC process is based on firing the predeposited rear Al metallization layer using a laser beam with the finality to create a local point contact through the passivation layer and contact electrically the rear Al layer with the silicon substrate. As depicted in Figure 2.11, this method is intended to be used to create a rear point contact pattern without the necessity of using photolithography which is a cost- and material-intensive process that involves several handling steps. Hence, LFC approach represents an easy, rapid and cost-effective method that significantly eases the implementation of both laboratory and industrial scale PERC solar cells. In addition, as LFC technology is a room temperature process, it avoids the possibility of wafer warping that has becoming a major drawback when combining thin wafers and high-temperature firing steps associated to screen-printed solutions [47].

## 2.3. Laser-Fired Contact (LFC) approach

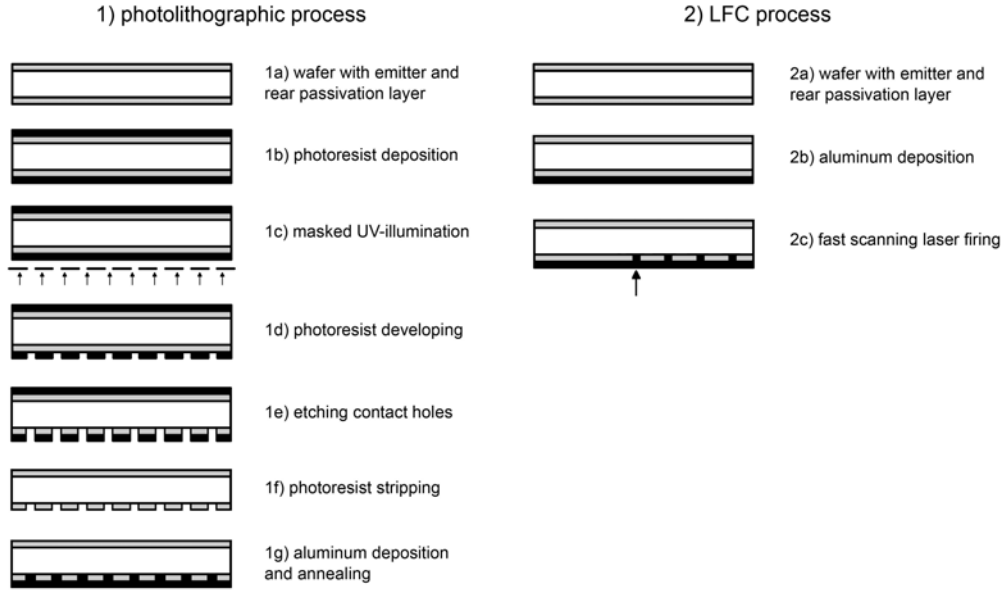


**Figure 2.11:** Comparison between a conventional photolithographic process and the LFC technology for creating the rear point contacts in PERC solar cells [45].

### 2.3.1 Key features of Laser-Fired Contacts (LFCs)

From an electric point of view, an interesting feature of LFC process is the formation of an Al-doped p<sup>+</sup> region under the contacted surface region if proper laser conditions are used. This is achieved by the thermally-assisted diffusion of Al atoms from the top Al layer into the melted Si. This p<sup>+</sup> region not only creates a local BSF that induces a relatively low recombination velocity below the contacts, but also ensures a low-contact resistance independently of the substrate resistivity. These two features are supposed to strongly influence the final solar cell performance. Hence, the p<sup>+</sup> region formed under the Laser-Fired Contacts (LFCs) is considered a key feature for the good operation of the LFC approach.

LFC approach can be applied by using any of the dielectric layers that have demonstrated excellent c-Si passivating properties such as SiO<sub>2</sub> [48], silicon nitride (SiN<sub>x</sub>) [49], amorphous-silicon carbide (a-SiC<sub>x</sub>) [50], and most recently, aluminum oxide (Al<sub>2</sub>O<sub>3</sub>) [51]. In the case of using the later dielectric material as rear passivation layer, an interesting alternative to the conventional LFC process can be applied [48]. In this case, the Al<sub>2</sub>O<sub>3</sub> layer itself acts as Al-dopant source for the p<sup>+</sup> region formation, and therefore, the contact can be done

directly onto the  $\text{Al}_2\text{O}_3/\text{c-Si}$ , instead of being done onto the Al/dielectric/c-Si stack. This approach enables the use of lower laser powers in comparison to the conventional LFC process where high laser powers are needed to fire the aluminum through the dielectric layer. Thus, this process involves a softer laser treatment which can be important for reducing the possibility to undergo structural defects, such as cracks, in the Si structure.

Laser firing concept has been also extended to develop local emitter on the front side of c-Si solar cells [52]. Despite this is a very promising technology for developing novel high-efficiency c-Si solar cell concepts, this approach is out of the scope of this thesis and it is not going to be addressed in the present document.

We would like to underline that all LFCs studied in this work have been processed in  $\text{Al}_2\text{O}_3/\text{c-Si}$  samples (without Al layer on top), hence by using the low-laser power process mentioned above. From now on, all introduced concepts concerning the LFC approach will be related to this variation of the process.

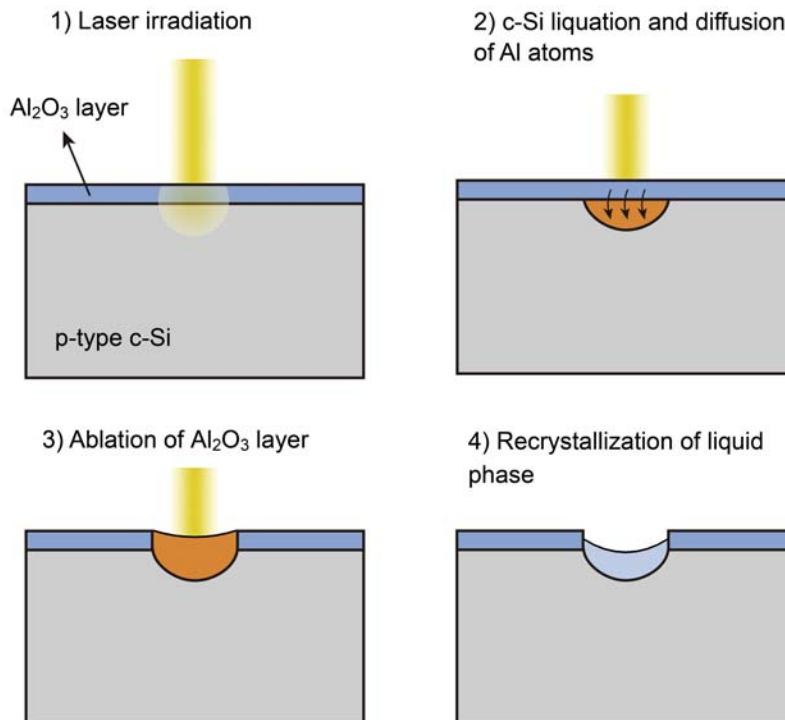


**Figure 2.12:** Schematic representation of the LFCs formation steps.



### 2.3.2 Considerations of LFCs formation

A single LFC process can be roughly described as a rapid melting and recrystallization cycle that usually takes place in less than one microsecond. The detailed steps that occur during this rapid process are the following (see Figure 2.12):

1. **Laser irradiation and thermal energy absorption:** the laser beam hits the  $\text{Al}_2\text{O}_3$ -passivated c-Si laser and laser thermal energy is absorbed by the illuminated material region.
2. **c-Si melting and Al atoms diffusion:** As a consequence of the thermal energy absorption, the material temperature rises and when it overcomes the material melting temperature, the material starts to melt. Since the melting point of Si (1414 °C) is lower than that of the  $\text{Al}_2\text{O}_3$  (2071 °C), and moreover the  $\text{Al}_2\text{O}_3$  is transparent at the used laser wavelength (in our case 1064 nm), Si material fraction is expected to melt firstly. In contrast,  $\text{Al}_2\text{O}_3$  layer is not expected to melt during the first part of the process. However, the progressively increase of temperature is believed to induce a thermally-assisted dopant atoms diffusion from the  $\text{Al}_2\text{O}_3$  layer to the melted Si fraction.
3.  **$\text{Al}_2\text{O}_3$  melting:** If the temperature of the liquid phase fraction continues to rise, it can overcome the  $\text{Al}_2\text{O}_3$  melting point. Once this happens, the  $\text{Al}_2\text{O}_3$  layer will also start to melt.
4. **Liquid phase solidification:** When the laser pulse stops, thermal energy is progressively dissipated and liquid phase starts to solidify. Solidification is expected to take place from the bottom of the liquid fraction towards the silicon surface via epitaxial growth. If laser processing is carried out in air, the upper most surface of the molten silicon is believed to react with ambient oxygen and subliming to the air. Hence, a small fraction of silicon is lost during the process.

### 2.3.3 Optimization of LFC

LFCs are usually processed on a sample surface drawing a squared matrix array distribution. As represented in Figure 2.13, such an array of LFCs is geometrically determined by both the radius of the contacts ( $r$ ) and the distance between them, the so-called pitch ( $p$ ). From these two parameters, the

contacted area fraction ( $f_c$ ) defined as the percentage of the laser-processed sample surface is obtained by:

$$f_c = \frac{\pi r^2}{p^2} . \quad (2.19)$$

Because the radius of LFCs usually shows very small variations (characteristic radius values range between 20 and 40  $\mu\text{m}$ ),  $p$  is the key parameter to achieve a proper optimization of the LFC approach. Short  $p$  values (high  $f_c$ ) induce a lower specific base series resistance, i.e. higher fill factors. Conversely, long  $p$  values (low  $f_c$ ) results in lower surface recombination velocities, i.e. high open circuit voltages. Hence, there is a trade-off for this parameter that results in an optimum performance of the LFC approach.

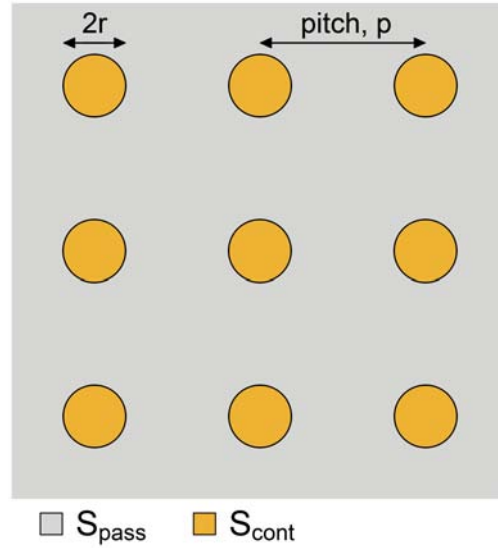


**Figure 2.13:** Scheme of an array of LFCs. Geometrically, it is defined by the radius of contacts ( $r$ ) and by the distance between them, the so-called pitch ( $p$ ).  $S_{\text{pass}}$  defines the surface recombination velocity at the non-processed region, whereas  $S_{\text{cont}}$  corresponds to the surface recombination velocity at the contacts.

### 2.3.3.1 Recombination at the laser-processed surface

As it has been shown, LFC approach is used to open local apertures through the passivation layer. Hence, the surface recombination velocity at the laser-processed region is expected to increase considerably respect the recombination velocity before the laser processing. However, the formation of a  $p^+$  region

### 2.3. Laser-Fired Contact (LFC) approach

---

below the laser-processed surface region increases locally the surface passivation by BSF and helps to achieve moderate levels of surface passivation at the contacts. According to the analytical model described by Fischer in 2003 [53], the impact of laser processing on surface passivation can be determined assuming that non-processed surface keeps its initial good passivation, and therefore, the increase in surface recombination velocity is only attributed to the contacts. Thus, as we can qualitatively observe in Figure 2.13, an effective surface recombination velocity ( $S_{\text{eff}}$ ) at the laser-processed surface can be determined by both the surface recombination velocity at the non-processed area fraction ( $S_{\text{pass}}$ ) and the surface recombination velocity at the processed contacts ( $S_{\text{cont}}$ ). According to Fischer, an  $S_{\text{eff}}$  in the surface processed by laser is defined by the following analytical expression:

$$S_{\text{eff}} = \left( \frac{R_s - \rho W}{\rho D_e} + \frac{1}{f_c S_{\text{cont}}} \right)^{-1} + \frac{S_{\text{pass}}}{1 - f_c}, \quad (2.20)$$

where  $\rho$  is the resistivity of the wafer,  $W$  is the wafer thickness,  $D_e$  is the electron diffusion coefficient and  $R_s$  is the base series resistance. The latter can be obtained from the following expression:

$$R_s = \frac{p^2 \rho}{2 \pi r} \tan^{-1} \left( \frac{2W}{r} \right) + \rho W \left[ 1 - \exp \left( -\frac{W}{p} \right) \right], \quad (2.21)$$

where  $r$  is the radius of the spots.

However, as described above, the LFC formation is characterized by a local melting and solidification step of the bulk c-Si. In such a rapid high-temperature cycle, the surface around the LFC is believed to suffer high thermal gradients during the contact formation. This could induce important damage on the passivation capabilities around the contacts, since as mentioned in Section 2.2.3, high temperatures can reduce the chemical passivation mechanism of  $\text{Al}_2\text{O}_3$  films. A comprehensive analysis about the effect of the laser processing at the LFCs vicinity is presented in Chapter 6.



# 3

## Characterization techniques

*In the present chapter, the different characterization techniques used in this thesis are presented. Special importance has been given to those features and peculiarities which make these techniques suitable tools to obtain unique and valuable information about PV devices and materials. A common denominator in all these techniques is the elevated spatial resolution achieved. In the first section, Photoluminescence (PL) spectroscopy is briefly introduced. From this basic introduction, the most important aspects of micro-PL measurements and cryogenic micro-PL measurements have been subsequently described. In the second section, important aspects of micro-Raman spectroscopy measurements for silicon-based systems analysis are explained. In the third section, different variations of Scanning Probe Microscopies (SPM) such as conductive-Atomic Force Microscopy (c-AFM) and Kelvin Probe Force Microscopy (KPFM) are addressed. Finally, in the last section, we give a brief summary about other macroscopic techniques that have been applied in order to obtain specific material or device parameters, such as effective lifetime or dielectric fixed charge.*

### 3.1 Photoluminescence (PL) spectroscopy

Photoluminescence (PL) is the spontaneous emission of light from a material under illumination. The emitted light is the result of the radiative recombination between photo-excited electrons in the Conduction Band (CB) and the corresponding holes in the Valence Band (VB) (see Section 2.2.1.1). Hence, PL is a selective and extremely sensitive probe of discrete electronic states. The features of the emission spectrum can be used to identify surface, interface and impurity levels. Moreover, the intensity of the PL signal provides information of the quality of surfaces and interfaces. PL analysis is nondestructive, so the technique requires very little sample manipulation.

In the present thesis, PL spectroscopy has been used to carry out two specific studies in PV materials. On the one hand, micro-PL spectroscopy measurements have been applied to characterize the local impact of the laser pulse in LFC processes. On the other hand, low-temperature micro-PL experiments applied to the study of  $\text{Al}_2\text{O}_3$ -passivated c-Si wafers have been used to obtain important information about the  $\text{Al}_2\text{O}_3$ -Si interface. Prior to introduce in more detail the basis of these techniques, a brief state of the art about PL experiments for characterizing PV materials and devices is addressed.

#### 3.1.1 PL for the study of passivated c-Si

PL spectroscopy has been extensively used for the rapid and non-invasive characterization of the performance of passivation materials at a qualitative level [54]. Moreover, by further combining PL spectroscopy and photo-current measurements, it is possible to obtain reliable quantitative results regarding the lifetime of the photogenerated carriers [55, 56], namely the efficiency of the passivation system under study.

##### 3.1.1.1 Brief description about steady-state conditions

With a time dependent photo-generation rate of electron-hole pairs ( $G(t)$ ), the excess carrier density ( $\Delta n(t)$ ) obeys the continuity equation as:

$$\frac{d\Delta n(t)}{dt} = G(t) - U_{\text{eff}} , \quad (3.1)$$

being

$$U_{\text{eff}} = \frac{\Delta n(t)}{\tau_{\text{eff}}(\Delta n(t))} . \quad (3.2)$$

### 3.1. Photoluminescence (PL) spectroscopy

---

where  $U_{\text{eff}}$  corresponds to the effective recombination rate and  $\tau_{\text{eff}}(\Delta n(t))$  corresponds to the injection level dependent effective lifetime.

However, assuming steady state conditions where:

$$\frac{d\Delta n(t)}{dt} = 0, \quad (3.3)$$

the generation rate ( $G$ ) and the recombination rate ( $U_{\text{eff}}$ ) in Equation (3.1) are balanced and the expression can be rewritten thereby:

$$G = U_{\text{eff}} = \frac{\Delta n}{\tau_{\text{eff}}} \Rightarrow \tau_{\text{eff}} = \frac{\Delta n}{G}. \quad (3.4)$$

#### 3.1.1.2 Qualitative determination of passivation efficiency

As mentioned in Section 2.2, recombination of photo-generated carriers in a semiconductor material such as c-Si takes place via radiative, Auger or recombination via defects mechanisms. These three recombination mechanisms can be divided at the same time in two types: radiative and non-radiative processes. Thus, the total recombination rate,  $U_{\text{total}}$ , defined in Equation (2.2), can be expressed as the sum of both radiative and non-radiative recombination mechanisms:

$$U_{\text{total}} = U_{\text{rad}} + U_{\text{nonrad}}. \quad (3.5)$$

Resolving for the lifetime ( $\tau_{\text{total}}$ ), Equation (3.5) can be also expressed by:

$$\frac{1}{\tau_{\text{total}}} = \frac{1}{\tau_{\text{rad}}} + \frac{1}{\tau_{\text{nonrad}}}. \quad (3.6)$$

From the ratio of measured lifetime to radiative lifetime, the PL efficiency of a material can be expressed as:

$$\eta_{\text{PL}} = \frac{\tau_{\text{total}}}{\tau_{\text{rad}}}. \quad (3.7)$$

In general, indirect band gap semiconductors as c-Si show low PL response. This is due to the fact that non-radiative recombination is the dominant recombination mechanism, and therefore, has associated a much lower lifetime. However, since both radiative and non-radiative processes are mutually excluding mechanisms, the PL signal can be used to infer the level of non-radiative recombination. Thus, for samples with the same doping level and assuming steady-state conditions under identical excitation conditions, the detected PL intensity can be employed to assess, at a qualitative level, the passivation performance of different materials.

### 3.1.1.3 Quantitative determination of lifetime

The photoluminescence intensity is proportional to the radiative recombination rate ( $U_{\text{rad}}$ ) defined in Equation (2.6), and repeated thereby:

$$I_{\text{PL}} \propto U_{\text{rad}} = B_{\text{rad}} \Delta n (\Delta n + N_A), \quad (3.8)$$

where  $B_{\text{rad}}$  is the coefficient of radiative recombination and  $N_A$  is the doping density. Due to screening effects,  $B_{\text{rad}}$  is reduced for higher charge carrier densities. However, for  $\Delta n < 10^{15} \text{ cm}^{-3}$  and doping concentrations of  $N_A > 10^{15} \text{ cm}^{-3}$ ,  $B_{\text{rad}}$  is a constant, and Equation (3.8) can be rewritten thereby:

$$I_{\text{PL}}(\Delta n) = C N_A \Delta n + C \Delta n^2, \quad (3.9)$$

where  $C$  is a calibration constant that depends on the experimental setup (power, optical filters, detector) and sample properties (thickness, surface morphology). In principle, one single measurement of the PL intensity ( $I_{\text{PL}}$ ) and the excess carrier density ( $\Delta n$ ) under identical excitation conditions and using the same experimental setup is enough to obtain the calibration constant  $C$ . This, for instance, can be done by the simultaneous application of PL and photo-conductance (PC) measurements. Once calibration constant  $C$  is known, we can convert the detected  $I_{\text{PL}}$  into absolute values of  $\Delta n$  of the silicon sample under study by means of Equation (3.9).

Finally, if measurements are carried out under steady-state condition, the obtained absolute values of  $\Delta n$  can be converted into effective lifetime values by Equation (3.4). For that, we need to know generation  $G$  that can be obtained by:

$$G = \Phi (1 - R_f) \frac{1}{W}, \quad (3.10)$$

where  $W$  is the wafer thickness,  $R_f$  is the reflectivity of the sample at the illumination wavelength and  $\Phi$  is the photon flux that is usually measured in the experiment by a calibrated solar cell.

## 3.1.2 Micro-PL spectroscopy

As already mentioned, the objective of the present thesis is focused on the study of PV materials and devices at the sub micron level. In order to achieve such a high spatial resolutions, PL measurements have to be performed using a micro-setup configuration [57]. As observed in Figure 3.1, micro-PL measurements are carried out by focusing the excitation light beam onto the sample



### 3.1. Photoluminescence (PL) spectroscopy

---

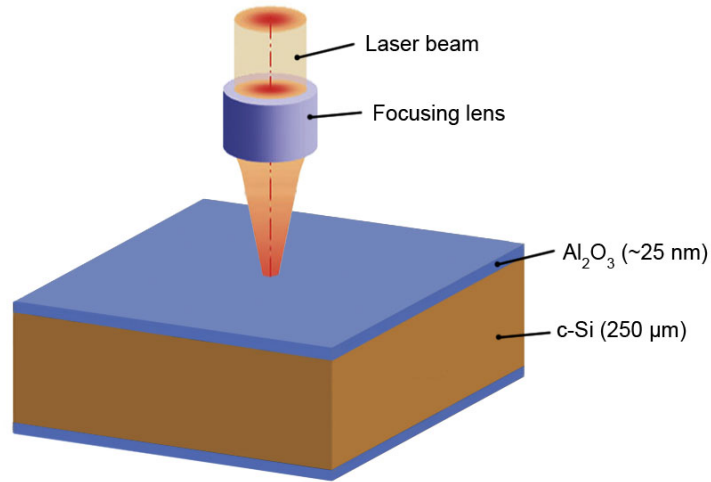


**Figure 3.1:** Experimental setup for a micro-PL spectroscopy experiment. The excitation light beam is typically focused onto the sample surface by microscopic objectives. The light emitted from the material is also collected by the same microscopic objectives, and after its collection is sent to the detector.

surface by focalization lenses, i.e. conventional microscopic objectives, leading a light spot diameter of few microns. The final dimensions of the light spot onto the sample surface depends on the experimental setup. Basically, it depends on the laser beam diameter before being focalized, and the magnification of the focalization lens used.

An important difference between macro- and micro-PL spectroscopy experiments relies on the injection level at which these measurements are performed. In macro-PL measurements where illumination level is assumed to be in the order of 1 sun, the injection level takes values around  $10^{15} \text{ cm}^{-3}$ . In contrast, in the case of micro-PL measurements, the focalization of the light beam in a very small spot leads to high values of injection level. For instance, levels in the order of  $10^{18}$ - $10^{19} \text{ cm}^{-3}$  can be easily reached.

The difference on the injection levels between the two measurement configurations has important implications in terms of the experimental parameters and physical conditions at which the measurements are developed. According to Figure 2.8 (Section 2.2.1.4), for excess carrier densities around  $10^{15} \text{ cm}^{-3}$ , bulk recombination is mainly determined by recombination via defects, resulting in values of recombination lifetime in the order of 1000  $\mu\text{s}$ . In contrast, for excess carrier densities above  $10^{18} \text{ cm}^{-3}$ , bulk recombination is controlled

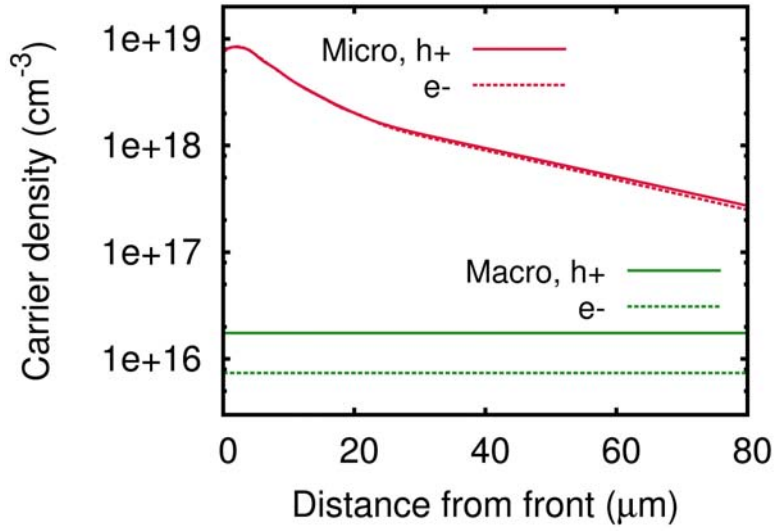


**Figure 3.2:** Simulated electron and hole carrier profiles below the illuminated material surface for representative macro- and micro-PL spectroscopy measurements.

by Auger recombination and lifetime decreases dramatically down to values below 1  $\mu\text{s}$ . Since the diffusion length ( $L_{\text{length}}$ ) depends quadratically on the lifetime ( $\tau$ ) as:

$$L_{\text{length}} = (D\tau)^{1/2}, \quad (3.11)$$

where  $D$  is the diffusivity, the low recombination lifetime associated to micro-PL experiments leads to a small diffusion length. Hence, the large light beam focalization associated to micro-PL experiments has implicitly correlated a very high spatial resolution. An example of this phenomenon is illustrated in Figure 3.2, where simulations by PC1D have been used to obtain representative electron and hole carrier density profiles below the illuminated surface for typical macro- and micro-PL experiments. Calculations were done assuming a monochromatic 633 nm illumination. For macro-PL measurements, a light irradiation of  $0.1 \text{ W cm}^{-2}$ , a bulk recombination lifetime of  $1000 \mu\text{s}$ , and a surface recombination velocity of  $30 \text{ cm s}^{-1}$  were used. In the case of micro-PL measurements, the light irradiation, the bulk lifetime and the surface recombination were assumed to be  $3 \times 10^5 \text{ W cm}^{-2}$ ,  $0.5 \mu\text{s}$ , and  $1 \times 10^5 \text{ cm s}^{-1}$ , respectively. Such high surface recombination and low bulk lifetime are typically achieved under high injection conditions, i.e.  $\sim 1 \times 10^{18} \text{ cm}^{-3}$  [58]. As it can be seen, macro-PL measurements show a moderate carrier density of around  $1 \times 10^{16}$

### 3.1. Photoluminescence (PL) spectroscopy

---

that is constant along the material thickness. The obtained profile is correlated to a large diffusion length,  $L$ , of about 1000  $\mu\text{m}$ . In contrast, due to the large focalization of the light beam, carrier profiles linked to micro-PL measurements give a significantly higher carrier concentration below the surface, which decreases rapidly as a consequence of the lower carrier diffusion length. A remarkable observation in the micro-PL profiles is the local decay of the curve at the points very close to the surface. This feature is correlated to the high recombination velocity at the surface under strong injection levels, and it is going to be a common peculiarity in all the simulated carrier concentration profiles presented in the next section.

It is worth to mention that the characterization by micro-PL spectroscopy does not allow the conversion of relative PL signal to absolute  $\Delta n$  values through PC measurements calibration (see Section 3.1.1.3). At the high carrier densities achieved by micro-PL measurements,  $B_{\text{rad}}$  is not constant due to screening effects and the quantitative determination of lifetime is not possible. Nevertheless, despite only qualitative results concerning the quality of passivation systems can be obtained by micro-PL measurements, its associated high lateral resolution allows to obtain unique and exclusive information about particular features of the material systems and devices under study.

#### 3.1.2.1 Spatially-resolved carrier profiles in micro-PL experiments

As explained in the previous section, the use of a micro setup configuration in PL spectroscopy experiments intrinsically leads to high carrier densities. The level and volume distribution below the illuminated surface of such high carrier densities is highly affected by different experimental parameters such as:

- power level
- lense magnification
- excitation wavelength

In order to analyze the effect of these parameters on the charge density profile below the sample surface, we have simulated the electron density in a 0.5  $\Omega\text{cm}$  p-type c-Si wafer under different illumination conditions correlated to the parameters listed above. On the one hand, the carrier concentration profile along  $z$  direction (wafer depth) was simulated by PC1D. On the other hand, the carrier profile in the  $xy$  plane (corresponding to the sample surface and, as we will

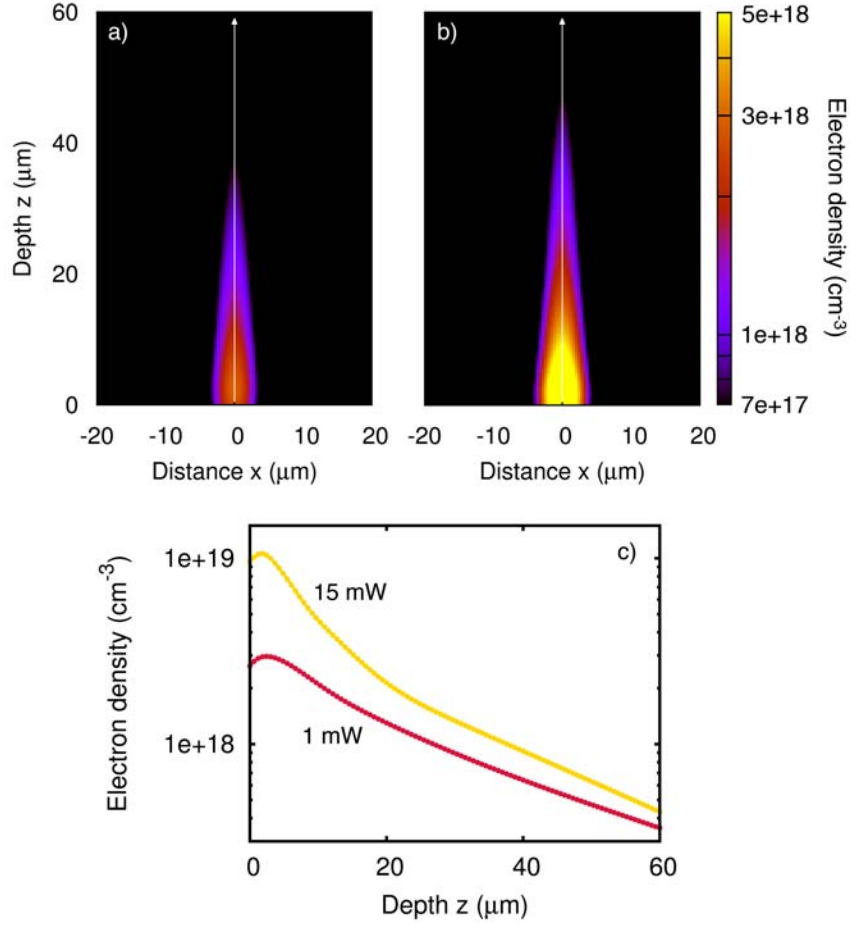


**Figure 3.3:** Simulated electron density maps below an illuminated Si surface originated by 1 mW (a) and 15 mW (b) 633 nm light beam focalized onto the sample surface by a x100 objective. The carrier profiles along the indicated (white arrow) depth  $z$  direction are also represented (c).

see, perpendicular to the represented maps) was considered to draw a Gaussian decay. To carry out the simulations we have considered a bulk lifetime of  $0.5 \mu\text{s}$  and surface recombination velocities ranging from  $1 \times 10^4$  to  $1 \times 10^5 \text{ cm s}^{-1}$ .

The more evident parameter affecting the carrier density profile below the sample surface is the power level of the incoming light beam. Figure 3.3 shows the electron density profiles corresponding to a 1 mW (a) and a 15 mW (b) 633 nm monochromatic light beam focalized onto the sample surface by a x100 microscopic objective. Because of the high focalization level, electron densities around  $3 \times 10^{18} \text{ cm}^{-3}$  are achieved with moderate power levels of 1 mW. In the case of using higher power levels, the electron density can reach values

### 3.1. Photoluminescence (PL) spectroscopy

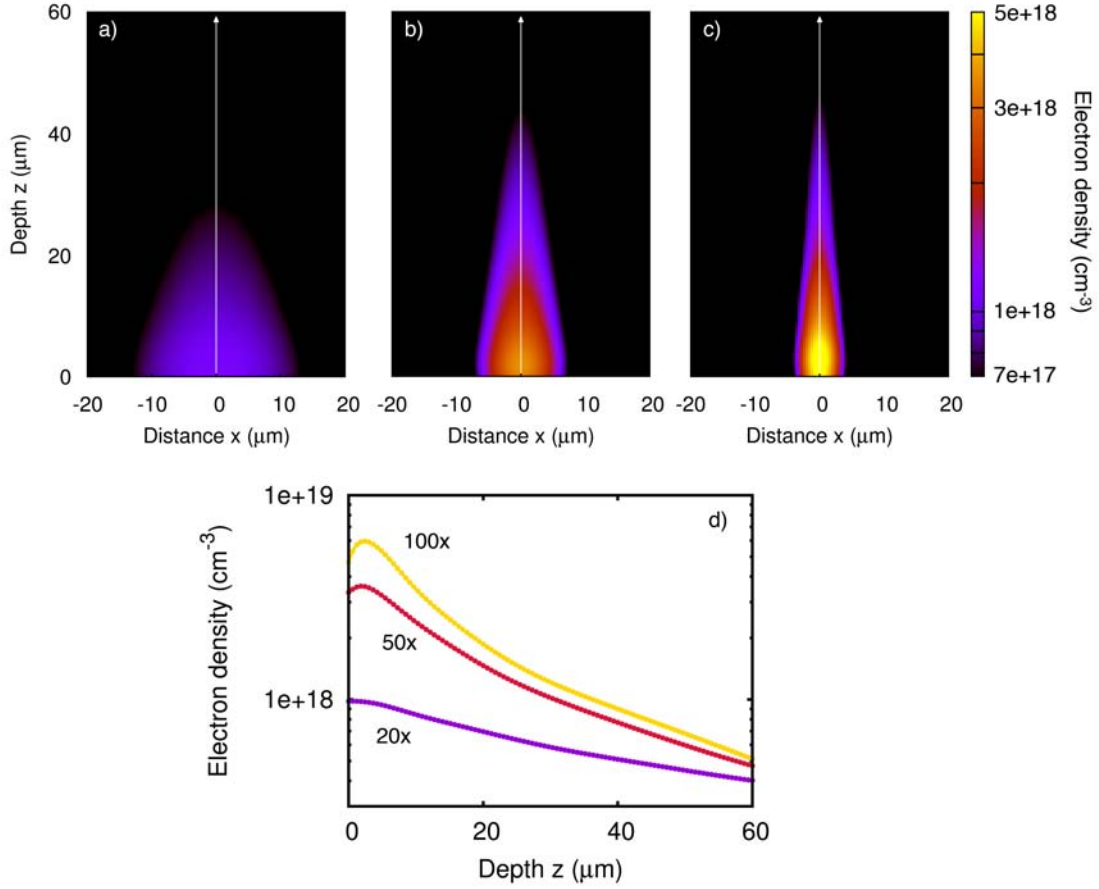


**Figure 3.4:** Simulated electron density maps below the illuminated Si surface assuming a 5 mW illumination from a 633 nm light beam being focalized onto the sample surface by a x20 (a), x50 (b) and x100 (c) objective. The carrier profiles along the indicated (white arrow) depth  $z$  direction are also represented (c).

above  $1 \times 10^{19} \text{ cm}^{-3}$ . As it can be clearly observed in Figure 3.3c, the 15 mW electron density curve shows a higher decay respect the 1 mW curve, specially along the first 20  $\mu\text{m}$  below the surface. Hence, the difference between carrier concentrations is larger the closer to the surface. This is induced by the low carrier lifetime at the bulk, and the corresponding low diffusion length, which tend to equalize the carrier densities at deeper points of the wafer thickness. As mentioned in the previous section, another important observation is the local decay of the carrier density observed at the first 5  $\mu\text{m}$  below the free-surface as a result of the elevated surface recombination velocity.

Concerning the effect of the focalization lense magnification, we illustrate in Figure 3.4 the carrier density distribution associated to micro-PL measure-

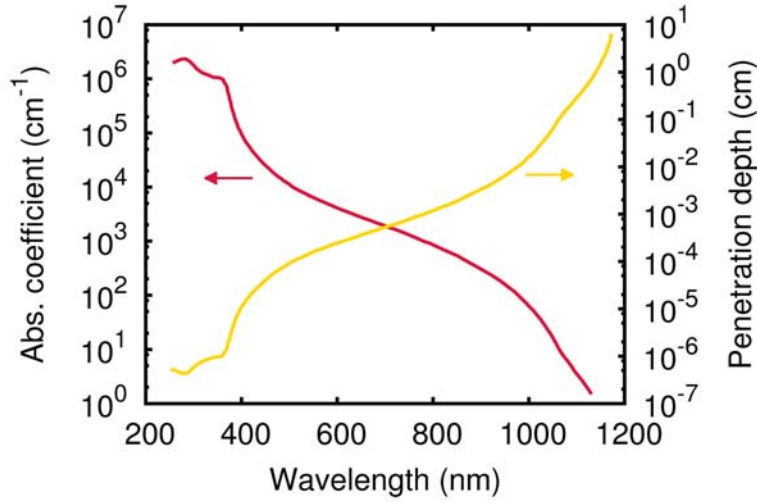


**Figure 3.5:** Silicon absorption coefficient and corresponding penetration depth against wavelength.

ments in which the excitation light beam is focalized onto the sample surface by a x20, x50 and x100 objective. For these calculations, the excitation wavelength and the laser power onto the sample surface were considered to be 633 nm and 5 mW, respectively. In terms of electron density level and electron density profile, the results here show a similar trend than that observed in Figure 3.3. Since for a given power level the power density (incoming photons per unit area) increases as the objective magnification increases, i.e. the illuminated area decreases, the use of objectives with higher magnifications intrinsically leads to higher carrier densities.

Nevertheless, an even further important feature observed in these calculations is the dependence of the objective magnification on the resultant lateral dimensions of the light beam. As it can be clearly observed in maps a, b and c of Figure 3.4, there is a systematic decrease of the x distance being illuminated, the higher the magnification of the objective. Thus, in addition to an increase of the charge density achieved, the use of higher magnification objectives also leads to a decrease of the material volume in which carriers are photo generated. This fact has important implication in terms of the lateral resolution achieved by micro-PL measurements.

Finally, also the wavelength of the excitation light beam affects the profile shape of the photo-generated carrier density. This is basically due to the dependence of the c-Si absorption coefficient on the wavelength (see Figure 3.5).

### 3.1. Photoluminescence (PL) spectroscopy

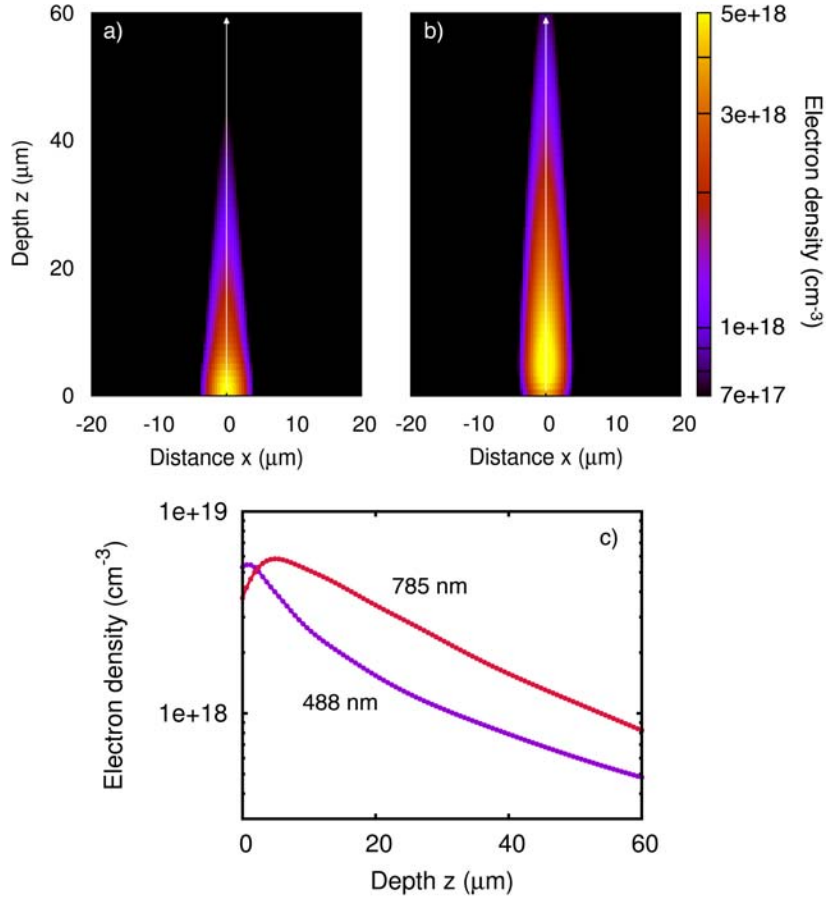


**Figure 3.6:** Simulated electron density maps below the illuminated Si surface originated by a 5 mW light beam focalized onto the sample surface by a 100x objective with a corresponding wavelength of 488 nm (a) and 785 nm (b). The carrier profiles along the depth  $z$  direction are also represented (c).

Keeping this dependence in mind, we can analyze the calculations of the electron density distribution in micro-PL measurements for both 480 nm and 785 nm illumination (Figure 3.6). Since the penetration depth linked to the 488 nm illumination is significantly lower ( $1\text{ }\mu\text{m}$ ) in front of the one related to the 785 nm excitation ( $10\text{ }\mu\text{m}$ ), the 488 nm photons are absorbed much closer to the surface. As we can observe in Figure 3.6c, this fact has important implications in the carrier density profiles at the sub-surface region. The electron density profile of the 488 nm illumination shows a slightly higher electron density at the very close region of the free-surface. From this region with a carrier density maximum, the curve draws a strong decay along the first  $10\text{ }\mu\text{m}$  below

the illuminated surface. In contrast, the 785 nm electron density profile shows a much lower decay. Moreover, it evidences respect the 488 nm curve an even higher electron density maximum point around 5  $\mu\text{m}$  below the surface. Since 785 nm photons are absorbed across a deeper material volume, such a maximum electron density maximum can be explained by a lower affectation of the surface recombination, which enlarges the total number of photons below the surface. All these facts, explain well the much higher resolution in Z direction associated to micro-PL measurements that are performed with shorter wavelengths.

In conclusion, for the design and development of micro-PL measurements, it is important to bear in mind two important features: 1) the use of focalization lenses with higher magnification leads to higher lateral resolution, and 2) the use of lower excitation wavelengths leads to much more sensitivity to surface phenomena.

### **3.1.3 Low-temperature micro-PL spectroscopy**

Low-temperature micro-PL measurements have been also used in this work for the characterization of  $\text{Al}_2\text{O}_3$ -passivated c-Si wafers. With decreasing temperature, phonon population decreases abruptly and both thermal ionization of impurity-bounded carriers and thermal dissociation of excitons is increasingly suppressed. As schematically depicted in Figure 3.7, radiative recombination processes at room temperature are dominated by band-to-band transition between free carriers. However, with decreasing temperatures, both free-bound transitions and radiative recombination of excitons (i.e. free exciton as well as bound excitons) subsequently set in. This fact leads to a qualitative change in the PL emission of bulk Si. In comparison to room-temperature PL measurements, where quantitative information concerning the conversion efficiency of PV materials can be obtained (see Section 3.1.1), low-temperature PL measurements are used to obtain qualitative and fundamental information about the material properties.

#### **3.1.3.1 Free-bound (FB) transitions**

In non ideal semiconductors, the presence of donor or acceptor impurities intrinsically leads to the existence of localized states which can give rise to the so-called free-to-bound (FB) transitions. In particular, these transitions are described by recombination processes between free carriers in the bands and



### 3.1. Photoluminescence (PL) spectroscopy



**Figure 3.7:** Scheme showing the different type of PL transitions as a function of the temperature.

carriers bounded to the localized states within the band gap. Thus, for p-type materials, conduction-band-to-acceptor transitions ( $e-A^0$ ) may occur, whereas for n-type materials, valence-band-to-donor transitions ( $p-D^0$ ) may be present. The luminescence yield of transitions involving localized states generally increases with decreasing temperature owing to the suppression of the thermal emission of trapped carriers to the conduction band. The dependence of the FB transitions luminescence yield on temperature is described by:

$$PL_{\text{yield}} = \frac{1}{1 + C \exp\left(\frac{-E_a}{k_B T}\right)}, \quad (3.12)$$

where  $C$  is a constant which is proportional to  $T^{3/2}$  and  $E_a$  is the activation energy, which in this case represents the ionization energy of the impurity state.

#### 3.1.3.2 Excitons

At temperatures below 80 K, the thermal energy is so low that it is not enough to thermally dissociate the photo generated excitons. Hence, recombination events arising from electron-hole pairs bound to each other by their Coulomb interaction, the so-called free excitons (FE), can be observed. The thermal dependence of the FE luminescence yield can be described again by Equation (3.12), where in this case the activation energy corresponds to the exciton binding energy. For instance, for silicon, a FE binding energy of 15 meV has been experimentally and theoretically obtained [59].

The transition energy of FE ( $E_{FE}$ ) can be simply expressed by:

$$E_{FE} = E_g - E_x, \quad (3.13)$$

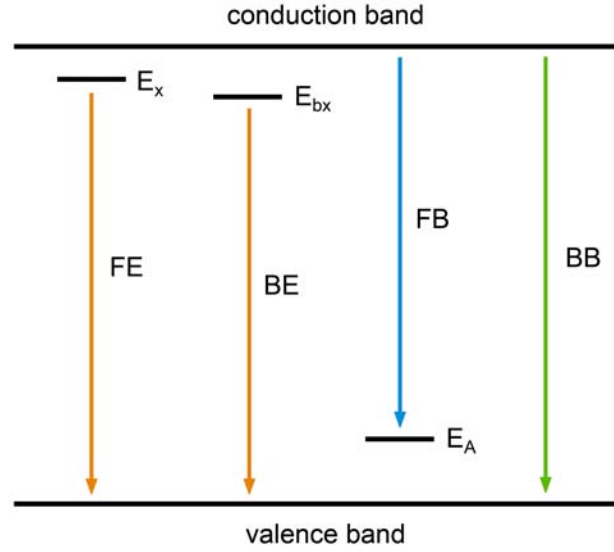


**Figure 3.8:** Different optical transitions that can take place in a PL experiment. Scheme adapted from [60].

where  $E_g$  is the band gap and  $E_x$  is the exciton binding energy.

Free excitons can get easily bound to impurities, leading to the so-called bound excitons (BE). Due to the interaction with the impurity, their binding energy changes slightly, and therefore, also changes their transition energy. In analogy with Equation (3.13), the transition energy for bound exciton ( $E_{BE}$ ) emission is given by:

$$E_{BE} = E_g - E_{bx} , \quad (3.14)$$

where  $E_{bx}$  corresponds to the binding energy of the complex. Since the exciton-impurity interaction has typically associated a slightly higher energy than the exciton itself, the  $E_{BE}$  PL emission line typically appears in the PL spectra at slightly lower values of energy.

A summary of the different optical transitions that can take place in a PL measurement is illustrated in Figure 3.8.

## 3.2 Raman spectroscopy

Raman spectroscopy is based on the analysis of the Raman scattering effect discovered by C. V. Raman in 1928 [61]. The Raman scattering process is the

### 3.2. Raman spectroscopy

---

result of an exchange of energy between an incident light beam and certain vibrational, rotational or other low-frequency modes of the system under study. Thus, the frequency of the inelastic scattered light is shifted respect to the incident light frequency, allowing the determination of such fundamental excitation modes of the material. Because only one photon out of the  $10^6$ - $10^{12}$  incident photons is inelastically or Raman scattered, high intensity excitation lasers and very sensitive detectors are required to study the Raman effect. Raman spectroscopy can be fundamentally used to identify materials by means of the determination of material vibrational levels, as well as to detect structural changes that alter the crystal symmetry, hence alter the material vibrational modes. In the latter case, real-time measurements while changing physical parameters such as temperature or pressure are commonly used.

In analogy to micro-PL spectroscopy, the term micro-Raman spectroscopy is employed when the excitation light beam is focused on the sample surface by microscopic objectives, allowing much greater lateral resolution than conventional Raman spectroscopy setups. Micro-Raman spectroscopy can be applied for an enormous number of different types of studies. In the present work, micro-Raman spectroscopy has been used to carry out a spatially-resolved characterization of LFCs processed in  $\text{Al}_2\text{O}_3$ -passivated c-Si wafers.

#### 3.2.1 Fundamentals of Raman spectroscopy

From a quantum mechanical point of view, the Raman process can be described as follows: A photon  $k_i$ ,  $w_i$  (being  $k_i$  the direction and  $w_i$  the frequency) is absorbed by the material and an electron is excited from a ground energy state to a higher energy state. In a very few number of cases, such an excited electron interacts with a phonon  $q_j$ ,  $w_j$  (where  $q_j$  is the wave-vector and  $w_j$  is the frequency), resulting in a gain or a loss of energy. Then, when this electron recombines coming back to the ground state, a photon  $k_s$ ,  $w_s$  is emitted. For anti-Stokes Raman scattering we have  $w_s = w_i + w_j$ , whereas for Stokes Raman scattering  $w_s = w_i - w_j$ . The Stokes Raman scattering has a higher probability, so in most cases, it is the signal measured and analyzed. The relation between scattered photons frequency and wavelength is described by the following expression:

$$\Delta w (\text{cm}^{-1}) = \left( \frac{1}{\lambda_0 (\text{nm})} - \frac{1}{\lambda_1 (\text{nm})} \right) \times 10^7, \quad (3.15)$$

where  $\lambda_0$  is the wavelength of the incident photons and  $\lambda_1$  is the wavelength of the scattered ones.

### 3.2.2 Raman spectrum of c-Si

The Raman spectrum of c-Si is characterized by a main Raman line positioned at  $520.9 \text{ cm}^{-1}$  (see Figure 3.9a). This peak is correlated to the zone-edge optical phonon at  $k=0$  (being  $k$  is the wave-vector of the mode) [62, 63, 64]. This is the only one Raman active Si phonon, and will be referred as first-order silicon Raman peak throughout the this section. Behind its apparent simplicity, the study of some specific features of the line shape of this Raman peak can give us very important information about certain c-Si properties such as mechanical stress, doping, composition and crystallinity, among others. This fact, together with the high lateral resolution associated to micro-Raman spectroscopy, convert this technique as a very powerful tool for the characterization of c-Si based photovoltaic devices. The different Raman peak features and the related information that can be extracted from them are represented in Figure 3.9 and described below:

- **Shift of the peak position (Figure 3.9b):** It was in 1970 when Anastasakis *et al.* [69] observed that first order c-Si Raman peak suffered a certain shift under uniaxial external stress. The work triggered the application of Raman spectroscopy for measuring internal stress in semiconductor material structures. A tensile stressed structure leads to a Raman peak shift towards lower frequencies, whereas a compressed stressed structure results in a peak shift towards higher frequencies [65].
- **Broadening of the peak left flank (Figure 3.9c):** Changes on the left shoulder of the c-Si Raman peak are related to variations on the Si crystalline fraction. A decrease of the crystalline fraction, which takes place for instance in micro-crystalline Si, is qualitatively observed by a broadening of the peak left flank. Compared to c-Si, the Raman spectrum of amorphous-Si is characterized by a less intense Raman peak positioned at  $480 \text{ cm}^{-1}$ . Hence, the broadening observed in less crystalline silicon samples is consequence of the transition from the c-Si state to the amorphous-Si state [66, 67]. Despite being a less importance feature, microcrystalline Si Raman peak also evidence an increase of the peak FWHM.

### 3.2. Raman spectroscopy

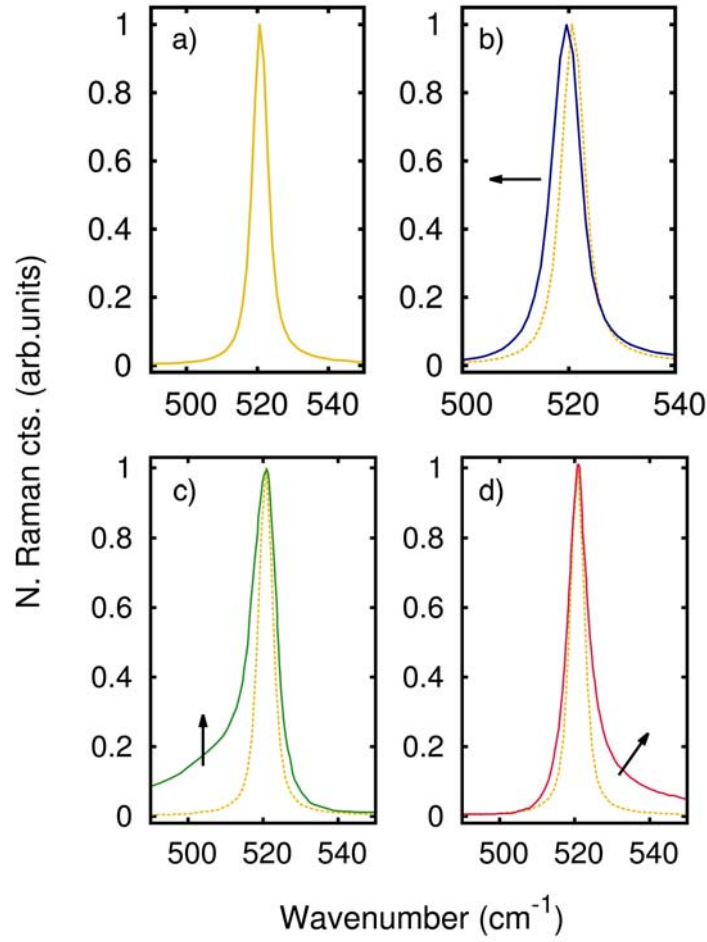


**Figure 3.9:** The c-Si Raman spectrum is characterized by the first order Si Raman peak positioned at  $520.9 \text{ cm}^{-1}$  (a). Variations in the Raman peak line shape such as a shift of the peak maximum (b) [65], a broadening of the left peak flank (c) [66, 67], and the presence of asymmetric features in the right peak flank (d) [68] are associated to changes on specific c-Si properties.

- **Asymmetry of the Raman peak (Figure 3.9d):** Asymmetric features appearing on the right side of the c-Si Raman peak are associated to the so-called Fano resonance. This phenomenon is observed in samples with a substantial increase in the doping density, i.e. above  $1 \times 10^{10} \text{ cm}^{-3}$  [68], and it results from the resonant interaction between the discrete phonon states and a continuum of hole states. Due to its doping dependence, Fano resonances can be used to monitor doping density variations in c-Si. Since this approach is used in this thesis for studying the doping

density profiles in LFCs, details about the Fano effect are addressed in Chapter 6.

- **Widening of the peak half-width (not shown in Figure 3.9):** By definition, the half-width of the Raman peak, known as Full Width at Half Maximum (FWHM), is reciprocally related to the lifetime of the phonon participating in the electron-phonon scattering. Different parameters have been proven to affect the Raman peak FWHM. For instance, the temperature dependence of the Raman peak FWHM has been widely studied in GaN [70] and Si [64]. Concerning the dependence of Si properties that are of interest in this thesis, an increase of the first order Si Raman peak FWHM can be observed by an increase of the doping density and/or by a decrease of the Si crystalline fraction.

### 3.3 Scanning probe microscopies

The invention of the Scanning Tunneling Microscope (STM) in 1985 and the Atomic Force Microscope (AFM) in 1986 by Binnig and Rohrer redefined the concept of microscopy and gave rise to a new family of characterization instruments known as Scanning Probe Microscopes (SPMs). SPMs are used in the study of surface properties of materials from the micron to the atomic level. The operation principle of SPMs is represented by the scheme of Figure 3.10. In such, the material surface under study is scanned by a sharp tip, which senses different properties of the material. For instance, STM, was the first instrument to atomically resolve real-space images of surfaces, and is based on the measurement of a tunneling current between a sharp conducting tip and a conducting sample. On his behalf, AFM has become one of the most popular SPMs. In this case, a very sharp tip of few microns long and often less than 10 nm in diameter is located at the free end of a cantilever. This cantilever scans the sample surface (or the sample surface is scanned over the cantilever) and the cantilever deflection that changes according to the surface shape is monitored to generate a map to of the surface topography. Magnetic Force Microscopy (MFM) and Scanning Near-field Optical Microscopy (SNOM) are other examples of the many SPMs which use different interactions to probe different properties of the surface. In the present thesis, three different types or variations of SPM techniques have been used. First, Kelvin Probe Force Microscopy (KPFM) has been used to characterize the band bending of a Metal-

### 3.3. Scanning probe microscopies

---

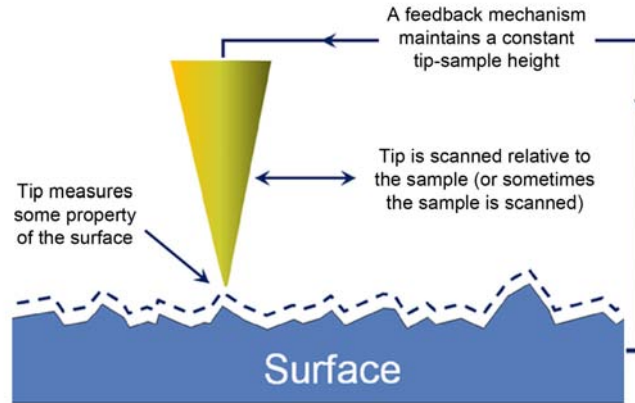


**Figure 3.10:** Representation of operation principle of scanning probe microscopies (SPMs).

Oxide-Semiconductor (MOS) interface at the rear part of a passivated emitter solar cell. In addition, conductive-AFM (c-AFM) has been employed to obtain conductive maps of point contacts processed in  $\text{Al}_2\text{O}_3$ -passivated c-Si wafers. Finally, as we will see in a supplementary study presented in the appendix A, conventional AFM measurements were applied in real-time during heating of different organic PV thin films. This methodology, referred as temperature-dependent AFM, was used to determine the cold-crystallization transition of organic thin-films. The details about its application and operation will be exposed in the mentioned appendix

#### 3.3.1 Kelvin Probe Force Microscopy (KPFM)

KPFM uses the same fundamental principle as the macroscopic probe technique [71]. KPFM was first introduced by Nonnenmacher *et al.* [72] for measuring the local contact potential difference (CPD) between a conducting AFM tip and the sample. In particular, this CPD is measured by sensing an electrostatic force between tip and sample, which results from the difference between tip and sample work functions [73, 74, 75, 76]. Figure 3.11 depicts the operation principle of KPFM by means of representing the variations on the energy level diagram of the tip and sample surface. Figure 3.11a shows the energy levels of tip and sample when they are not electrically connected. When the two materials are in electrical contact through their back side (Figure 3.11b), Fermi levels of tip and sample line-up and electrons flow from the material with the lower

work function (weak electron binding) to the one with the higher work function (strong electron binding). This generates opposite charges on the materials surface, and therefore, an electrostatic force of magnitude  $V_{CPD}$  is generated on the contact area between tip and sample. This force can be compensated by applying an external bias ( $V_{DC}$ ) with the same magnitude and opposite direction as  $V_{CPD}$  (Figure 3.11c). KPFM is based on monitoring the applied voltage  $V_{DC}$  that eliminates the surface charge in the tip-sample contact area. The CPD appearing between tip and sample is equal to the difference between their respective work functions and is defined as:

$$V_{CPD} = \frac{\phi_{tip} - \phi_{sample}}{-q} \quad (3.16)$$

where  $\Phi_{tip}$  is the tip work function,  $\phi_{sample}$  is the sample work function, and  $q$  is the electronic charge.

Since its introduction, KPFM has been widely used to study a wide range of material surfaces and real devices. For instance, it has been used to characterize the surface band bending of thin films [77] and also to obtain surface potential (SP) maps of pn junction diodes [78] or organic solar cells (OSC) [79]. Moreover, as KPFM combines a very high spatial resolution (up to tens of nanometers) with the possibility to develop electronic band-related measurements, cross-sectional KPFM measurements can be considered a unique and powerful tool to perform a local study of potential profiles across multi-layer devices. For instance, KPFM has been used to characterize pn junction cross-sections [80], or also to study the internal potential profile across solar cells [81, 82].

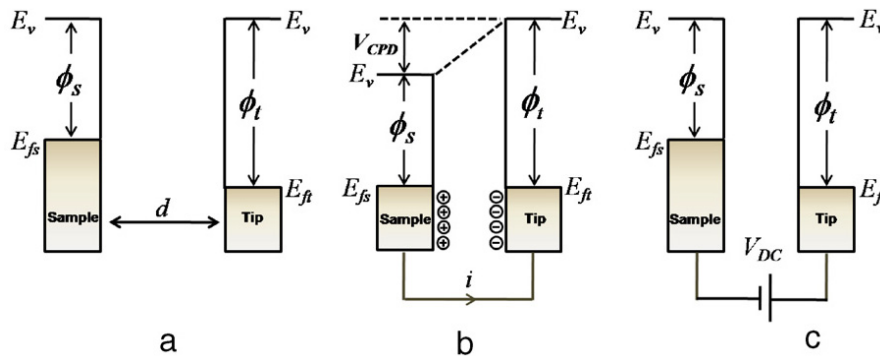


**Figure 3.11:** Band diagram of tip and sample representing the operation principle of kelvin probe force microscopy (KPFM).



### 3.3.2 Conductive atomic force microscopy

One of the simplest ways for studying electrical properties at the sub micron level is by applying a voltage between the sample and a conductive AFM tip, and measuring the resulting current flowing between them. Two different types of measurements, dynamic and static, can be applied. In the former both topography and current maps are simultaneously recorded while the tip scans the sample surface at a constant force. In the later, the tip is kept statically at a specific point of the sample surface and an I-V characteristic is recorded. In the last case, the obtained values of current are more reliable since the tip-sample force is easily maintained at a constant value.

Conductive probes are usually obtained by coating standard Si probes by conductive thin films. These can be based on metals (Pt/Ir is one of the most common), doped diamond or highly doped Si. The choice of a specific conductive coating frequently depends on the work function matching between the tip and sample.

## 3.4 Other characterization techniques

### 3.4.1 Quasi-steady state photoconductance

Quasy-steady-state photoconductance (QSSPC) is a contact-less non-invasive technique introduced by R. A. Sinton and A. Cuevas in 1996 [83, 84] for measuring the effective lifetime ( $\tau_{\text{eff}}$ ) from the absolute value of the photoconductance generated by a flash lamp illumination. The experimental setup of the QSSPC technique is illustrated in Figure 3.12. In this technique, the decay time of the light source is slow enough to allow the photo-generation rate be balanced by the total recombination within the wafer at every instant of time (this is the origin of the term quasi-steady state). Thus, as described in Section 3.1.1.1, for a  $\tau_{\text{eff}}$  much greater than the light decay time, the derivative term of the continuity Equation (3.1) is negligible, and therefore,  $\tau_{\text{eff}}$  depends exclusively on  $\Delta n$  and  $G$  (see Equation (3.4)). These are the parameters measured experimentally by the QSSPC technique.

The average excess carrier density  $\Delta n = \Delta p$  is calculated by the photoconductance signal ( $\Delta\sigma$ ), which is sensed by a coil that is inductively coupled to the sample under study. Thus,  $\Delta n_{\text{av}}$  can be determined via:

$$\Delta(t) = \frac{\Delta\sigma(t)}{q(\mu_n + \mu_p)W}, \quad (3.17)$$

where  $W$  is the wafer thickness and  $\mu_n$  and  $\mu_p$  are the electron and hole mobilities.

On the other hand,  $G(t)$  is calculated using appropriate calibration functions from the averaged illuminated intensity  $I_{av}(t)$ , which is measured from a calibrated reference solar cell. Thus, the generation rate within the sample can be determined by:

$$G(t) = \frac{I_{av}(t) f_{abs} \Phi^{1sun}}{W}, \quad (3.18)$$

where  $\Phi^{1sun}$  is the flux of photons corresponding to an irradiance of 1 sun, and  $f_{abs}$  is the fraction of the total irradiated photons absorbed by the material.

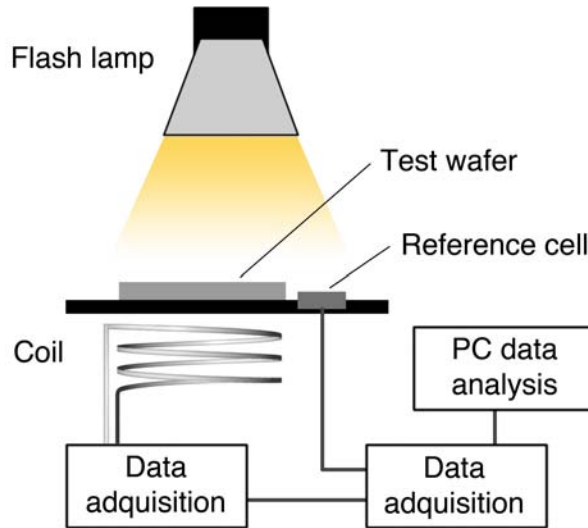
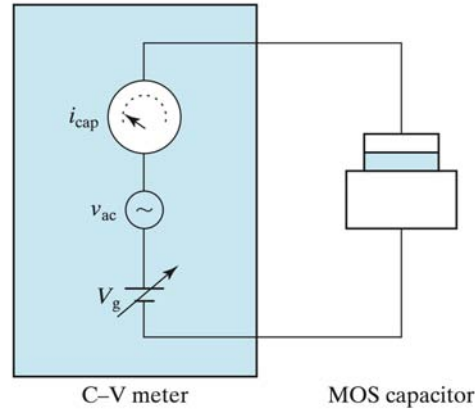


Figure 3.12: Experimental setup of the QSSPC technique.

### 3.4.2 Capacitance-Voltage curves

The capacitance-voltage (C-V) technique is a powerful and widely used tool for studying the oxide quality of metal-oxide-semiconductor (MOS) structures, as the one we can find at the front or rear side of passivated c-Si solar cells. In particular, the C-V technique is exclusively used in this thesis in order to determine the charge level associated to different  $\text{Al}_2\text{O}_3$  passivation layers. Before discussing the oxide charge calculation procedure, both the C-V relationship and the C-V curve are introduced.

### 3.4. Other characterization techniques



**Figure 3.13:** Scheme illustrating a C-V measurement setup [85].

The C-V curve is usually measured with a C-V meter (see Figure 3.13), which applies a DC bias voltage and a small sinusoidal signal (1 kHz-10 MHz) to the MOS capacitor. The resulting charge variation gives rise to the capacitance which is defined as:

$$C = \frac{dQ_g}{dV_g}, \quad (3.19)$$

where  $Q_g$  and  $V_g$  are the gate charge and gate voltage, respectively. Capacitance is commonly given in units of farad/unit area. Figure 3.14 illustrates a high-frequency C-V curve corresponding to an Al/Al<sub>2</sub>O<sub>3</sub>/p-type c-Si MOS capacitor. A C-V curve can be divided in the three characteristic operation regions of a MOS capacitor: accumulation, depletion and inversion. As it can be seen, having a p-type c-Si base, accumulation occurs at negative polarities, whereas inversion occurs at positive polarities. Important and diverse information about MOS capacitor features such as gate oxide thickness, substrate doping concentration, threshold voltage, flat-band voltage and oxide charge can be deduced from C-V characteristics. Here, we focus on the determination of the oxide charge.

#### 3.4.2.1 Oxide charge determination

The effective oxide charge ( $Q_{eff}$ ) is defined as the sum of the different charge types we can find in a MOS structure. These are: the oxide fixed charge ( $Q_f$ ), the mobile charge ( $Q_m$ ) and the oxide trapped charge ( $Q_{trap}$ ). Simple room temperature C-V measurements do not distinguish the three components of

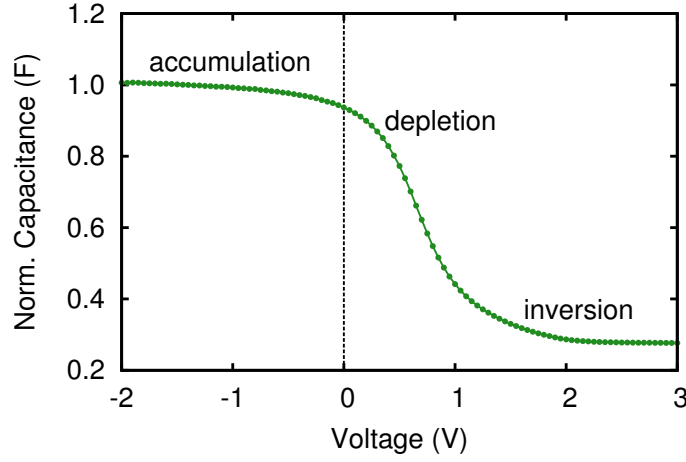


**Figure 3.14:** An example of a C-V curve.

$Q_{\text{eff}}$ . Since the charge profile in the oxide is not known, the calculation of  $Q_{\text{eff}}$  is based on the assumption that the charge is located in a sheet at the silicon-oxide interface and is given by:

$$V_{\text{fb}} = \varphi_{\text{ms}} - \frac{Q_{\text{eff}}}{C_{\text{ox}}}, \quad (3.20)$$

where  $V_{\text{fb}}$  is the flat band voltage,  $\varphi_{\text{ms}}$  is the metal-semiconductor work function and  $C_{\text{ox}}$  is the capacitance corresponding to the oxide. Qualitatively, we can identify the presence of oxide charge by a shift of the C-V curve respect  $V=0$ . For positive oxide charges, C-V shifts towards negative voltages. In contrast, for negative charges, C-V curve shifts towards positive voltages.

# 4

## Cross-sectional KPFM study of Al/SiO<sub>2</sub>/c-Si stacks

*In this chapter, we use Kelvin Probe Force Microscopy (KPFM) to perform for the first time a high-resolution spatially-resolved surface potential (SP) study of a cleaved Al/SiO<sub>2</sub>/Si Metal-Oxide-Semiconductor (MOS) cross-section. In the first section, SP maps of MOS cross-section have been used to study different MOS features such as Si band bending and depletion width. In the second section, KPFM measurements have been performed varying the bias applied to the Al gate. This has allowed to study other important MOS features such as the flat band voltage and the amount of charges at the MOS interface. Due to the complexity of the measurement procedure, and to the observation of some unexpected features in the obtained results, we present this chapter as an exploratory introduction of a KPFM methodology to characterize MOS structures. With further improvements, the presented procedure could represent a valuable methodology to study the different MOS features with a spatial resolution down to few tens of nanometers.*

## 4.1 Introduction

The Metal-Oxide-Semiconductor (MOS) capacitor is an important structure that is present in a very wide range of semiconductor devices. For instance, it forms an essential part of a MOS Field-Effect Transistor (MOSFET), which in turn, is the fundamental part of many electronic and optoelectronic devices such as Integrated Circuits (ICs) or Charge Coupled Devices (CCDs). Also, it can be found on the front or rear side of c-Si solar cells. The study of the MOS capacitor behavior under a varying bias applied between the substrate and the gate is a powerful way to investigate the quality of both the oxide layer and the oxide-silicon interface. One of the most common techniques in order to do so is the measurement of Capacitance-Voltage (C-V) curves (see Section 3.4.2). Through a deep analysis of C-V curves one can obtain an insight about the most relevant MOS features such as the flat band voltage, the threshold voltage or the level of interface charge. However, an important limitation of these macroscopic-type measurements is that no detailed or spatially-resolved information can be obtained. In the present chapter, we use Kelvin Probe Force Microscopy (KPFM) (see Section ) in order to carry out a high-resolution spatially-resolved characterization of a cleaved Al/SiO<sub>2</sub>/c-Si MOS stack.

## 4.2 Experimental details

### 4.2.1 Materials and samples

MOS structures under study were based on 2.5  $\Omega\text{cm}$  boron-doped Float Zone (FZ) crystalline silicon (c-Si) wafers with a crystal orientation of (100) and a thickness of 250  $\mu\text{m}$ . MOS oxide barrier consisted of a 100 nm-thick silicon dioxide (SiO<sub>2</sub>) layer, which was grown on both sides of the c-Si wafer by thermal oxidation. After the oxidation process, a 2  $\mu\text{m}$ -thick top Al layer was deposited onto the previously obtained SiO<sub>2</sub>/c-Si/SiO<sub>2</sub> sample in order to form the gate electrode. Furthermore, a second Al contact was deposited at the bottom of the Al/SiO<sub>2</sub>/c-Si/SiO<sub>2</sub> sample. This back Al electrode was electrically connected to the Si base by means of the creation of laser-processed local base contacts. Thus, the Si base could be easily connected to the ground by this back Al electrode. Figure 4.1 shows the sample architecture and the experimental setup of cross-sectional KPFM measurements. As it can be seen, KPFM measurements were performed on top of the Al/SiO<sub>2</sub>/c-Si MOS. It is

## 4.2. Experimental details

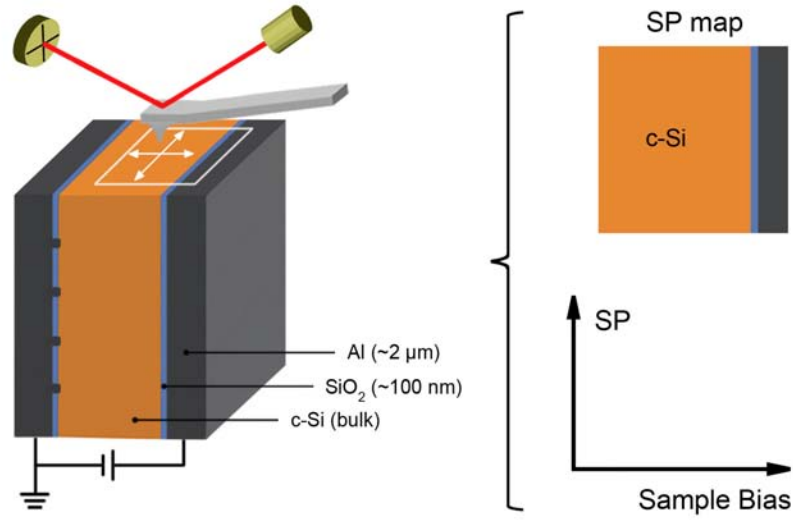


**Figure 4.1:** Experimental setup of KPFM measurements in MOS cross-sections based on Al/SiO<sub>2</sub>/c-Si stacks. As it can be observed, KPFM measurements can be performed under a varying bias applied to the Al gate. SP maps of MOS cross-section and SP vs Bias curves at selected points of the sample surface can be obtained..

worth to mention that samples had to be perfectly cleaved in order to obtain a clean and completely flat cross-section. Since drastic changes in sample height can decrease the stability of KPFM measurements, the obtention of a perfectly cleaved cross-section was an indispensable requirement in order to obtain consistent KPFM results.

### 4.2.2 Measurement modes

KPFM microscopy offers two different measurement modes. The most common, the so-called single-pass KPFM, is based on scan the material surface to be studied and record simultaneously both the topography and the SP signal. This measurement procedure can also be employed while applying a DC voltage to the sample. In our case, the voltage is applied to the Al gate and the Si is connected to the ground. Moreover, there is the possibility to use a second measurement procedure, the so-called KPFM spectroscopy. This is a static measurements mode where the tip is kept at a certain point of the sam-

ple surface, and the SP signal is recorded as a function of the applied sample bias.

### 4.2.3 Equipment and measurement details

KPFM measurements were performed using a Pico+ SPM (Agilent Technologies) equipped with a three lock-in module setup. SP maps were recorded in single-pass KPFM by means of AM (amplitude modulation) mode. In order to reduce capillary forces, measurements were performed in a nitrogen-rich atmosphere using an environmental chamber. Pt/Ir coated silicon tips with a force constant of 5 N/m were used to carry out the measurements.

## 4.3 Towards reaching the MOS interface

Due to the small thickness of a MOS stack, the method employed to reach the MOS cross-section is not trivial. The complexity relies on the fact, that the AFM tip has to reach the MOS interface without getting the end of the Al electrode, i.e. the end of the cleaved sample. In case of the tip would fall out of the sample, the piezo-tube of the KPFM equipment would loss the feedback, then the AFM tip could break when trying to scan in the reverse direction.

The procedure followed to properly reach the MOS cross-section is described in Figure 4.2. First, the AFM tip is engaged on the c-Si bulk cross-section. Once the tip is engaged, the scanning surface area is progressively moved towards the MOS interface until the Al electrode is observed. The displacement of the scanning surface area has to be done in steps with a maximum

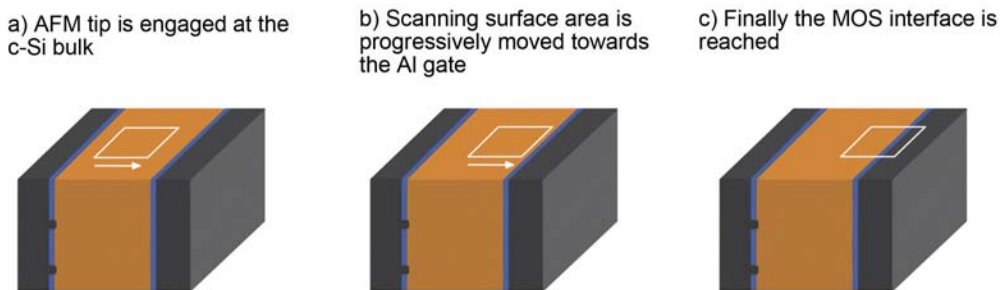


**Figure 4.2:** Sketch illustrating the different steps of the procedure used to reach the Al/SiO<sub>2</sub>/c-Si MOS interface.



### 4.3. Towards reaching the MOS interface

distance of 2  $\mu\text{m}$ , i.e. the distance between the end of the bulk Si and the end of the sample cross-section. Hence, this part of the procedure can require high amounts of time. Usually, the Al electrode is identified by a drastic increase of the SP signal. A change in the surface morphology can be observed in some cases.

#### 4.3.1 Orientation-induced Si work function variations

An interesting observation throughout the localization of the MOS interface was the identification of different Si crystallographic planes. We believe that at local and specific surface regions of the Si wafer cross-section, the cleavage of the Si followed different crystallographic directions, leading to the presence of different crystallographic planes at specific points of the sample cross-section.

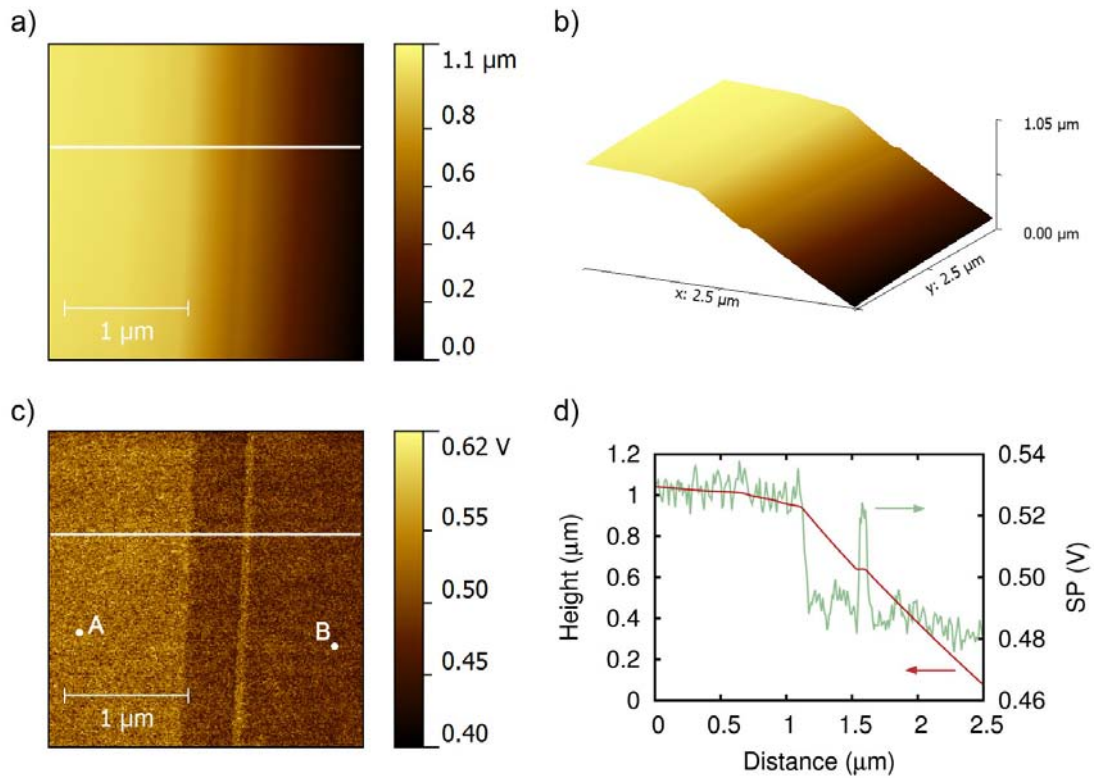


**Figure 4.3:** 2D (a) and 3D (b) topography maps of a cleaved Si wafer cross-section. Each one of the 4 identified planes has a characteristic SP correlated value, as deduced from the SP map (c). Topography and SP profiles (d) across the selected horizontal lines are also represented.

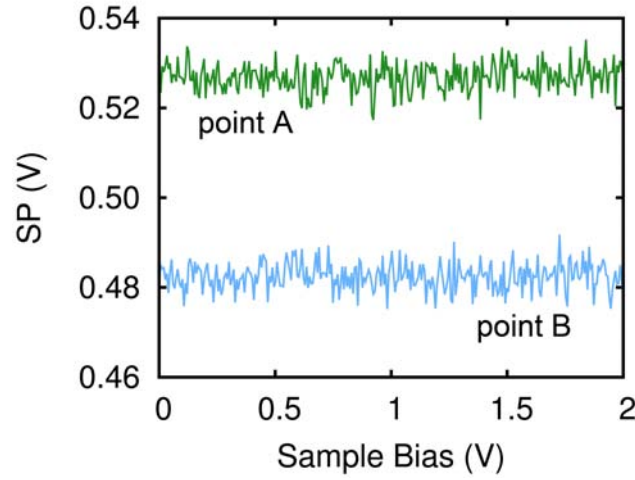


**Figure 4.4:** SP against applied bias to the Al gate of the two selected points in Figure 4.3c.

The topography (a) and SP (c) maps of a cleaved Si cross-section showing different cleavage planes are represented in Figure 4.3. For clarity, a 3D topography map (b) is also depicted.

As observed in the topography and SP profiles of Figure 4.3d, the scanned surface area shows 4 different planes with two correlated specific orientations. Each one of the two observed orientations has a specific SP correlated value, which is constant within the planes. The horizontal planes show a characteristic SP value of 0.53 V approximately, whereas tilted planes show a SP value of around 0.48 V. This results in a work function difference between planes of about 0.05 eV. The work function variation between different crystal orientations is produced by the presence of surface dipoles (induced by the breaking of the crystal network) and by the different atomic packing correlated to the different crystal planes. For c-Si, differences in work function ranging from 0.05 to 0.15 eV have been experimentally reported between (100), (110) and (111) crystal orientations [86].

The hypothesis about cleavage plans identification is strengthened by results presented in Figure 4.4. This panel represents the SP variation against Al gate bias of the two selected points in Figure 4.3c. As it can be seen, the SP value is constant, and therefore, not dependent with the applied bias. This fact demonstrates that the recorded points are far away from the MOS interface, and therefore, all plans observed in Figure 4.3 correspond to the bulk c-Si.

## 4.4 MOS cross-section SP map

Figure 4.5 shows the topography (a) and the SP (b) maps of an Al/SiO<sub>2</sub>/Si MOS cross-section. In addition, the corresponding topography and SP profiles (c) are also represented. The larger and lower plane on the right-hand side of the topography profile corresponds to the Si wafer. The SiO<sub>2</sub>/c-Si interface (vertical dashed line) could be precisely identified by a drastic change of the slope in the topography profile. Hence, the SiO<sub>2</sub> layer should belong from the SiO<sub>2</sub>/c-Si interface until 100 nm towards to the left. The hypothetic location of the SiO<sub>2</sub> layer was represented in the plot by a gray colored area. As observed from the SP profile, the SP signal shows a lower value (right part of the dashed line) of about 0.15 V which corresponds to the Si substrate. Also, it can be identified a higher SP value corresponding to the Al (the very left part of the SP profile) that reaches a value of 0.85 V. The observed SP difference between the bulk Si and Al is therefore about 0.7 V. With this, we compare the observed

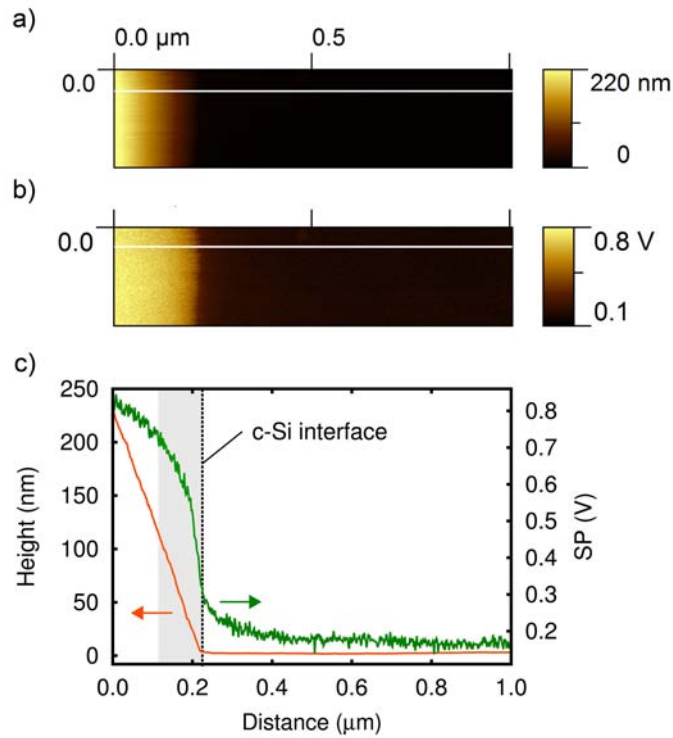


**Figure 4.5:** Topography (a) and surface potential (b) maps of an Al/SiO<sub>2</sub>/c-Si cross-section. Corresponding topography and surface potential (SP) profiles (c) are also represented.

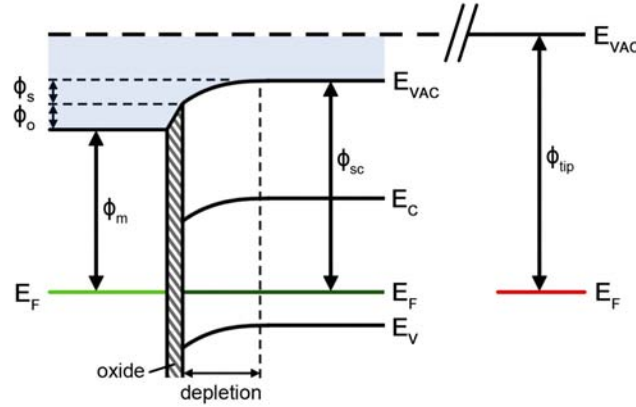


**Figure 4.6:** Energy band diagram of both the MOS structure and the KPFM tip. MOS structure is formed by an Al gate and a p-type Si body.  $E_{VAC}$ : vacuum energy;  $E_C$ : Conduction band energy;  $E_F$ : Fermi level energy;  $E_V$ : Valence band energy;  $\phi_{tip}$ : KPFM tip work function;  $\phi_{sc}$ : semiconductor work function;  $\phi_m$ : metal work function;  $\phi_s$ : Band bending-related potential;  $\phi_o$ : Oxide-related potential. The gray colored area represents the measured surface potential.

work function difference with the theoretical one. The work function of a semiconductor ( $\phi_{sc}$ ) is defined by:

$$\phi_{sc} = \chi + \frac{E_g}{2} + \phi_F, \quad (4.1)$$

being

$$\phi_F = \frac{k_B T}{q} \ln \left( \frac{N_A}{n_i} \right), \quad (4.2)$$

where  $\chi$  is the electron affinity,  $E_g$  is the band gap,  $\phi_F$  is the Fermi potential,  $k_B$  is the Boltzmann constant, i.e.  $8.617 \times 10^{-5} \text{ eV K}^{-1}$ ,  $T$  is the temperature,  $N_A$  is the density of acceptor impurities and  $n_i$  is the density of intrinsic impurities at the given temperature. For our  $2.5 \text{ } \Omega\text{cm}$  boron-doped FZ c-Si we obtain a work function of 4.9 eV. Taking the work function of Al, i.e.  $\sim 4.1 \text{ eV}$  [87], we have a theoretical work function difference between Si and Al of 0.8 eV which roughly agrees with the measured one, i.e. 0.7 eV.

An interesting feature observed in Figure 4.5 is the slight bending of the Si SP signal when reaching the SiO<sub>2</sub>/Si interface. The reasons of such SP signal bending can be deduced by observing in detail the sketch of Figure 4.6. This sketch represents the band diagram of the MOS cross-section during the KPFM measurement at 0 V of applied external bias, where the MOS structure

#### 4.5. SP under a varying bias

---

is at depletion regime. According to Equation (3.16) (see Section 3.3.1) the SP is defined by:

$$SP = \frac{\varphi_{\text{tip}} - \varphi_{\text{sample}}}{-q}, \quad (4.3)$$

where  $\varphi_{\text{tip}}$  is the tip work function,  $\varphi_{\text{sample}}$  is the sample work function and  $q$  is the electronic charge. During the KPFM measurement, the work function of the KPFM tip acts as a reference, and therefore, the measured SP is defined by the gray colored area of Figure 4.6. Thus, the small Si SP upward bending at the vicinity of the SiO<sub>2</sub>/Si interface observed in Figure 4.5c is correlated to the downward Si band bending induced by the MOS depletion. In this sense, the band bending ( $\varphi_s$ ) across the depletion region can be determined by rewriting the expression (4.3) in the form:

$$SP = \frac{\varphi_{\text{tip}} - \varphi_{\text{bulk.Si}} + \varphi_s}{-q}, \quad (4.4)$$

where  $\varphi_{\text{bulk.Si}}$  is the bulk Si work function. According to Equation (4.4) and the SP profile of Figure 4.5c it can be deduced a Si band bending at the MOS junction of about 0.15 V.

### 4.5 SP under a varying bias

We have also carried out KPFM measurements across the MOS junction by varying the bias between the c-Si substrate and the Al contact (the Si substrate is connected to the ground). With these bias-dependent KPFM measurements we want to study the response of the MOS capacitor and the possible presence of charges at the MOS interface. Figure 4.7 shows the SP profiles of the MOS cross-section at different bias applied to the Al gate. Note that here the SiO<sub>2</sub>/Si interface has been positioned at  $x=0$   $\mu\text{m}$  to compare the different SP profiles. The SiO<sub>2</sub>/Si interface is defined by the vertical dashed line. Again, an estimation of the 100 nm-thick oxide layer is represented by the gray colored area on the left side of the vertical dashed line.

As previously observed in Figure 4.5, when no external bias is applied to the gate, we observe a small upward SP bending, i.e., downward Si band bending, corresponding to the depletion situation of the MOS structure under study (look at the scheme of Figure 4.6). When positive bias are applied to the Al gate (i.e. gate Fermi level goes down), the upward SP bending observed in the

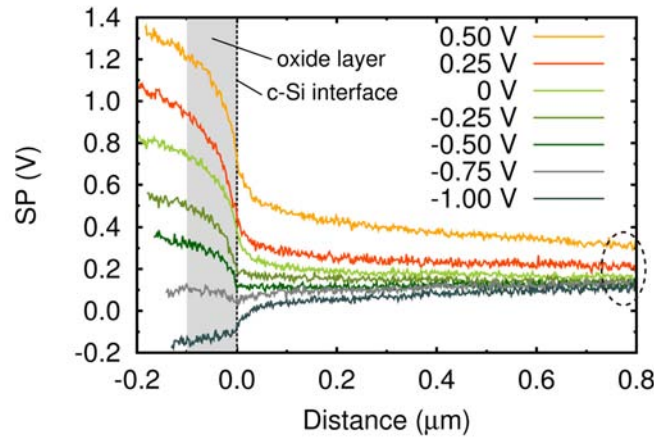


**Figure 4.7:** SP profiles of the MOS structure at different applied bias to the Al gate (left part of the oxide layer). As it can be observed, the differences of the Al gate surface potential are roughly the same than the differences of the applied bias.

plot of Figure 4.7 increases as a result of the enlargement of the downward Si band bending. Conversely, when negative potentials are applied to the Al contact (i.e. gate Fermi level goes up) the SP bending decreases progressively until the flat band situation takes place around a bias of -0.5 V. From this point on, if we apply more negative potentials, the SP bending reverses and bends downwards (i.e. Si band bending bends upwards). This means that the accumulation situation of the MOS structure is achieved. It is important to remark that the observed flat band voltage ( $V_{fb}$ ) is not in agreement with the ideal  $V_{fb}$  (without considering charges at the oxide layer nor at the semiconductor/dielectric interface), which should take place at a bias of about -0.8 V. The observed shift of around 0.3 V between the theoretical and the measured  $V_{fb}$  is linked to the charge correlated to the oxide layer. In fact, when the flat band situation is observed at -0.5 V, the SP curve across the SiO<sub>2</sub> layer (gray colored area) evidences a remaining potential of roughly 0.3 V. The potential drop observed across the oxide layer flats when the theoretical  $V_{fb}$  is applied, i.e. -0.8 V. We can observe two further observations that demonstrate the consistency of these measurements. The first one is that the SP potential of the Al gate changes in the same proportion than the applied external bias. The second one is that the SP signal across the SiO<sub>2</sub> layer draws an exponential-like decay, corresponding to the potential drop through the dielectric layer.

We would like to highlight that the SP profiles show an unexpected be-

#### 4.5. SP under a varying bias

havior. As marked by the dashed circle, the SP curve at the very far region from the MOS interface do not reach the SP value corresponding to the bulk. This observation is specially evident for the 0.5 V curve. We do not have a detailed explanation about this behavior, and despite the results are consistent in general, it is appropriate to be cautious when extracting conclusions.

##### 4.5.1 KPFM spectroscopy

The Al/SiO<sub>2</sub>/Si-based MOS structure has also been studied by means of KPFM spectroscopy measurements. As stated above, KPFM spectroscopy consists on measuring the SP signal variation at certain points of the sample surface as a function of the voltage applied to the Al gate (Si substrate is connected to the ground). Figure 4.8a shows a SP map of an Al/SiO<sub>2</sub>/Si-based MOS cross-section showing the positions where SP vs Bias curves (b) were obtained. In particular, the curves were recorded at a distance of 0.1 (p1), 0.5 (p2) and 1  $\mu$ m (p3) from the SiO<sub>2</sub>/Si interface.

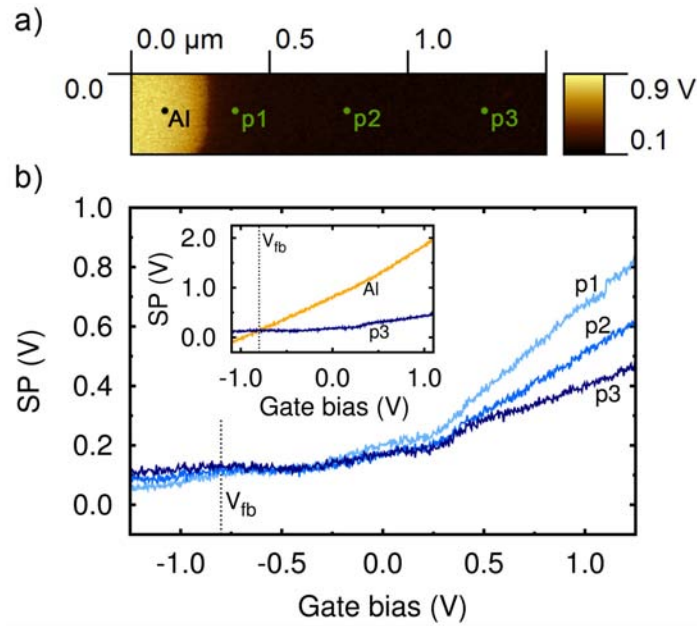


**Figure 4.8:** SP map of an Al/SiO<sub>2</sub>/Si MOS structure (a) that shows the position where the SP vs bias curves (b) were obtained. SP vs bias curves were obtained at a distance of 0.1 (p1), 0.5 (p2) and 1  $\mu$ m (p3) from the SiO<sub>2</sub>/Si interface. The inset shows the SP vs Bias curves obtained at point 3 and at the Al gate. The vertical dashed line labeled as  $V_{fb}$  corresponds to the theoretical position of the flat band voltage.

μm (p3) from the SiO<sub>2</sub>/Si interface. Moreover, the inset depicts a comparison between the SP-Bias curve recorded at point p3 and the one recorded when the tip is positioned onto the Al gate. In both plots the theoretical position of  $V_{fb}$  is depicted by the vertical dashed line. Notice that the latter was calculated for an ideal MOS, i.e. without considering charges associated to the oxide layer.

As it can be seen in the main plot, the closer the point to the MOS interface the larger the SP variation when external bias is applied to the Al contact. Since the points located close to the SiO<sub>2</sub>/Si interface have associated a higher band bending, their corresponding SP variation as a result of a certain gate potential change is higher. On the contrary, the farther the points from the SiO<sub>2</sub>/Si interface, the lower the SP variation as a result of changes in the Al gate. A second observation to be mentioned is that all the curves cross at a voltage around -0.5 V. This bias value (in agreement with the one observed in Figure 4.7) corresponds to the  $V_{fb}$  of the MOS structure under study. When the flat band situation is achieved for a certain value of external bias, then no band bending should exist, and therefore, all the points (independently of the distance from the SiO<sub>2</sub>/Si interface) should show the same SP value. As also seen in Figure 4.7, the  $V_{fb}$  deduced from Figure 4.8 shows a shift of approximately 0.3 V in front of the theoretical  $V_{fb}$  of an ideal MOS (vertical dashed line labeled as  $V_{fb}$ ). We correlate this shift to the charges associated to the oxide layer (and/or semiconductor/oxide interface). In fact, as evidenced by the inset of Figure 4.8, the SP-Bias curves of Al and the one related to the further point from the interface (p3) (being the later roughly associated to the c-Si bulk and therefore without effect of the oxide layer charging effects), cross at the theoretical  $V_{fb}$  represented by the vertical dashed line. The change of  $V_{fb}$  induced by the existence of charge in the oxide layer is described by the following expression:

$$V_{fb} = V_{fb0} - \frac{Q_{ox}}{C_{ox}} \quad (4.5)$$

where  $V_{fb0}$  is the flat band voltage without the effect of the oxide charge,  $Q_{ox}$  is the oxide charge and  $C_{ox}$  is the oxide capacitance. Since  $V_{fb0}$  is -0.8 V and  $V_{fb}$  is observed at -0.5 V, the charges at the oxide layer must be negative. In SiO<sub>2</sub> layers the existence of mobile charges induced by the presence of ions is relatively common. However, these mobile charges are usually positive. Thus, we believe that the observation of a net negative charge at the SiO<sub>2</sub> layer should be correlated to the presence of fixed charges or acceptor states at the SiO<sub>2</sub>/Si interface [88]. The presence of acceptor surface states could be induced by the cleavage of the Si sample.



## 4.6. Chapter summary

---

Theoretically, SP vs Bias curves should reduce their slope at higher positive applied potentials as a result of the band bending reduction that takes place due to the proximity of the inversion regime of the MOS capacitor. In particular, the theoretical threshold voltage ( $V_{th}$ ) of the MOS system under study is calculated to be around 1.1 V. Hence, above this voltage value, the band bending at the oxide/semiconductor should not increase any more. Nevertheless, we observe that the slope of SP vs Bias curves continues increasing above threshold voltage. Despite we do not have a consistent explanation of this behavior, the imperfect cleavage of the MOS stack, and the subsequent possible presence of current leakage across the oxide layer, could be a possible reason of this unexpected observation. Finally, another feature to remark is that the slope of SP vs Bias curves is not constant. In particular, curves show an inflection point around 0.25 V. In this case, the presence of interface states (perhaps induced by the sample cleavage) could be a possible cause of this phenomenon.

## 4.6 Chapter summary

In this chapter, we have investigated the applicability of KPFM for characterizing MOS cross-sections. On the one hand, SP maps recorded by conventional single-pass KPFM measurements have been successfully used to identify the band bending at the semiconductor interface. On the other hand, by voltage-dependent KPFM measurements, other MOS features such as the flat band voltage and the amount of oxide charges have been also characterized.

The obtained results have demonstrated the potential and applicability of this methodology to study MOS structures. However, the results show specific unexpected features, i.e. the non-saturation of SP signal above threshold voltage, we do not understand at this moment. Due to such specific features have been observed while applying an external bias, the possible imperfect cleavage of the MOS structure could be a possible reason. Despite the results are consistent in general, it is appropriate to be cautious when extracting conclusions.



# 5

## Low-temperature micro-PL in $\text{Al}_2\text{O}_3$ -passivated c-Si wafers

*In this chapter, we present a low-temperature micro-Photoluminescence (PL) spectroscopy study of  $\text{Al}_2\text{O}_3$ -passivated c-Si wafers. Surprisingly, low-temperature PL spectra exhibit clear signature of the formation of the so-called Electron-Hole Liquid (EHL) in spite of using low excitation intensities for which the EHL is not usually observed in bulk Si. Besides of its mere but important observation, we have found an interesting correlation between the EHL emission intensity and the passivation efficiency of  $\text{Al}_2\text{O}_3$  layers annealed at different temperatures. We show that the EHL emission intensity variation is correlated to the changes induced by annealing in the  $\text{Al}_2\text{O}_3$ /c-Si interface.*

## 5.1 Introduction

With decreasing temperature, both thermal ionization of impurity-bounded carriers and thermal dissociation of excitons is progressively suppressed (see Section 3.1.3). This leads to a qualitative change in the Photoluminescence (PL) spectra where band-to-band transitions become more improbable and novel PL emission lines involving trapped charges and excitons set in.

In highly excited semiconductors, as it is typically the case in micro-PL measurements (see Section 3.1.2), low temperatures can also favor the formation of a condensed phase of electron-hole pairs, the so-called Electron-Hole Liquid (EHL) [89]. Thus, optical transitions from such a condensate phase may be observable. In the next section, we explain the main features of the EHL concept and the requirements for its formation.

### 5.1.1 Electron-Hole Liquid (EHL)

In a semiconductor material under optical excitation, electron-hole pairs, i.e. excitons, are generated. The number of such photo-generated electron-hole pairs increases steadily with increasing optical pumping. Under this scenario, provided the number of electron-hole pairs is beyond a critical value, they can start to aggregate, leading the formation of a condensed phase of excitons, the so-called EHL [89, 90]. The EHL phase formation is triggered by many-body effects, and only takes place below a critical value of temperature. Figure 5.1a illustrates the phase diagram of exciton systems in c-Si. As it can be seen, the critical density and the critical temperature for the EHL formation are  $3 \times 10^{18} \text{ cm}^{-3}$  and 25 K, respectively. Figure 5.1b represents the formation process of EHL in a highly illuminated crystal.

EHL condensation was first predicted by L.V. Keldysh in 1968 [91]. The discovery leads to a large number of works during the next two decades in which general properties of this metallic degenerate Fermi liquid were studied [92, 93, 94], mostly in Si and Ge. For such bulk semiconductors materials, the carrier lifetimes are so short that in conventional (macro) PL measurements the critical density for the condensation could only be observed under strong (pulsed) optical pumping [95, 96, 97]. A reintroduction of the EHL concept took place at the end of the '90s, this time promoted by the charge carrier confinement in different micro- and nano-structures such as Silicon-On-Insulator (SOI) layers [98], trenched structures [99], nanowires [100, 101] or quantum wells [102]. In this case, since the limited diffusion of e-h pairs favors to reach

## 5.1. Introduction

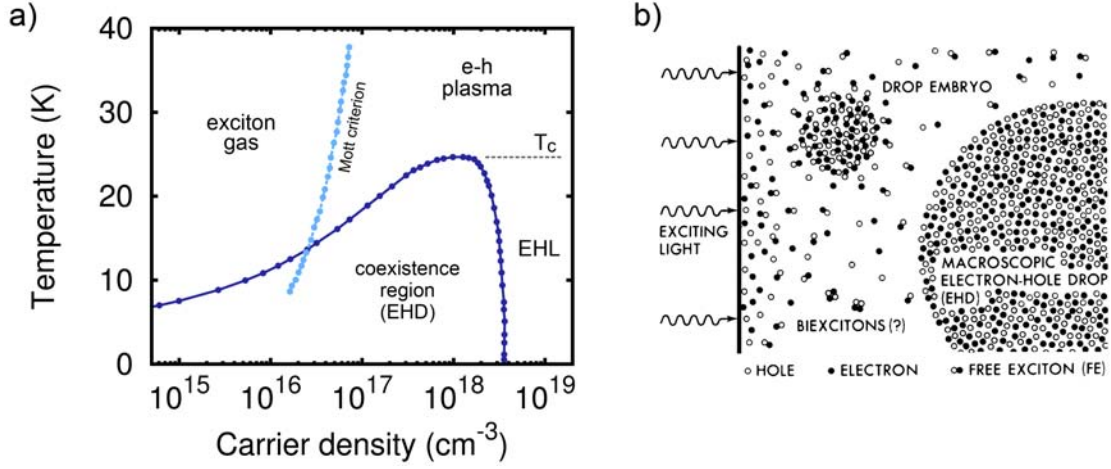


**Figure 5.1:** Phase diagram of exciton systems in c-Si (a) [103] and sketch representing the formation of EHL droplets under the illuminated crystal surface (b) [89]. When the exciton density reaches a critical value, excitons start to aggregate creating EHL droplets, also known as electron-hole droplets (EHD).

the EHL critical density, the condensed phase could be observed even using relatively low excitation powers (e.g. 1-5 mW).

In this chapter, we present a low-temperature PL spectroscopy study of Al<sub>2</sub>O<sub>3</sub>-passivated c-Si wafers, where the passivation efficiency of the alumina layer was varied by the use of different annealing temperatures. Taking into consideration the EHL concept, and in analogy to Figure 3.7 (see Section 3.1.3), we schematically illustrate in Figure 5.2 the different PL transitions that are believed to take place in low-temperature micro-PL studies in c-Si.



**Figure 5.2:** Scheme showing the different entities that participate in the PL recombination as a function of temperature.

**Table 5.1:** List of the sample parameters, including the corresponding fixed charge at the Al<sub>2</sub>O<sub>3</sub> layer and the charge carrier lifetime obtained by C-V and QSSPC measurements, respectively.

Resistivity ( $\Omega\text{cm}$ )	Annealing ( $^{\circ}\text{C}$ )	Charge ( $\text{cm}^{-2}$ )	Lifetime ( $\mu\text{s}$ )
0.4	–	$-1.80 \times 10^{12}$	73
0.4	325	$-2.05 \times 10^{12}$	504
0.4	375	$-2.35 \times 10^{12}$	662
0.4	425	$-3.20 \times 10^{12}$	146
2.5	–	$-1.65 \times 10^{12}$	303
2.5	325	–	1130
2.5	375	$-2.65 \times 10^{12}$	1740
2.5	425	$-3.05 \times 10^{12}$	1180

## 5.2 Experimental methodology

### 5.2.1 Materials and samples

Samples were made from both 0.4 and 2.5  $\Omega\text{cm}$  boron-doped Float-Zone (FZ) crystalline silicon wafers with (100) crystal orientation and thickness of 250  $\mu\text{m}$ . Both sides of the c-Si wafers were passivated by a 25 nm-thick layer of aluminum oxide (Al<sub>2</sub>O<sub>3</sub>), which was deposited by thermal Atomic Layer Deposition (ALD) at 200  $^{\circ}\text{C}$ . In order to have samples showing different passivation efficiencies, the resulting Al<sub>2</sub>O<sub>3</sub>-passivated Si wafers were annealed in forming gas (N<sub>2</sub>/H<sub>2</sub>) at temperatures of 325, 375 and 425  $^{\circ}\text{C}$  for 20 min. Table 5.1 provides the main specifications of the eight samples under study. The level of annealing-induced fixed charge ( $Q_f$ ) in the Al<sub>2</sub>O<sub>3</sub> layer and the resulting effective lifetime ( $\tau_{\text{eff}}$ ) are included. The former was calculated from Capacitance-Voltage (C-V) measurements, where an Al contact was deposited onto the mentioned Al<sub>2</sub>O<sub>3</sub>-passivated samples to form the required Metal-Oxide-Semiconductor (MOS)-Al/Al<sub>2</sub>O<sub>3</sub>/Si structure (see Section 3.4.2). The latter was determined by Quasi-Steady State Photo-Conductance (QSSPC) measurements at a injection level of  $1 \times 10^{15} \text{ cm}^{-3}$  (see Section 3.4.1).

The evolution of both the fixed charge  $Q_f$  and effective lifetime  $\tau_{\text{eff}}$  with annealing temperature for the four 0.4  $\Omega\text{cm}$  c-Si wafers under study is depicted in Figure 5.3. Notice from Table 5.1 data that  $Q_f$  and  $\tau_{\text{eff}}$  for the 2.5  $\Omega\text{cm}$  c-Si wafers follow the same trend. The only difference is that  $\tau_{\text{eff}}$  for the 2.5

## 5.2. Experimental methodology

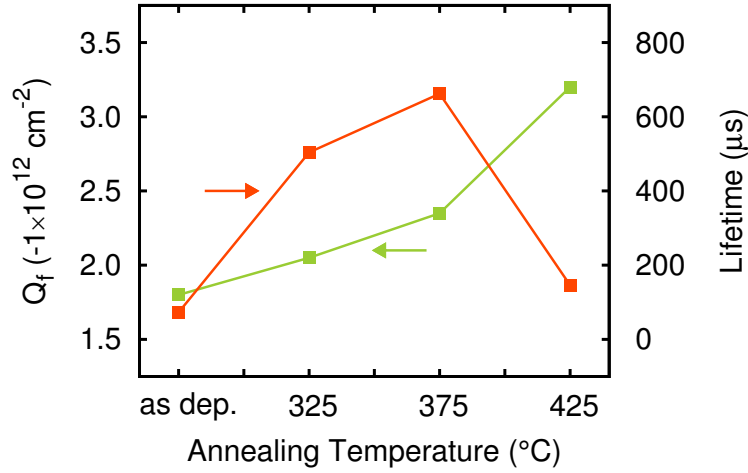


**Figure 5.3:** Fixed charge at the  $\text{Al}_2\text{O}_3$  layer and effective lifetime against annealing temperature of  $\text{Al}_2\text{O}_3$ -passivated  $0.4 \text{ } \Omega\text{cm}$  c-Si wafers annealed in forming gas ( $\text{N}_2/\text{H}_2$ ).

$\Omega\text{cm}$  c-Si wafers is systematically higher due to the lower recombination rate resulting from a lower impurity concentration. As deduced from Figure 5.3, and supported by previous reports [21, 28], the effective lifetime increase that takes place up to an annealing temperature of  $375^\circ\text{C}$  is mainly induced by an increment of the fixed charge at the alumina layer (enhancement of field-effect passivation). However, despite the fact that the fixed charge at the alumina layer further increases for the highest annealing temperature of  $425^\circ\text{C}$ , the harsh heat treatment degrades the  $\text{Al}_2\text{O}_3/\text{c-Si}$  interface (i.e. decrease of chemical passivation), and the charge carrier lifetime decreases again. It is worth to mention that for a better and easier understanding of the results and conclusions presented in this chapter, it is important to keep in mind the evolution of  $Q_f$  and  $\tau_{\text{eff}}$  shown in Figure 5.3, and the conclusions extracted from it concerning the  $\text{Al}_2\text{O}_3/\text{c-Si}$  interface.

### 5.2.2 Measurement details

Low-temperature PL spectroscopy measurements were carried out with a Lab Ram HR Raman spectrometer (Horiba Jobin Yvon). A diode-pumped solid state laser with a wavelength of  $785 \text{ nm}$  was used as excitation source and the light beam was modulated by an optical chopper at a frequency of  $130 \text{ Hz}$ . Due to the low modulation frequency, steady state conditions were ensured.

The PL signal was recorded by a single-channel, infrared photodiode detector using phase-sensitive lock-in amplification. PL measurements were carried out in micro-setup configuration by focusing the laser beam onto the sample surface by microscopic objectives. Two levels of incoming photon flux ( $\Phi$ ) on the sample surface of  $4.5 \times 10^{22}$  and  $2.4 \times 10^{20}$  photons $\cdot$ s<sup>-1</sup> $\cdot$ cm<sup>-2</sup> were used. These photon fluxes resulted from an excitation power of 5.7 and 8.5 mW and a spot diameter of 8 and 133  $\mu$ m, respectively.

### 5.2.3 Cooling procedure

Low-temperature PL experiments were performed using a gas flow-type cryostat where the sample to be studied is located. The laser beam enters through an optical quartz window (1 mm thickness) located at the top side of the cryostat. During measurement the samples are under High Vacuum (HV)-conditions. These are obtained by a vacuum pump unit consisting of a turbomolecular pump coupled to a rotary vane pump. For performing measurements at low temperatures the cryostat was cooled down using liquid He (see Figure 5.4). The gas flow of liquid-He passes throughout the cooling circuit in

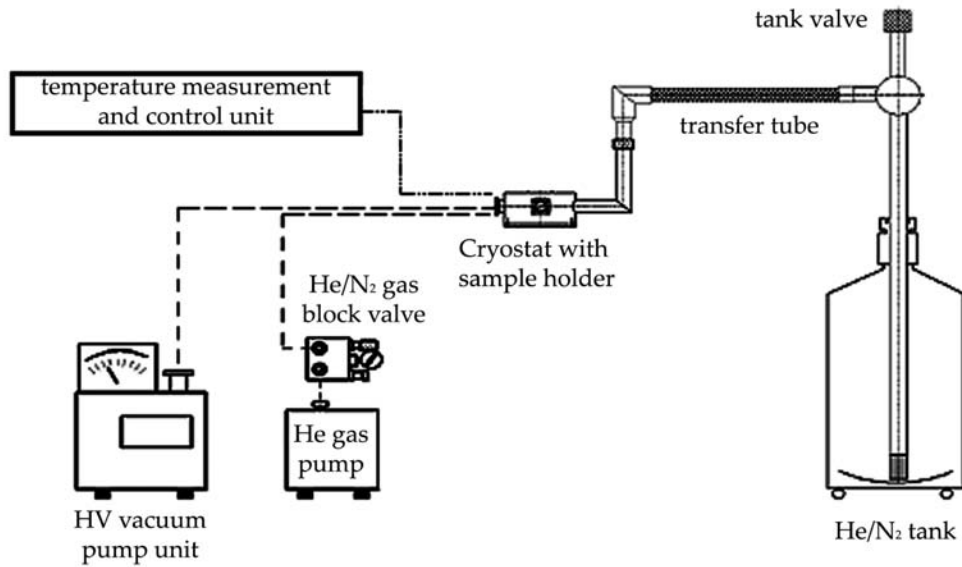


**Figure 5.4:** Setup for cooling. The liquid He leaves the tank and passes through the cryostat where it is evaporated. Both the tank valve and a gas pump at the end of the circuit control the He gas flux.



order to cool the sample chamber down to the desired temperature. The flux of the cooling liquid can be regulated by the tank valve, while the evaporation pressure is controlled by a gas pump located at the end of the circuit. A temperature control unit with an installed heater linked to a temperature sensor in the cryostat is used to regulate the cooling-down and heating-up process of the samples. The temperature range goes from 3.5 K to 325 K, and its temperature stability is within 0.1 K.

## 5.3 PL down to 40 K

Figure 5.5 illustrates the PL spectra recorded at temperatures from 300 to 40 K for a 0.4  $\Omega\text{cm}$  c-Si wafer passivated by a 25 nm-thick layer of  $\text{Al}_2\text{O}_3$  annealed at 375 °C. PL spectrum obtained at room temperature ( $\sim 300$  K) reveals a wide PL emission centered around 1.1 eV. This PL emission line is correlated to the (indirect) transverse-optical (TO) phonon-assisted band-to-band transitions. With decreasing temperature, energy of phonons decreases. Then, the phononic energy contribution to the phonon-electron scattering process in band-to-band transition become less important. This phenomenon is evident in the PL spectra recorded between 300 and 80 K as a significant and progressive narrowing of the PL emission band, the lower the temperature. Additionally, we also observe a progressive PL intensity enhancement with decreasing temperature, which is related to decrease of the non-radiative recombination due to a reduction of the phonon population [104]. We can observe two further phenomena induced by the decrease of temperature. One is the observation in the PL spectrum recorded at 180 K of the PL emission from Free-Bound (FB) transitions involving carriers chained to boron impurities. Moreover, below  $\sim 80$  K, thermal energy  $k_B T$  is lower than the exciton binding energy and thermal dissociation of excitons is progressively suppressed. Due to this fact, recombination from both TO-phonon assisted (indirect) Free Exciton (FE) and Bound Excitons (BE) starts to take place. The PL emission from BE recombination is observed in the PL spectra by a small shoulder on the left side of the FE PL emission line. Since the complex has an extra binding energy due to the exciton-impurity interaction, the BE has associated a slightly lower emission energy.

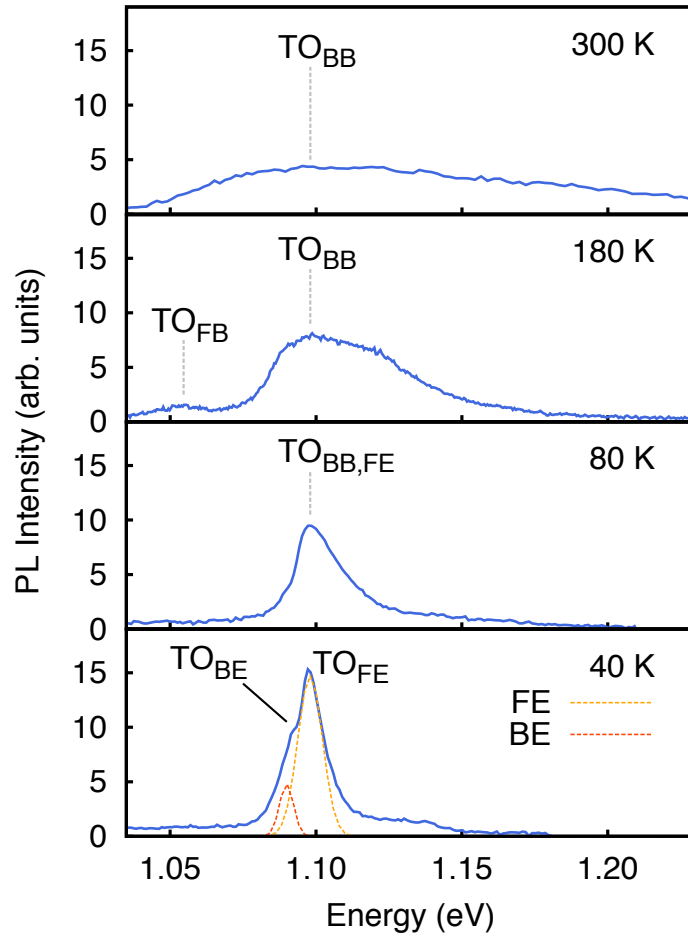


**Figure 5.5:** PL spectra between 300 and 40 K of a 2.5  $\Omega\text{cm}$  c-Si wafer passivated with a 25 nm-thick layer of Al<sub>2</sub>O<sub>3</sub> annealed at 375 °C. Spectra were recorded with a photon flux of  $4.5 \times 10^{22} \text{ photons} \cdot \text{s}^{-1} \cdot \text{cm}^{-2}$ . Peak assignment to TO-phonon assisted band-to-band (TO<sub>BB</sub>) recombination, free-bound (TO<sub>FB</sub>) recombination, free excitons (TO<sub>FE</sub>) recombination and bound excitons (TO<sub>BE</sub>) recombination is indicated.

## 5.4 PL below 40 K

Figure 5.6 shows representative PL spectra recorded at temperatures from 40 to 4 K for both a 0.4 and a 2.5  $\Omega\text{cm}$  c-Si wafers passivated by a 25 nm-thick layer of Al<sub>2</sub>O<sub>3</sub> annealed at 375 °C. At 40 K the PL spectra are characterized by an emission line at 1.098 eV and a low energy shoulder, which are related to the indirect TO phonon-assisted transition of FE and BE, respectively. The excitonic emission dominates the PL spectra down to about 25 K, where the

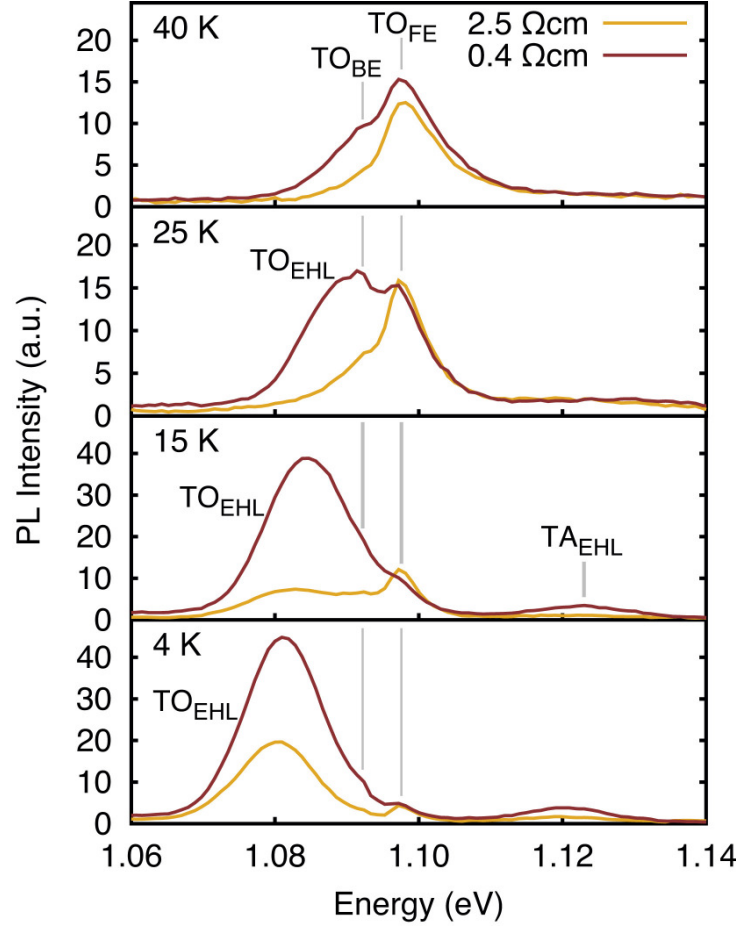


**Figure 5.6:** PL spectra between 40 K and 4 K of a 0.4 and 2.5  $\Omega\text{cm}$  c-Si substrates passivated with a 25 nm-thick layer of  $\text{Al}_2\text{O}_3$  annealed at 375  $^\circ\text{C}$ . The spectra were recorded with a photon flux of  $4.5 \times 10^{22} \text{ photons} \cdot \text{s}^{-1} \cdot \text{cm}^{-2}$ . Peak assignment to TO-phonon assisted recombination of free excitons (FE), bound excitons (BE) and Electron-Hole-Liquid (EHL) is indicated.

appearance of an additional PL band at ( $\sim 1.088$  eV) sets in. This broader band increases gradually in intensity, becoming the most prominent feature below 15 K. In addition, the observed increase in intensity is also accompanied by a significant redshift with decreasing temperature. We emphasize that such a marked temperature behavior cannot be ascribed to a stiffening of the optical phonon involved in the indirect transition, since below 80 K both FE and BE excitonic transitions occur essentially at the same energy. The observed variation with temperature of the peak energy and intensity is clear signature of the influence on the optical transition of many-body effects which are strongly

temperature dependent. As mentioned above, at such low temperatures, provided that the lifetimes of the photo-generated carriers (electrons as well as holes) are long enough, it is possible to build up carrier densities beyond the critical value at which many-body effects arising from exchange and correlation interactions would trigger the formation of droplets of the condensed EHL phase [105]. The droplets grow at expenses of free and bound excitons as well as band electrons and holes. Since the exchange terms of the Coulomb interaction yield a negative nonlinear contribution to the total energy of the electronic system, there is a pronounced bandgap renormalization (reduction) associated with the formation of the condensate. This renormalization manifests itself in a reduction of the optical transition energy, as observed, for example, in doped GaAs single quantum wells [106]. The higher the carrier density, the stronger the reduction. With decreasing temperature we expect an increase in the photo-generated carrier density mainly due to the enhancement of the carrier lifetime. For all these reasons and supported by previous results [89], we assign the broad PL feature to TO phonon-assisted radiative recombination processes from a condensed EHL. Incidentally, emission from the Transverse-Acoustical (TA) phonon-assisted EHL recombination is also detected at 1.12 eV.

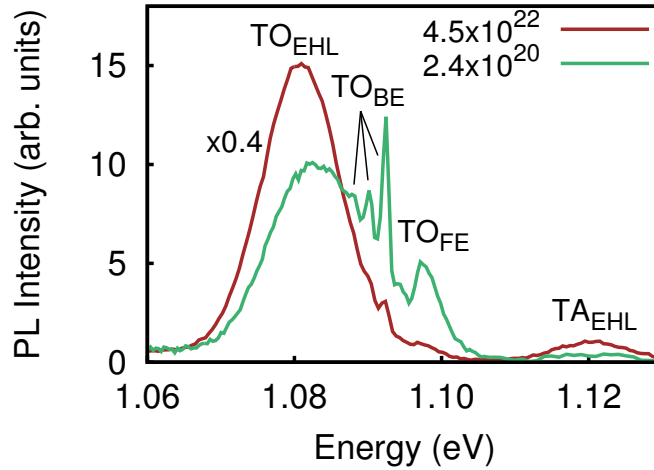


**Figure 5.7:** PL spectra of the  $\text{Al}_2\text{O}_3$ -passivated 0.4  $\Omega\text{cm}$  c-Si wafer recorded at 8 K using a photon flux of  $4.5 \times 10^{22}$  and  $2.4 \times 10^{20}$   $\text{photons} \cdot \text{s}^{-1} \cdot \text{cm}^{-2}$ . Note that the PL spectrum recorded with the higher photon flux is depicted with a scaling factor of 0.4.

#### 5.4. PL below 40 K

---

For a given incident photon flux per unit time  $\Phi$ , every absorbed photon within a distance  $d$  from the Si surface, determined by the absorption coefficient of Si at low temperature for the given laser wavelength ( $\alpha = 550 \text{ cm}^{-1}$ ) [107], would generate an electron-hole (e-h) pair. In order for the condensed phase to form, the effective concentration of photo-generated e-h pairs has to reach the EHL critical density ( $\rho_c = 3 \times 10^{18} \text{ cm}^{-3}$ ) [108], which can be roughly estimated according to:

$$\rho_c = \frac{\Phi \tau_{\text{exc}}}{d} \left( 1 - e^{-\alpha d} \right), \quad (5.1)$$

where  $\tau_{\text{exc}}$  corresponds to the average lifetime of photo-generated e-h pairs. Two important deductions can be extracted from Equation (5.1). First, we can observe that the stability of the EHL phase mainly depends on both the lifetime (intrinsic to the material) and the incident photon flux. This fact is clearly revealed by Figure 5.7. The panel shows two PL spectra recorded at 8 K in an  $\text{Al}_2\text{O}_3$ -passivated  $0.4 \text{ } \Omega\text{cm}$  c-Si using two different levels of incoming photon flux. As it can be seen, the PL spectrum recorded with the lower photon flux exhibits a significantly less intense EHL feature (either the one assisted by TO phonons as well as the one assisted by TA phonons). This is because for the weaker photon flux, the photo-generated carrier density is close to the critical value and the EHL becomes thermally unstable [109, 110]. In addition, for the higher photon flux it is also observed a higher band-gap renormalization (i.e. lower energy associated to the EHL optical transition). This is because for a higher carrier density the EHL has associated higher Coulomb interaction exchange terms. The second insight about the EHL behavior can be deduced by isolating the distance  $d$  from Equation (5.1):

$$d \simeq \frac{2}{\alpha} \left( 1 - \frac{\rho_c}{\Phi \tau_{\text{exc}} \alpha} \right). \quad (5.2)$$

In this case, Equation (5.2) further tells us that for the distance  $d$  to be positive but non-zero,  $\tau_{\text{exc}}$  should be larger than about 120 ns, which is typically achieved at low temperatures in high-quality, indirect-gap semiconductors, where the carrier lifetime is largely determined by the radiative recombination time.

The variation with temperature of the integrated intensity for both the EHL and the FE emission peaks is depicted in Figure 5.8 for the two c-Si wafers with different resistivity. At temperatures above 30 K, PL emission mainly proceeds from the FE (and BE, of course) recombination, slightly increasing in intensity

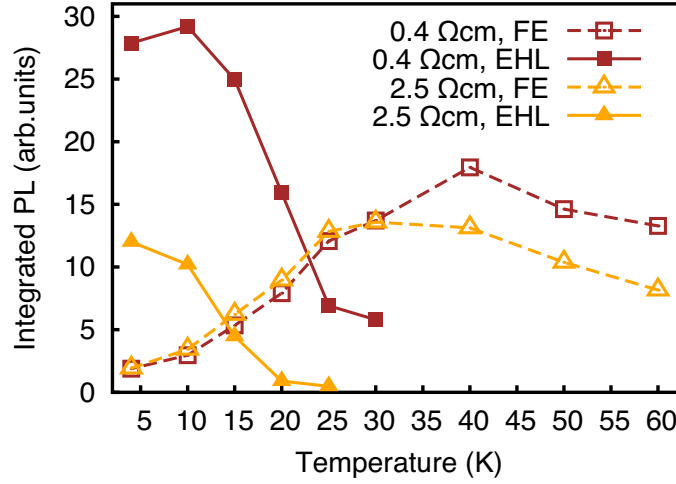


**Figure 5.8:** Integrated PL intensity against temperature of the phonon-assisted FE emission and the EHL emission of the 0.4 and the 2.5 Ωcm c-Si substrates passivated by an Al<sub>2</sub>O<sub>3</sub> layer annealed at 375 °C.

from 60 K to 40 K as a result of the decrease of the non-radiative relaxation rate due to less electron-phonon scattering processes. The intensity of the FE emission, in contrast, begins to fade as soon as the EHL emission sets in. The steep intensity rise of the latter with decreasing temperature in the range of coexistence is a clear indication that both are mutually competing radiative recombination mechanisms. Below 20 K, the EHL recombination increasingly becomes the dominant process in detriment of any excitonic emission, since the condensate is the lowest excited state. It is also worth to mention that the 0.4 Ωcm substrate shows a significantly higher intensity of the EHL emission than the 2.5 Ωcm substrate. This effect is related to the different doping levels of the samples, since the (substitutional) doping impurities act as nucleation centers for the condensation of the EHL. The formation of an EHL droplet is more likely to proceed from excitons bound to the doping impurities due to their extra binding energy (BE transition). Hence, the EHL is thermodynamically more stable in the wafer with higher residual doping.

#### 5.4.1 Correlation between EHL PL intensity and passivation efficiency

Figure 5.9 shows the EHL emission intensity of the two sets of samples with different resistivity as a function of the annealing temperature of the Al<sub>2</sub>O<sub>3</sub>

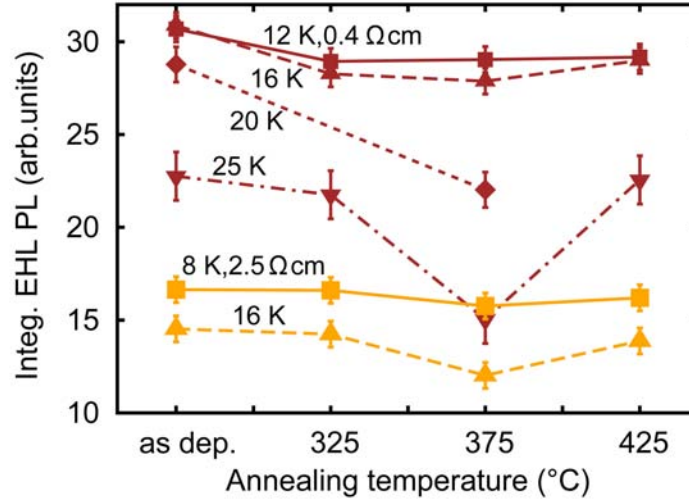


**Figure 5.9:** Variation of the integrated EHL emission intensity between 8 and 25 K as a function of the annealing temperature of the alumina layer for both the 0.4 and the 2.5  $\Omega\text{cm}$  c-Si substrates.

layer. For clarity, we show data only for selected temperatures between 8 and 25 K. Both sets of samples exhibit the same general behavior. Up to an annealing temperature of 375 °C, the EHL emission intensity shows a decreasing trend, whereas for the highest annealing temperature of 425 °C the trend is reversed (EHL intensity increases). As it can be seen, the observed variation is more marked the higher the temperature. Interestingly, the EHL intensity evolution with annealing temperature is the opposite to that of the photoconductivity carrier lifetime (see Table 5.1 and Figure 5.3).

We attempt to explain this striking result with the help of the sketches in Figure 5.10, which illustrate the expected band profile close to the surface under steady-state illumination. As the effect of annealing consists in a variation of the charge balance between the Si surface charge and the one thermally created at the thin alumina layer, the extension  $D$  of the hole accumulation region at the Si sub-surface region would also change in the same proportion. Since photo-generated e-h pairs dissociate immediately in the band-bending region, thus, impairing any radiative recombination, the EHL emission can only stem from a sub-surface region delimited by the depth  $d$  of e-h pair photo-generation (see Equation 5.1) minus the extension  $D$  of the band-bending region.

For annealing temperatures up to 375 °C, the induced increase of the fixed

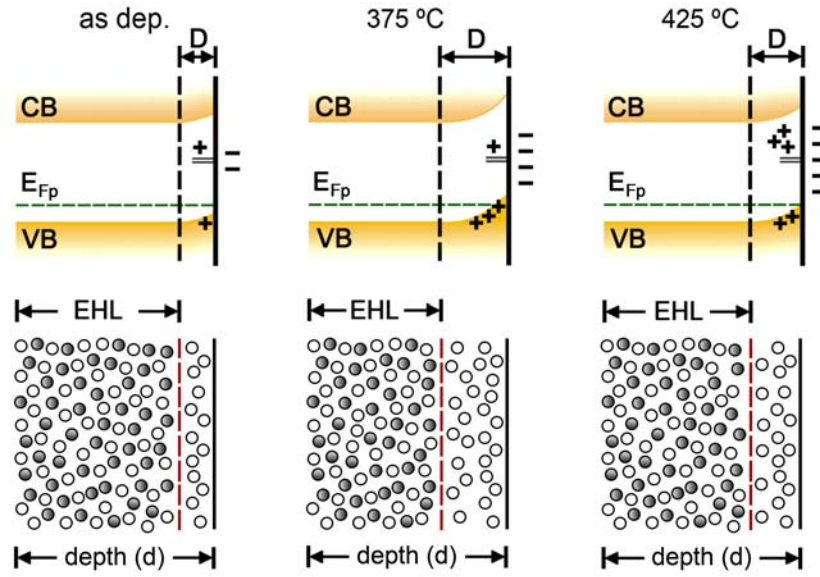


**Figure 5.10:** Sketches illustrating the band profile under steady-state illumination and the variation of the accumulation region of photo-generated holes ( $D$ ) induced by changes in the net interface charge with annealing.  $E_{Fp}$  denotes the quasi-Fermi level of holes. Quasi-Fermi level of electrons is omitted for the sake of clarity.

charge in the alumina leads to a more pronounced surface accumulation region (larger band bending) and thus to a larger  $D$ . This, in turn, leads to a reduction of the active EHL radiative recombination volume given by  $d - D$ , and therefore, the EHL emission intensity diminishes. However, for the highest annealing temperature of 425 °C, despite the further increase in the fixed negative charge at the alumina layer, degradation of the  $\text{Al}_2\text{O}_3/\text{Si}$  interface starts to occur, as suggested by the decrease of the QSSPC carrier lifetime (see Table 5.1 and Figure 5.3). By interface degradation is meant the generation of surface defect states at elevated annealing temperatures, which partially counteract the negative charges at  $\text{Al}_2\text{O}_3$ , reducing  $D$ . Hence, the active EHL recombination region as well as the EHL emission intensity increase again for the highest annealing temperature.

To strengthen the proposed hypothesis, it is instructive to take a closer look at Equation (5.2) and its implications. At very low temperatures ( $T < 15$  K), exciton lifetimes ( $\tau_{\text{exc}}$ ) of about 200 ns [103] lead to a large depth  $d$  of roughly 14  $\mu\text{m}$ . This value of  $d$  is too large compared to a band-bending extension  $D$



#### 5.4. PL below 40 K

in the order of 100 nm, therefore, little influence of the charge accumulation region is expected. In contrast,  $\tau_{\text{exc}}$  decreases with increasing temperature and can reach values close to the EHL critical lifetime of 120 ns at temperatures around 25 K [103]. For this case, Equation (5.1) yields rough estimates of  $d$  below 1  $\mu\text{m}$ , which are now of the same order of  $D$ . These simple facts explain well the data points depicted in Figure 5.9.

For a better clarity and understanding of this behavior, the evolution of the EHL PL intensity as a function of temperature is represented in Figure 5.11 for both the as deposited sample and the one annealed at 375 °C. For both samples, the measured integrated PL intensity of the EHL emission is systematically lower, the higher the temperature. This is interpreted as a reduction of  $d$  (and  $d - D$ , of course) with increasing temperature. Since  $D$  is larger for the sample annealed at 375 °C than for the as-deposited one, the reduction of the EHL PL intensity with increasing temperature, is proportionally higher for the annealed sample. This is observed as a higher slope for the annealed sample curve. This fact brings us to the conclusion that the sensitivity of the EHL PL intensity to variations of  $D$  increases with increasing temperature.

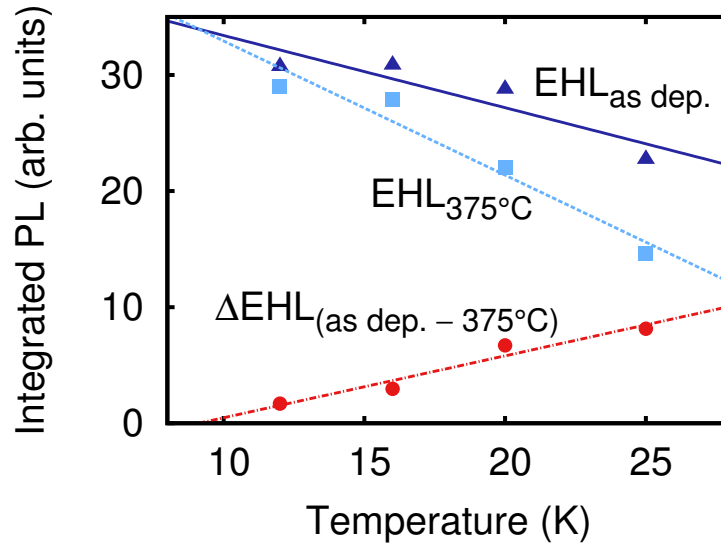


**Figure 5.11:** Variation of the integrated EHL PL against temperature for the as-deposited  $\text{Al}_2\text{O}_3$ -passivated c-Si wafer and the one annealed at 375 °C. Additionally, the difference between both PL signals ( $\Delta\text{EHL}$ ) is also shown.

### 5.4.1.1 Al<sub>2</sub>O<sub>3</sub> charge density under illumination

It is worth to mention that the charge density of Al<sub>2</sub>O<sub>3</sub> has been reported to suffer changes under certain optical excitation conditions. Recently, Liao *et al.* [111] reported an increase of Al<sub>2</sub>O<sub>3</sub> negative fixed charge due to light soaking from 1-sun illumination. Moreover, Gielis *et al.* [112] observed multiple photon induced charge trapping when studying the charging dynamics of Al<sub>2</sub>O<sub>3</sub> by Second-Harmonic Generation (SHG) measurements. In any case, as suggested by the band diagram of Si/Al<sub>2</sub>O<sub>3</sub> illustrated in Figure 5.12, excitation conditions should provide photons with an energy of at least 3.12 eV in order to promote electrons from the Si valence band up to the Al<sub>2</sub>O<sub>3</sub> conduction band. Notice that the representation of an interfacial SiO<sub>x</sub> layer between Si and Al<sub>2</sub>O<sub>3</sub> is simply due to the fact that some authors have reported its existence in c-Si wafers passivated by ALD Al<sub>2</sub>O<sub>3</sub> [28]. In the work of Liao *et al.*, the 3.12 eV barrier could be exceeded by photons from the UV part of the solar spectrum, whereas in the work of Gielis *et al.*, the process could be completed by multi photon mechanisms as a result of the high-level non-linear excitation. It is important to remark that under our Continuous Wave (CW) 1.58 eV excitation, we have no experimental evidence of such charging effects. In fact, all measured PL lines were stable in time and reproducible in terms of their intensity, even upon changes in temperature.

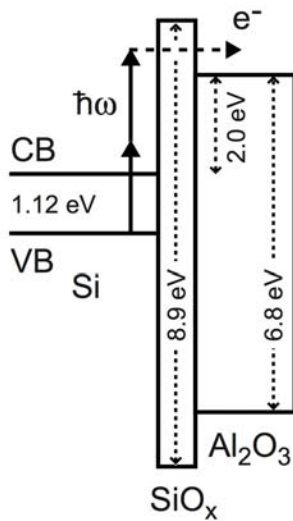


**Figure 5.12:** Band diagram of an Al<sub>2</sub>O<sub>3</sub>/c-Si interface illustrating the hypothetical photon induced charge injection into Al<sub>2</sub>O<sub>3</sub> layer under illumination [112]. Notice that an extra SiO<sub>x</sub> interfacial layer between Si and Al<sub>2</sub>O<sub>3</sub> is considered.

### 5.5 Chapter summary

Two main conclusions can be drawn from the work presented in this Chapter. First, we have shown that the use of micro-PL measurements at low-temperatures can favor the formation of the so-called EHL phase in Si even using moderate excitation powers for which the condensed phase is not usually observed in bulk Si. The elevated focalization linked to micro-PL measurements allows to reach the EHL critical density without the need to use elevated optical pumping. Second, we have shown that the intensity of the EHL emission is correlated to the net electric field at the  $\text{Al}_2\text{O}_3/\text{c-Si}$  interface. This finding opens the possibility to use this approach to monitor local variations in the surface and sub-surface interface properties.



# 6

## High-resolution spatially-resolved characterization of LFCs

*In this chapter, micro-Photoluminescence (PL) and micro-Raman spectroscopy measurements are used to carry out a comprehensive analysis of Laser-Fired Contacts (LFCs). In the first section, we take advantage of the high spatial resolution and the lifetime-sensitivity capabilities of micro-PL measurements in order to characterize the impact of laser processing on the performance of the passivation layer at the regions around the contacts. In the second section, high-resolution spatially-resolved Raman and PL measurements are used to study in detail the inner part of different LFCs processed in  $\text{Al}_2\text{O}_3$ -passivated c-Si wafers. Relevant information about LFC features such as the doping profile and the structural properties of the laser-processed region have been obtained by a detailed study of the recorded PL and Raman spectra.*

## 6.1 Introduction

LFC processes have already been used to create rear base contacts in solar cells with efficiencies well above 20% [51, 45]. Despite the evident success in the implementation of the LFC approach in real devices, there is still a lack of information about specific features of LFCs such as the impact on the passivation layer at the contacts vicinity, the level and doping profile of the p+ region and/or the structural properties of the laser-processed region. The most likely reason for that is the difficulty to find experimental techniques that match a high-lateral resolution (below 10  $\mu\text{m}$ ) and sensitivity to the parameters to be studied. In the present chapter, we use micro-Raman and micro-PL spectroscopies with a lateral resolution down to 1  $\mu\text{m}$  in order to perform a detailed spatially-resolved study of LFCs. The chapter has been divided in two main sections: the study of the induced impact at the LFC vicinity, and the study of the doping profile and the structural properties of the inner part of LFCs.

## 6.2 Local impact at the LFCs surroundings

As described in Section 2.3.1, the formation of LFCs is characterized by a local melting and solidification step of the bulk c-Si [113]. In such a rapid thermal cycle, local temperature can reach values above the silicon melting temperature, i.e. 1414 °C. Hence, the material fraction around the LFC is believed to suffer high thermal gradients during contact formation. This could induce important damage on the passivation capabilities around the contacts, decreasing the effective rear surface passivation in such area.

In this section, we use micro-PL spectroscopy measurements with a spatial resolution of 7  $\mu\text{m}$  in order to study how the laser processing affects the passivation capabilities of dielectric layers deposited onto the c-Si. In particular, we demonstrate that the passivation efficiency decreases at the nearby regions of the laser-processed base contacts. Such a decrease in passivation efficiency is studied in terms of laser power, laser wavelength, and type of dielectric stack system. Both laser processed  $\text{SiC}_x/\text{Al}_2\text{O}_3/\text{c-Si}$  and  $\text{Al}_2\text{O}_3/\text{c-Si}$  samples have been studied. Finally, from the obtained micro-PL information, we have estimated the impact of the laser processing on the passivation efficiency as a function of the pitch of the processed spots.

## 6.2. Local impact at the LFCs surroundings

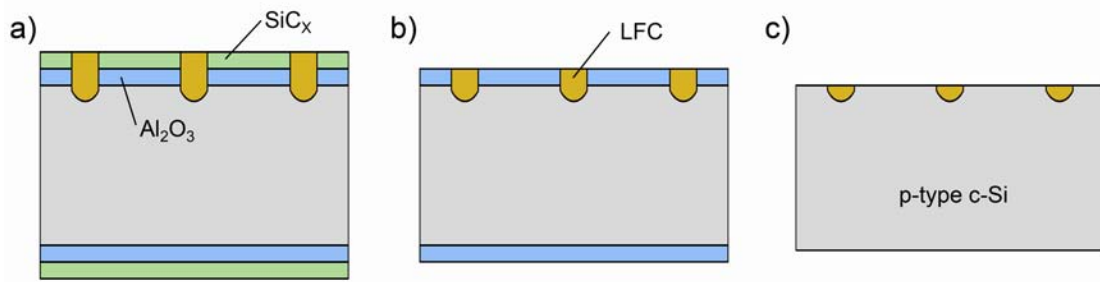


**Figure 6.1:** Sample structures studied in this chapter: laser processed  $\text{SiC}_x/\text{Al}_2\text{O}_3$  stacks (a), laser processed  $\text{Al}_2\text{O}_3/\text{c-Si}$  (b) and laser processed  $\text{Al}_2\text{O}_3/\text{c-Si}$  + immersion in hydrofluoric (HF) acid (c).

### 6.2.1 Experimental details

#### 6.2.1.1 Sample details

As schematically illustrated in Figure 6.1, three different sample structures were used to carry out the present study:

- A: laser processed  $\text{SiC}_x/\text{Al}_2\text{O}_3/\text{c-Si}$  stacks
- B: laser processed  $\text{Al}_2\text{O}_3/\text{c-Si}$  stacks
- C: laser processed  $\text{Al}_2\text{O}_3/\text{c-Si}$  + immersion in hydrofluoric (HF) acid

All the samples were based on p-type 2.5  $\Omega\text{cm}$  (boron-doped) float zone (FZ) crystalline silicon wafers with (100) crystal orientation and thickness of 250  $\mu\text{m}$ . After a RCA <sup>1</sup> cleaning sequence, a 25 nm-thick layer of  $\text{Al}_2\text{O}_3$  was deposited on both wafer sides by thermal Atomic Layer Deposition (ALD) in a Cambridge Nanotech Savannah S200 system at a temperature of 200  $^\circ\text{C}$ . During the process the surface of the substrate was alternatively exposed to trimethylaluminium ( $\text{Al}_2(\text{CH}_3)_6$ ) (TMA) and  $\text{H}_2\text{O}$  as precursors, which reacted until the surface was saturated. The reactions were cyclical and each reaction was purged by means of  $\text{N}_2$  to remove the reactants and the reaction products.

To obtain sample structure A, a 50 nm-thick capping layer of  $\text{SiC}_x$  was subsequently deposited by Plasma Enhanced Chemical Vapor Deposition (PECVD)

<sup>1</sup>The RCA clean is a standard set of wafer cleaning steps performed before high-temperature processing steps of silicon wafers in semiconductor manufacturing. Werner Kern developed the basic procedure in 1965 while working for RCA, the Radio Corporation of America.

**Table 6.1:** Specifications of the two types of laser used to process the LFCs studied in this section.

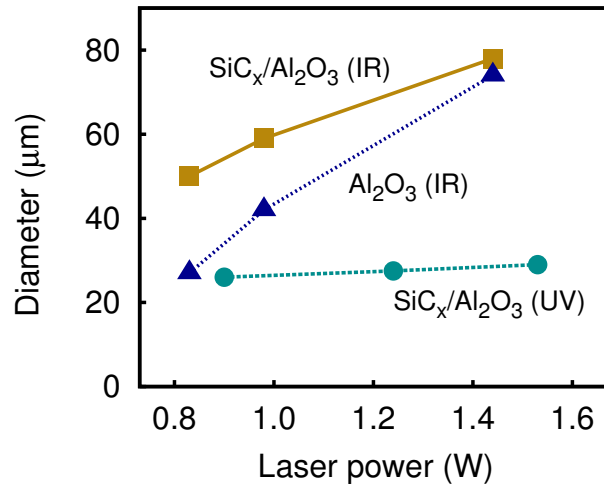
Manufacturer	Type	$\lambda$ (nm)	Pulse (ns)	Freq. (KHz)
StarMark	Nd:YAG	1064	100	4
Spectra-Physics	Nd:YVO <sub>4</sub>	355	12	20

on both sides of the  $\text{Al}_2\text{O}_3/\text{c-Si}/\text{Al}_2\text{O}_3$  stack. Next, a forming gas annealing (375 °C, 15 min in  $\text{H}_2/\text{N}_2$  atmosphere) was applied.

To obtain structure B, an  $\text{Al}_2\text{O}_3/\text{c-Si}/\text{Al}_2\text{O}_3$  sample was directly annealed in forming gas ( $\text{N}_2/\text{H}_2$ ) at a temperature of 375 °C for 15 min.

To obtain sample structure C, sample B was immersed in an HF (Hydrofluoric acid) 1% solution bath. The etching process took around 40 s approximately or until a hydrophobic silicon surface was obtained.

Two types of laser were used to process the LFCs (Table 6.1). In the majority of the samples, LFCs were processed by a 1064 nm Nd:YAG lamp-pumped Solid State Laser (SSL) working at 100 ns and 4 KHz of pulse duration. In this case, LFCs were processed using a laser power of 0.83, 0.98 and 1.43 W. Additionally, in order to study possible differences of using a different laser wavelength to process the contacts, other LFCs were processed by a 355 nm

**Figure 6.2:** Spot diameter against laser power for the different LFCs studied in this work.



## 6.2. Local impact at the LFCs surroundings

---

Nd:YVO<sub>4</sub> diode-pumped SSL working at 12 ns and 20 KHz of pulse duration. Here, LFCs were processed at a laser power of 0.90, 1.24 and 1.53 W.

Figure 6.2 shows the evolution of the contact diameter as a function of the laser power. Spot diameter of Infrared (IR)-processed contacts increases with increasing laser power, whereas spot diameter of Ultraviolet (UV)-processed contacts does not. In addition, spot diameter of UV contacts is significantly lower than diameter of IR LFCs. However, taking into account that power is defined by energy per unit of time, and the laser pulse used to process UV spots is one order of magnitude lower than that used for the IR spots, we have that the amount of energy used to process the UV spots is approximately one order of magnitude lower. In these sense, if we normalize the spot diameter by energy, the diameter of UV spots is proportionally higher. We attribute this fact to the higher absorption coefficient of silicon at the UV part of the electromagnetic spectrum.

### 6.2.1.2 Measurement procedure

Topography maps of LFCs were obtained by optical profilometry using a Micro-Xam 100 profilometer (KLA-Tencor). Micro-PL and micro-Raman spectroscopy measurements were carried out with a Horiba Jobin Yvon LabRam HR Raman spectrometer. For micro-PL measurements a diode-pumped solid state laser with a wavelength of 785 nm was used as excitation source. The light beam was modulated by an optical chopper at a frequency of 130 Hz to amplify the generated PL signal by a Lock-in amplifier. Due to the relatively long lifetime of the photo-generated carriers, the light beam modulation at 130 Hz ensured steady state conditions. The PL signal was recorded by an IR photodiode detector. PL measurements were carried out in a micro-setup configuration where light excitation beam was focused onto the sample surface by a 50x microscope objective (Leica) with a numerical aperture of 0.55. The mentioned configuration resulted in a light spot (and therefore a spatial resolution) of 7  $\mu\text{m}$  of diameter. In the case of micro-Raman measurements light excitation was made by the same diode-pumped solid state laser (wavelength of 785 nm) and again the light beam was focused onto the sample surface by a 50x microscope objective. Here, the inelastic scattering signal was collected by a charge-coupled device (CCD) cooled at 135 K.

### 6.2.2 Impact of the laser pulse on the passivation layer

Figure 6.3 shows both topography (a) and PL (b) maps of a LFC processed at 1.44 W in a  $\text{SiC}_x/\text{Al}_2\text{O}_3$ -passivated c-Si wafer. The physical dimensions of the LFC are represented in the PL map by a dotted circle. The corresponding topography (a) and PL (b) profiles correlated to the green horizontal lines of Figure 6.3 are depicted in Figure 6.4. The topography profile shows the morphology of the contact cross-section and allows the precise identification of the LFC borders (black vertical dashed lines). This has allowed the accurate correlation between both the topography and PL profiles for studying in detail the PL signal associated to the different points of the contact cross-section.

As c-Si is an indirect band gap semiconductor in which non-radiative processes are dominant mechanisms, and taking into account that radiative and

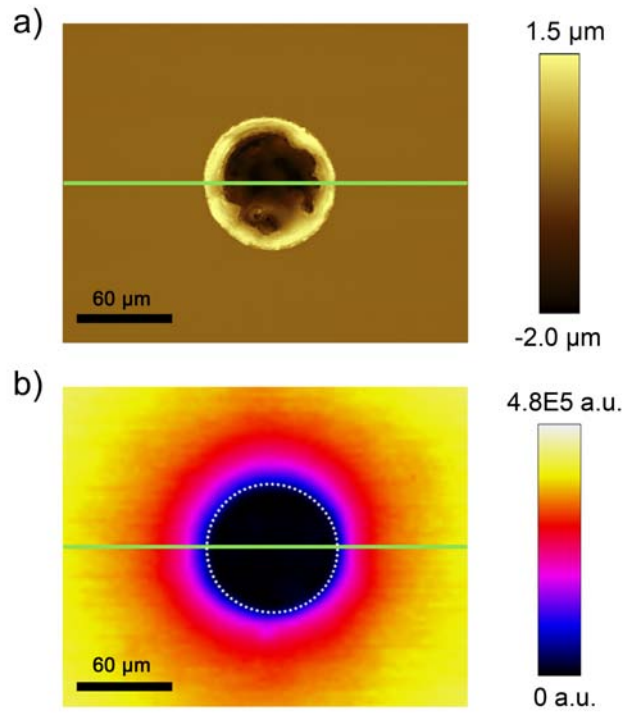


**Figure 6.3:** Optical profilometer topography map (a) and PL map (b) of a LFC processed in a  $\text{SiC}_x/\text{Al}_2\text{O}_3$ -passivated c-Si wafer at 1.44 W. The green line defines the horizontal cross-section from which topography and PL profiles of Figure 6.4 were obtained. In the PL map, the physical dimensions of the LFC are defined by the white dotted circle.

## 6.2. Local impact at the LFCs surroundings

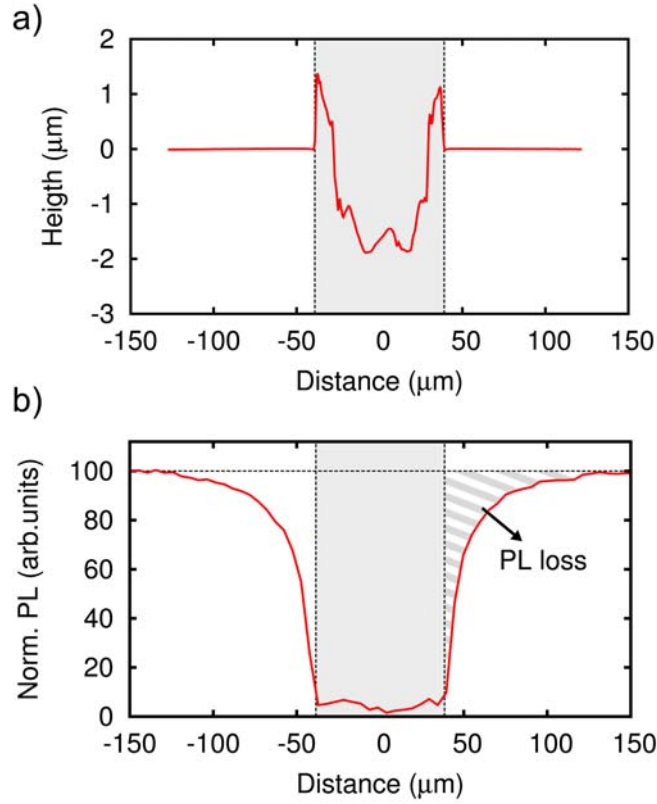


**Figure 6.4:** Topography (a) and PL (b) profiles corresponding to the green lines represented in Figure 6.3. The gray area depicts the inner part of the contact. PL profile is normalized by its maximum value at  $x=-150$  (and  $x=150 \mu\text{m}$ ), which corresponds to surface points non-affected by laser.

non-radiative are competitive processes (see Section 3.1.1.2), a maximum value of PL implies a minimum rate of non-radiative processes [114]. Thus, assuming that bulk recombination is negligible in front of surface recombination processes (as it is the case in our FZ c-Si samples), the higher the PL, the better the performance of the passivation layer [115]. As it can be seen, the PL profile of Figure 6.4 shows a maximum PL value at the further points ( $x = -150$  and  $x=150 \mu\text{m}$ ) from the LFC border. This maximum value of PL is correlated to a non-affected point of the sample surface with a maximum passivation quality. Notice that the PL signal has been normalized to this maximum value of the PL profile. This will allow us to compare measurements from different samples showing different passivation quality.

From this maximum value of PL intensity, the PL signal decreases progres-

sively when it gets closer to the contact border as a result of the reduction of the passivation performance around the contact. This reduction of the PL intensity can be semi-quantified by a PL loss (dashed shaded area of Figure 6.4b). In particular, this amount of PL loss can be considered as the level of passivation efficiency reduction induced by the laser firing process in the vicinity of the spots. Thus, from now on, the integration of this PL loss will be used to semi-quantify the impact of the laser processing and to compare data from different measurements. Concerning the integration limits in the x-axis, the integral was calculated from the physical border of the contact (vertical dashed line) up to 100  $\mu\text{m}$  away from this contact limit.

### 6.2.2.1 Laser power dependence

LFCs processed in  $\text{SiC}_x/\text{Al}_2\text{O}_3/\text{c-Si}$  stacks at different laser powers, i.e. 0.83, 0.98 and 1.44 W, have been studied in order to evaluate the effect of the laser power on the impact induced by the laser pulse. The obtained PL profiles are represented in Figure 6.5. For the sake of clarity, the PL profiles plotted here only show one half of the complete contact cross-section shown in Figure 6.4. In addition, the contact border depicted by the vertical dashed line has been positioned at  $x=0 \mu\text{m}$  for helping to the comparison among different PL profiles. Thus, the left part of the vertical dashed line defines the inner part of

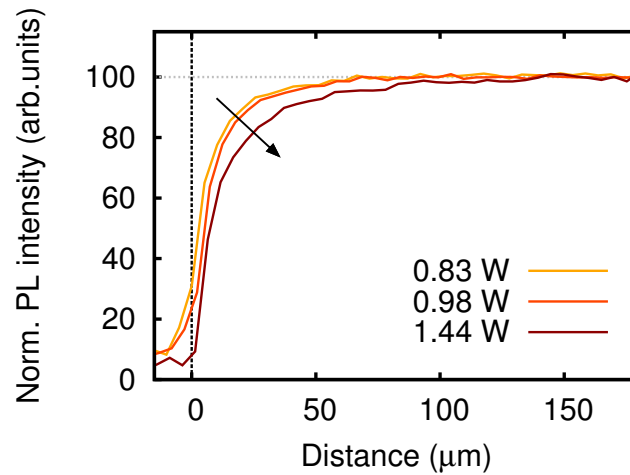


**Figure 6.5:** PL profiles recorded across LFCs processed at 0.83, 0.98 and 1.44 W in a  $\text{SiC}_x/\text{Al}_2\text{O}_3$ -passivated c-Si wafer. The limit of the contact is defined by the vertical dashed line at  $x=0 \mu\text{m}$ .

## 6.2. Local impact at the LFCs surroundings

---

the LFC, whereas the right side determines the region out of the contact. From now on, PL profiles of this section will be presented in this format. As already observed in Figure 6.4, the PL profiles here show a significant PL loss around the contact that we attribute to a reduction of the passivation quality. An increase of this PL loss, and therefore, an increase in the passivation quality reduction is observed for higher laser powers. In particular, a decay of the surface passivation quality up to approximately 100  $\mu\text{m}$  away from the spot border limit is observed for the most powerful laser process explored here.

### 6.2.2.2 Laser wavelength dependence

The observed local reduction in passivation efficiency induced by laser processing is believed to be linked to the thermal diffusion that takes place during the laser pulse and the contact formation. Since such a thermal dissipation strongly depends on the Si absorption coefficient and, as illustrated in Figure 3.5 (Section 3.1.2.1), the latter depends on the wavelength of the irradiation light, we have considered appropriate to study the dependence of the laser wavelength on the laser-induced impact. In order to do so, we have carried out micro-PL measurements in LFCs processed by a 355 nm laser in  $\text{SiC}_x/\text{Al}_2\text{O}_3/\text{c-Si}$  stacks. The obtained PL profiles are represented in Figure 6.6a, and the PL loss quantification (b) is compared to results obtained from LFCs processed with IR laser (Section 6.2.2.1). Two important particularities are observed. First, in contrast to the LFCs processed with the IR laser, the PL loss here does not increase with increasing the laser power. Interestingly, the same behavior was observed regarding the diameter of the UV LFCs (see Figure 6.2), which in contrast to the diameter of IR LFCs does not substantially increase with increasing laser power. A second important observation revealed by Figure 6.6b, is that the integrated PL loss for the UV LFCs is significantly lower than that observed for the LFCs processed with the 1064 nm laser. Nevertheless, as depicted in Figure 6.6c, if we normalize the PL loss by the LFCs diameter we observe that the PL loss, i.e. the reduction of the passivation efficiency, is proportionally higher for the LFCs processed by the UV laser. These results suggest that the use of UV lasers for LFC processing originates a higher reduction of passivation efficiency in front of IR lasers.

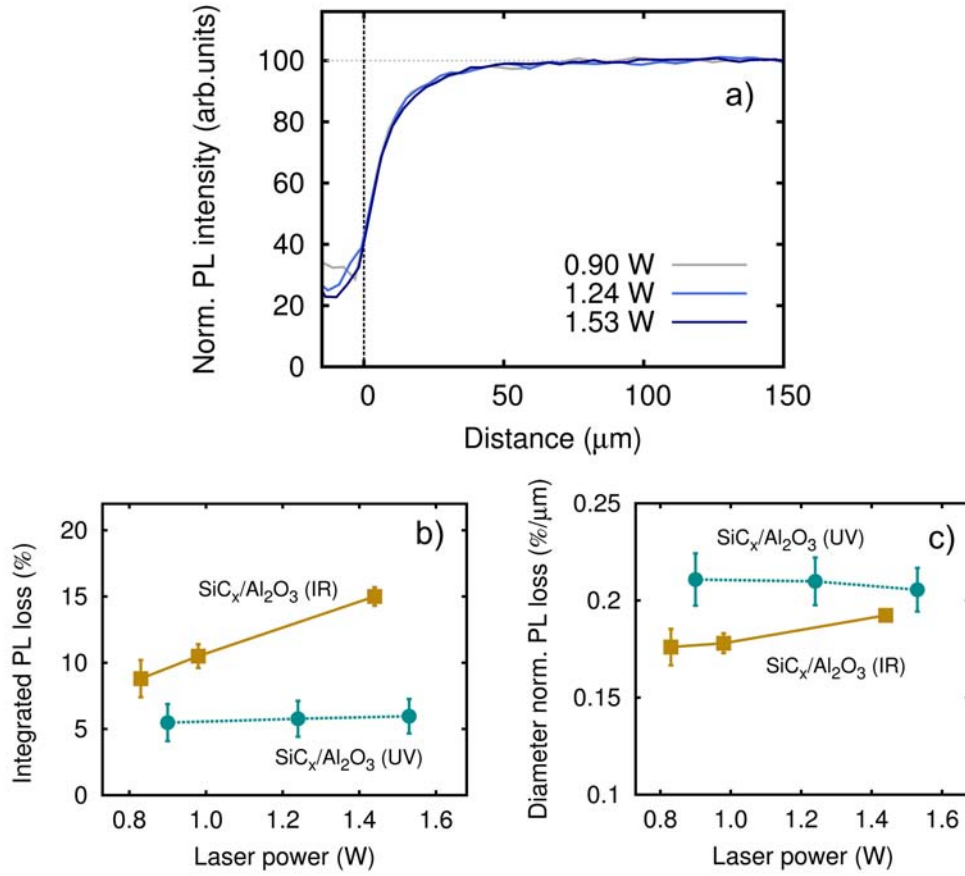


**Figure 6.6:** PL profiles recorded across LFCs processed at 0.90, 1.24 and 1.53 W in a  $\text{SiC}_x/\text{Al}_2\text{O}_3$ -passivated c-Si wafer with an UV laser (355 nm) (a). The integrated PL loss (according to the definition of PL loss described in this chapter) is represented as a function of the laser power, and compared to the integrated PL loss corresponding to LFCs processed in  $\text{SiC}_x/\text{Al}_2\text{O}_3$ /c-Si stacks using an IR laser (b). The integrated PL loss normalized by the LFCs diameter is also represented (c).

### 6.2.2.3 $\text{SiC}_x$ capping layer influence

The deposition of a  $\text{SiC}_x$  capping layer onto an  $\text{Al}_2\text{O}_3$  passivation layer is a common strategy used to improve the chemical and structural stability of  $\text{Al}_2\text{O}_3$ . In addition, when used on the rear side of a c-Si solar cell, a  $\text{SiC}_x$  acts as back reflector that reflects photons towards the bulk [116]. In this section, we study the effect of the presence of such capping layer on the impact induced by the laser pulse. For that, we compare the PL profiles of LFCs processed in

## 6.2. Local impact at the LFCs surroundings

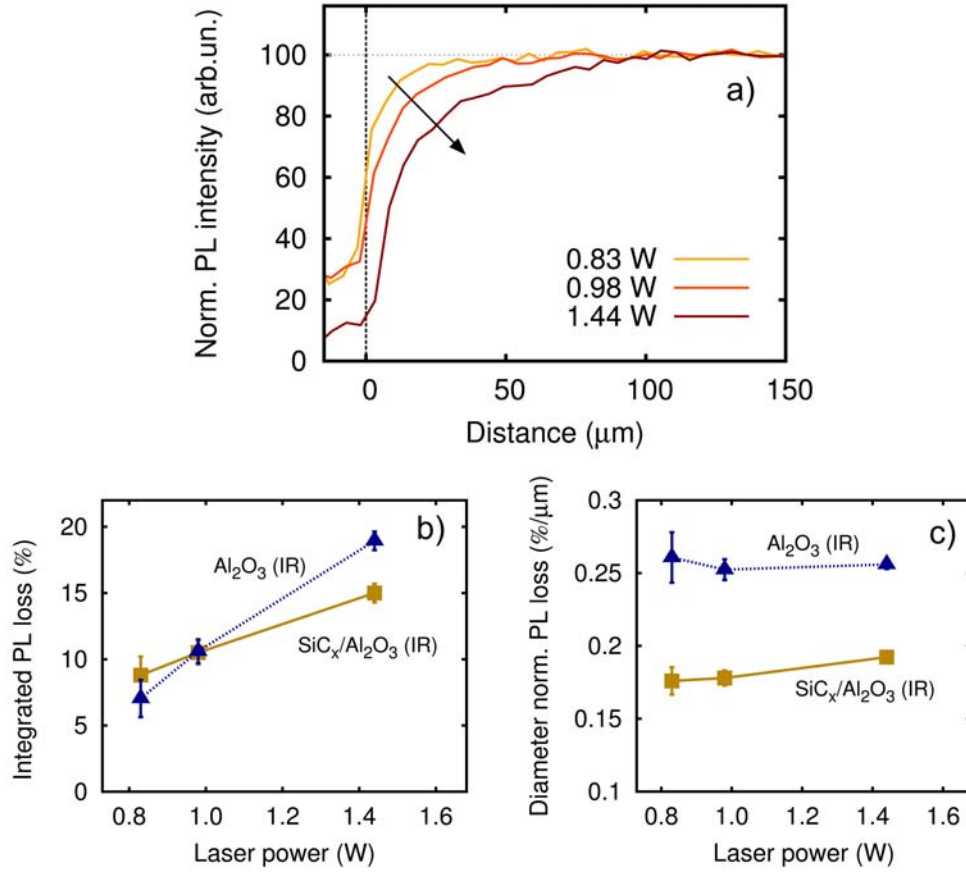


**Figure 6.7:** PL profiles recorded at the vicinity of LFCs processed at 0.83, 0.98 and 1.44 W (1064 nm laser) in an  $\text{Al}_2\text{O}_3$ -passivated c-Si wafer (a). The integrated PL loss is represented as a function of the laser power and compared to the PL loss corresponding to the LFCs processed with the same conditions in  $\text{SiC}_x/\text{Al}_2\text{O}_3$ -passivated c-Si wafers (b). The integrated PL loss normalized by the LFCs diameter is also represented (c).

$\text{SiC}_x/\text{Al}_2\text{O}_3/\text{c-Si}$  stacks (presented in Section 6.2.2.1) with micro-PL measurements recorded across LFCs processed in  $\text{Al}_2\text{O}_3/\text{c-Si}$  stacks. Results are shown in Figure 6.7. Again, we observe a significant reduction of the PL at the contact vicinity, which enlarges with increasing laser power. This enhancement of the PL loss is even higher than for the LFCs processed in  $\text{SiC}_x/\text{Al}_2\text{O}_3/\text{c-Si}$  stacks, as revealed by the higher slope in Figure 6.7b. If we normalize the PL loss by the LFCs diameter (Figure 6.7c), we observe two interesting aspects. The first one, as revealed by the horizontality of the PL loss curves presented in Figure 6.7c, is that the passivation efficiency reduction is much less dependent on the

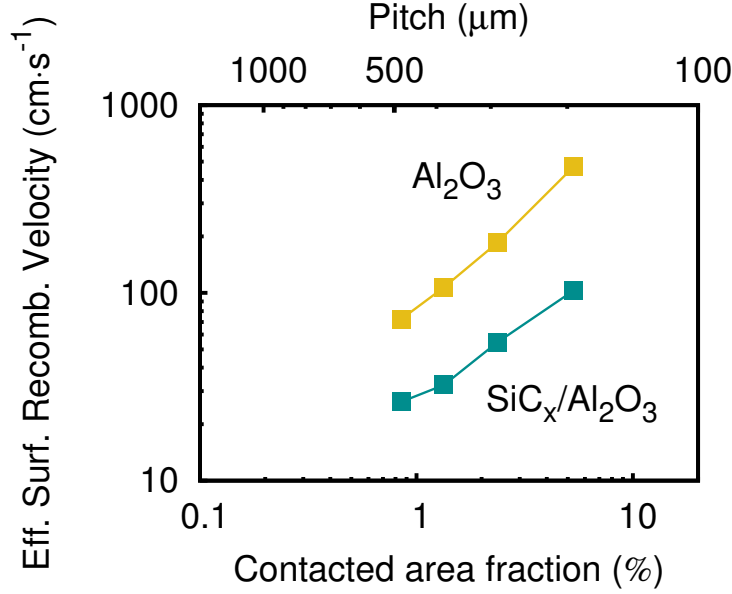


**Figure 6.8:** Effective surface recombination velocity at both laser-processed  $Al_2O_3$ - and  $SiC_x/Al_2O_3$  c-Si wafers. Extracted from [48].

laser power than expected from Figure 6.7b. This behavior can be explained by the fact that the increase of the LFCs diameter changes in the same proportion than the increase of the PL loss. The second important aspect to mention is that the LFCs processed in samples B, i.e. without the  $SiC_x$  capping layer, show a much higher impact, i.e. a much higher passivation efficiency reduction.

Keeping these results in mind, it is instructive to evaluate recent results from Ortega *et al.* [51], who studied the effective surface recombination velocity ( $S_{eff}$ ) at the laser processed surface of both  $Al_2O_3$ - and  $SiC_x/Al_2O_3$ -passivated c-Si wafers. Results are represented in Figure 6.8. As it can be seen, samples with the  $SiC_x$  capping layer show a lower  $S_{eff}$ . Ortega and co-workers suggested that the  $SiC_x$  layer could help to keep Al atoms close to the c-Si melted surface during the high temperature laser-stage, improving their diffusion into the substrate. This results in a better p+ Al-doped region below the contacted surface, and therefore, a lower surface recombination velocity at the contacts ( $S_{cont}$ ). Our results further suggest that the lower laser-induced impact observed in the samples that have the capping layer would be partially responsible of the observed lower  $S_{eff}$  for the samples with  $SiC_x$ . From these findings we can conclude that the presence of a  $SiC_x$  minimizes the impact of the laser pulse on the passivation layer.



## 6.2. Local impact at the LFCs surroundings

**Table 6.2:** Energy-Dispersive X-ray (EDX) spectroscopy data obtained in random points of both the  $\text{Al}_2\text{O}_3$ -passivated sample and the sample treated by HF.

element	$\text{Al}_2\text{O}_3$ -passivated		etched by HF	
	wt. (%)	at. (%)	wt. (%)	at. (%)
Carbon	13.29	26.53	8.89	19.14
Oxygen	3.39	5.07	-	-
Aluminum	0.57	0.51	-	-
Silicon	78.85	67.31	87.18	80.24
Palladium	1.04	0.23	0.97	0.24
Gold	2.86	0.35	2.95	0.39

### 6.2.3 Impact of the laser pulse on the c-Si bulk

We also wanted to study if the reduction of the passivation efficiency observed around the contact is only attributed to changes in the passivation layer, or otherwise, is also related to changes in the Si bulk. In order to study so, the same micro-PL measurements performed in  $\text{Al}_2\text{O}_3$ -passivated wafers have been carried out after the  $\text{Al}_2\text{O}_3$  layer was removed by HF etching (sample C).

First, in order to prove that the alumina layer has been correctly removed, we have performed Energy-Dispersive X-ray (EDX) spectroscopy analysis on both, the  $\text{Al}_2\text{O}_3$ -passivated wafers and the ones treated by HF etching. As shown in Table 6.2, the results reveal that traces of Al and O were detected in the  $\text{Al}_2\text{O}_3$ -passivated Si, whereas the HF-treated sample did not show any trace of Al and O. Note that Au and Pt comes from the conductive coating used in Scanning Electron Microscopy (SEM) analysis for avoiding charging effects, and therefore, they have not to be considered. Moreover, C content (always present in EDX data) comes from the dust on the sample surface, so again it has not to be taken into account here.

Figure 6.9 shows the PL profiles recorded across a LFC processed in sample C, i.e. after etching the dielectric layer. As it can be seen, PL profiles almost do not evidence any PL loss at the contact surroundings, showing that LFC processes do not apparently affect the c-Si bulk. This conclusion is in great agreement with the results presented in the next section, where an extensive micro-Raman spectroscopy analysis of LFCs reveals that c-Si structure only suffers structural changes inside the laser processed region, but not at the surrounding regions. With all these findings, we can confirm that the reduction

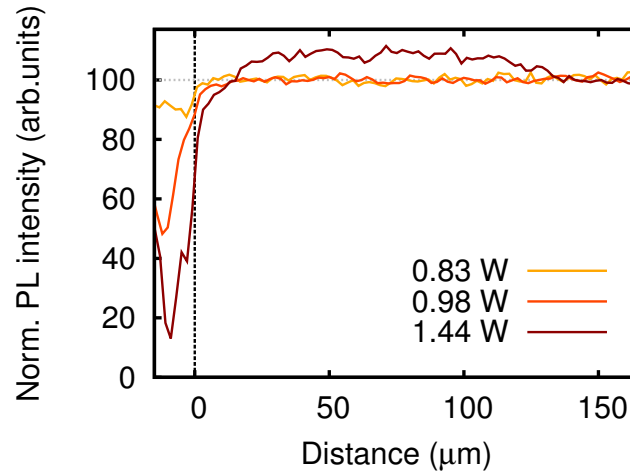


**Figure 6.9:** PL profiles recorded at the surroundings of three LFCs processed at 0.83, 0.98 and 1.44 W in an  $\text{Al}_2\text{O}_3$ -passivated c-Si sample after the  $\text{Al}_2\text{O}_3$  was removed by immersion in a HF bath.

in passivation efficiency observed at the LFCs vicinities is solely linked to a worsening of the passivation capabilities of the dielectric layer.

An unexpected feature is observed in Figure 6.9 for the 1.44 W PL profile. The HF-etched sample shows a region (from 10 to 130  $\mu\text{m}$  of the x-axis) with a higher PL intensity than the PL value related to a non-affected point of the sample surface ( $x=150 \mu\text{m}$ ). Supported by data presented in Figure 6.10, we attribute this effect to a heating-induced Al crystallization from the  $\text{Al}_2\text{O}_3$  layer, which could not be eliminated by the HF etching. This Al crystallization would take place during the LFC formation. As it can be seen in Figure 6.10, the sample surface region far away from the LFC border, i.e. region A2, shows a flat surface with a constant Surface Potential (SP) value of -0.15 V, which we associate to the raw HF-etched Si surface. In contrast, when we get closer to the LFC border (region A3), the sample surface evidence small structures with a spherical geometry of about 200-400 nm in diameter and 10-30 nm in height. The corresponding SP map (Figure 6.10f) reveals that these structures have associated a higher SP value, whereas the SP of the Si substrate is kept at the previously mentioned -0.15 V. The marked difference between SP values suggests that such spherical structures correspond to a different phase than Si. In addition, the fact that LFCs processed at lower laser powers, i.e. 0.83 and 0.98 W, showed neither the spherical structures, nor the higher PL signal increase around the contacts, strengthen the suggested hypothesis about the

## 6.2. Local impact at the LFCs surroundings

heating-induced Al crystallization from the  $\text{Al}_2\text{O}_3$  layer.

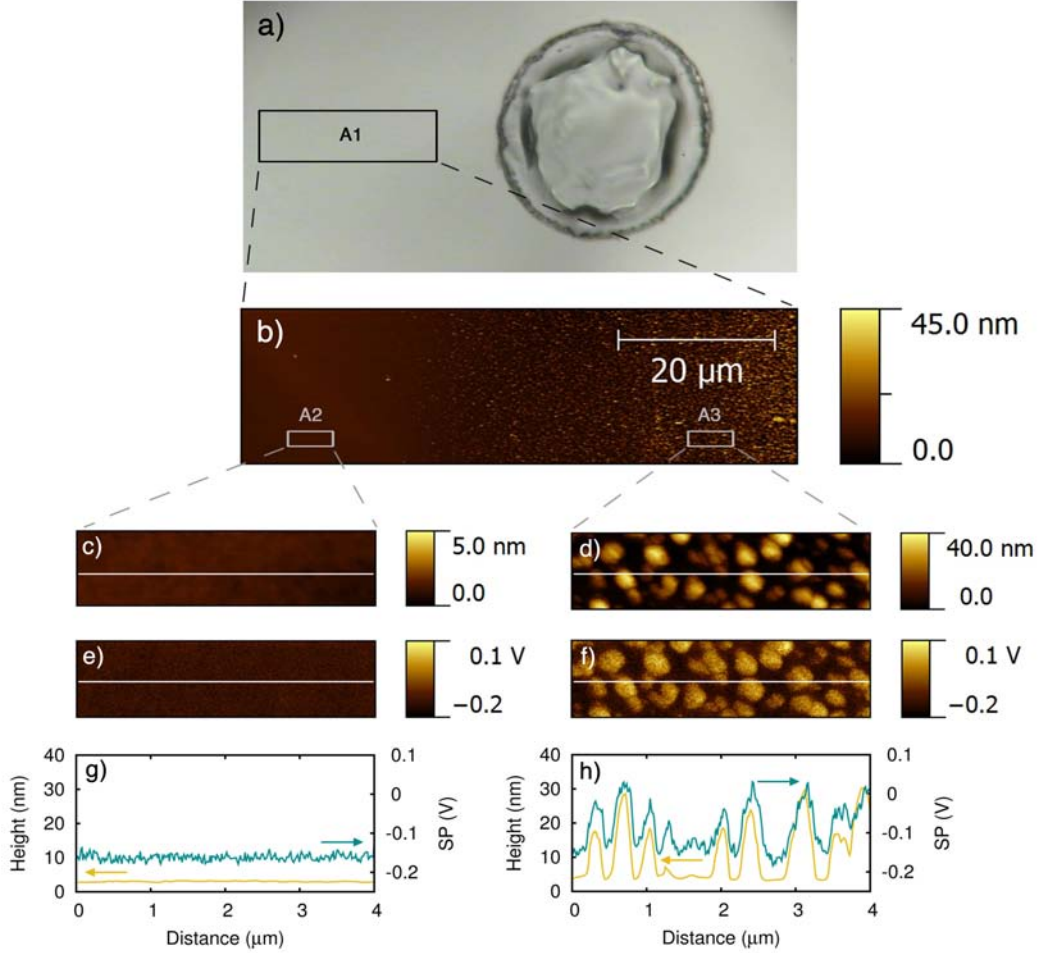


**Figure 6.10:** Optical microscope image (a) of a single LFC in a sample C, and topography map (b) recorded by KPFM at the selected area A1. Topography map (c), SP map (e), and the corresponding topography and SP profiles (g) of the selected area A2 (far from the LFC border) are represented. The homologous topography map (d), SP map (f) and the corresponding topography and SP profiles (h) of area A3 (closer to LFC border) are also depicted.

### 6.2.4 Estimation of passivation performance reduction

Micro-PL results presented in the previous sections demonstrate that  $S_{\text{eff}}$  in a laser-processed surface can not be solely determined by the surface recombination velocity correlated to the unprocessed sample surface ( $S_{\text{pass}}$ ) and the

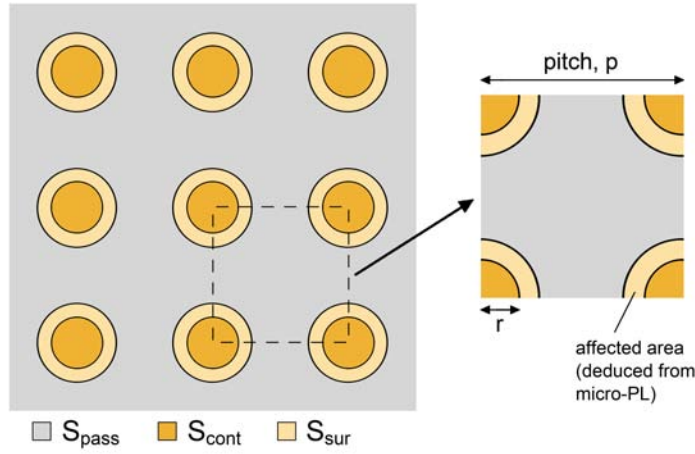


**Figure 6.11:** Representation of a squared matrix array of LFCs. Regions with a characteristic Surface Recombination Velocity (SRV) are indicated:  $S_{\text{pass}}$  concerns to the SRV of the non-processed area,  $S_{\text{sur}}$  corresponds to the SRV of the affected contacts surroundings and  $S_{\text{cont}}$  refers to SRV inside the contact.

recombination velocity assigned to the contacts ( $S_{\text{cont}}$ ) (see Section 2.3.3.1). Indeed, a third contribution concerning the laser affected area must be taken into account. The surface recombination velocity at the area affected by laser processing will be referred from now on as  $S_{\text{sur}}$ . In analogy to Figure 2.13 (Section 2.3.3.1), Figure 6.11 shows a sketch of a square matrix layout of LFCs indicating the different regions with a characteristic recombination velocity. In addition to  $S_{\text{pass}}$  and  $S_{\text{cont}}$ , here  $S_{\text{sur}}$  is considered.

From the geometrical parameters illustrated in the scheme on the right-hand side of Figure 6.11, we have estimated the percentage of affected area for different values of contacted area fraction and pitch. In order to calculate it, we have assumed a contact diameter of  $50\text{ }\mu\text{m}$  and a characteristic decay of the surface passivation quality, i.e. an enlargement of the laser affected area, of  $100\text{ }\mu\text{m}$  away from the spot border limit, as observed in the obtained micro-PL profiles. In addition to the percentage of affected area, we have also estimated the percentage of passivation performance reduction. The latter is a semi-quantification of the loss in passivation efficiency of the dielectric layer calculated from the local loss in PL deduced from micro-PL analysis (see Section 6.2.2). The results of these calculations are represented in Figure 6.12. For values of contacted area fraction below 1%, the estimated reduction in passivation efficiency is kept below around 3%. In contrast, for values of contacted

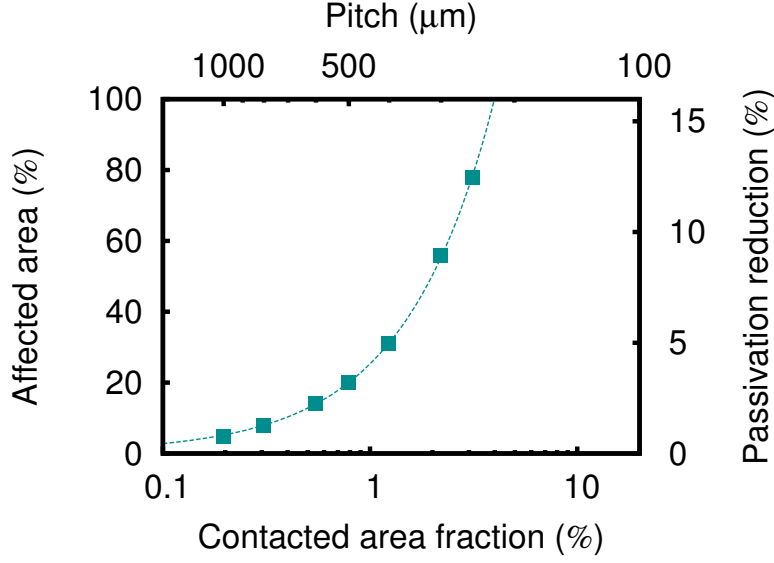


**Figure 6.12:** Percentage of affected area and estimation of the percentage of passivation performance reduction (calculated from the loss in PL deduced from micro-PL analysis) against the contacted area fraction (and the pitch). Calculations have been done assuming a spot diameter of 50  $\mu\text{m}$  and a characteristic affectation of 100  $\mu\text{m}$  away from the spot border limit.

area fraction above 1%, the amount of area affected by laser processing starts to increase significantly and the passivation reduction reaches values above 10% for pitch values of 300  $\mu\text{m}$ .

### 6.2.5 Effective surface recombination velocity at the laser-processed surface

In order to obtain a comprehensive insight about the impact of the laser processing on the final performance of a solar cell, we have determined  $S_{\text{eff}}$  at laser-processed surface. Since the surface having the LFCs can be considered as the final rear surface of a solar cell, the effective surface recombination velocity at the laser processed surface can be labeled as  $S_{\text{rear}}$ .  $S_{\text{rear}}$  was calculated from the effective lifetime ( $\tau_{\text{eff}}$ ) at 1 sun, i.e.  $\Delta n = 10^{15} \text{ cm}^{-3}$ , measured by Quasi Steady State Photo-Conductance (QSSPC). To obtain  $S_{\text{rear}}$  we should subtract the recombination at the non-treated surface and the intrinsic bulk recombination according to:

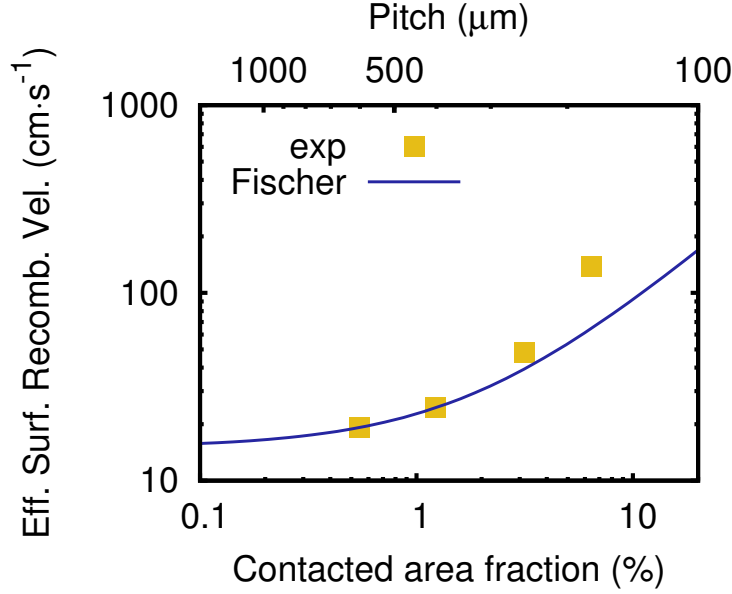


**Figure 6.13:** Effective surface recombination velocity ( $S_{\text{eff}}$ ) in a laser processed  $\text{SiC}_x/\text{Al}_2\text{O}_3$  stack as a function of the contacted area fraction. The corresponding pitch is also represented. Data points were adjusted to the Fischer's model.

$$S_{\text{rear}} = w \left( \frac{1}{\tau_{\text{eff}}} - \frac{1}{\tau_{\text{int}}} \right) - S_0, \quad (6.1)$$

where  $w$  is the wafer thickness,  $\tau_{\text{int}}$  is the intrinsic lifetime and  $S_0$  is the surface recombination velocity at the non-treated surface. The latter was deduced from a sample without laser processing, i.e.  $f_c=0\%$  sample. Data points are represented in Figure 6.13 against the pitch and the corresponding contacted area fraction considering a spot diameter of  $50 \mu\text{m}$ . Results were obtained from four  $\text{SiC}_x/\text{Al}_2\text{O}_3/\text{c-Si}$  samples with pitch values of 600, 400, 250 and  $175 \mu\text{m}$ . Experimental data are adjusted to Fischer's model (see Section 2.3.3.1), which can be used to predict  $S_{\text{eff}}$  of surfaces showing a squared matrix layouts of LFCs [46]. Fischer analytical model was calculated considering a  $S_{\text{cont}}$  of  $900 \text{ cm/s}$ , and a  $S_{\text{pass}}$  of  $15 \text{ cm/s}$ . As it can be seen, for long values of pitch, i.e. small contacted area fractions, the model adjusts well with the experimental data. However, as pitch value decreases, i.e. point contacts approach each other, the model predicts underestimated values of  $S_{\text{eff}}$ . We correlate this underestimation to the fact that the decay in the surface passivation at the contact surroundings demonstrated by micro-PL measurements is not included in Fischer's model. For long pitches, i.e. low contacted area fractions, the model is

### 6.3. Doping profiles in laser-fired contacts

---

able to incorporate this distortion by increasing the  $S_{\text{cont}}$  parameter where all the calculated recombination is considered. However, for short pitches there is a strong deviation from the model resulting in invalid  $S_{\text{cont}}$  values. Interestingly, the value of contacted area fraction where the model starts to deviate, i.e. around 2%, is in good agreement with data points of Figure 6.12, where the percentage of passivation efficiency reduction starts to increase significantly for values of contacted area fraction above 1%. For all these reasons, we believe that for a correct determination of  $S_{\text{cont}}$ , the reduction in surface passivation around the LFCs must be considered. Then, detailed 3D simulations would be necessary to correctly predict a pitch-dependent  $S_{\text{cont}}$  of laser-processed surfaces.

## 6.3 Doping profiles in laser-fired contacts <sup>2</sup>

A key feature for the good operation of the LFC approach is the formation of an Al-doped p+ region under the contacted surface area. As already mentioned in Section 2.3.1, this p+ region creates a local back-surface field (BSF) that induces a relatively low recombination velocity below the contacts, and in addition, ensures a low-contact resistance independently of the substrate resistivity. Hence, the characteristics of the Al-alloyed p+ region have a crucial effect in the performance of the final device. Nevertheless, the small dimensions of LFCs difficult their study and characterization, and therefore, there is still a lack of information about the specific features of this p+ region.

In the present section, we have carried out high-resolution micro-Raman and micro-PL spectroscopy measurements on different LFCs processed in  $\text{Al}_2\text{O}_3$ -passivated c-Si samples. Thanks to the high lateral resolution down to 1  $\mu\text{m}$  achieved in our experiments, we have been able to perform a detailed study of relevant LFC properties such as the doping profile, induced-stress and crystallinity fraction of the Si region being processed. This gives us an important insight about the LFC formation. The study has been applied in three LFCs processed at different incident laser power in order to analyze the influence of the laser power on the studied features.

---

<sup>2</sup>The measurements presented in this section have been carried out in the *Laboratoire de Génie Electrique de Paris (LGEF)* in the context of a collaboration between MatGas, the Universitat Politècnica de Catalunya (UPC) and the LGEF. The experiments have been performed under the supervision of Dr. José Álvarez of the Semiconductor and Thin Films group led by Prof. Jean-Paul Kleider.

### 6.3.1 Experimental methodology

#### 6.3.1.1 Materials and samples

The samples used to carry out the present study are the same as the ones used in Section 6.2 to characterize the impact of the laser pulse around the LFCs. In particular, all the measurements presented in this section have been performed in laser-processed  $\text{Al}_2\text{O}_3$ -passivated c-Si wafers in which the  $\text{Al}_2\text{O}_3$  layer has been removed by HF etching (see Section 6.2.1 for more details). Additionally, boron-doped FZ c-Si wafers with different doping densities, namely  $1 \times 10^{14}$ ,  $1 \times 10^{15}$ ,  $1 \times 10^{17}$ ,  $1 \times 10^{18}$ ,  $5 \times 10^{18}$  and  $1 \times 10^{20} \text{ cm}^{-3}$  were used to obtain reference Raman and PL spectra. From these reference Raman and PL spectra we have obtained calibration curves that have been used to quantify the doping density from the obtained Raman and PL data.

#### 6.3.1.2 Equipment details

Micro-Raman and micro-photoluminescence (PL) experiments were carried out with a WITEC Alpha300. A diode-pumped laser with a wavelength of 532 nm was used as excitation source resulting in a penetration depth of about 1  $\mu\text{m}$ . Micro-Raman and micro-PL measurements were performed with a 100x VIS (Visible), NA (numerical aperture)=0.9 and a 20x IR, NA=0.45, respectively. The resulting beam spot size on the sample surface is in diameter below 1  $\mu\text{m}$  and 2  $\mu\text{m}$  for Raman and PL measurements, respectively. Raman scattering signal was recorded through a 300 mm imaging spectrometer equipped with both a 600 lines/mm and 1800 lines/mm grating, and a 1024 x 127 CCD camera visible-optimized, whereas PL signal was collected through an additional 300 mm spectrometer composed of two gratings (150 and 300 lines/mm) and a 1024 x 1 pixel linear InGaAs photodiode array optimized for spectroscopy applications in the range 1-1.7  $\mu\text{m}$ . It is worth to mention that the incoming laser power on the sample surface for the Raman measurements was always kept below 3 mW in order to avoid both an excessive local heating of the sample surface, and the generation of Fano resonances induced by the free carriers introduced by high Continuous-Wave (CW) laser power densities [117]. The later effect is demonstrated in Figure 6.14 for laser power values above 5 mW. From now on, in order to ease the observation of Fano effect, some of the Raman spectra presented in this Section will be represented in a semi-log scale.



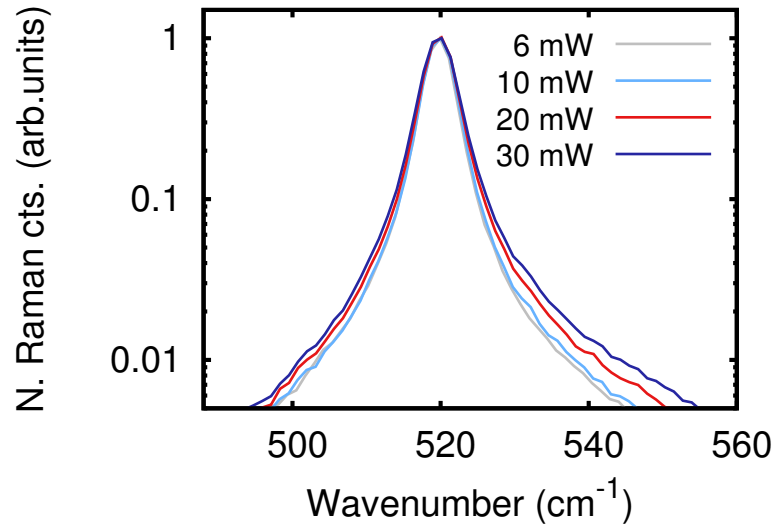


**Figure 6.14:** Observation of Fano resonances induced by photo-generated holes using laser power values above 5 mW.

Local electrical measurements through the Conductive-Atomic Force Microscopy (C-AFM) technique were performed using a Nanoscope IIIa Multi-mode AFM (Digital Instruments) associated with the home-made conducting probe extension called "Resiscope". This extension allows us to apply a stable DC bias voltage (from -10 to +10 V) to the sample and to measure the resulting current flowing through the tip as the sample surface is scanned in contact mode, yielding a local resistance map covering resistance values in the range  $10^2$ - $10^{12} \Omega$ . Current-Voltage (I-V) measurements are also permitted with this extension. Highly-Boron Doped (HBD) diamond-coated Si AFM cantilevers, with an intermediate spring constant of about 3 N/m, proved to be the most suitable AFM tips for making electrical measurements on LFCs.

## 6.3.2 Characterization by micro-Raman spectroscopy

### 6.3.2.1 Doping profiles

As stated in Section 3.2.2, doping profiles in c-Si can be monitored by studying both the width [118] and the so-called Fano resonance [119] of the first order c-Si Raman peak. The Fano resonance is evident in the Si Raman peak at hole concentrations above  $10^{18} \text{ cm}^{-3}$  by a characteristic asymmetry of the Raman

line, which results from the resonant interaction between the discrete phonon states and a continuum of hole states [120, 121, 122]. The Raman peak line shape can be described by the following expression:

$$I_{\text{ram}}(w) = I_0 \frac{[q_F + 2(w - w_{\text{max}})/\Gamma]^2}{1 + [2(w - w_{\text{max}})/\Gamma]^2} \quad (6.2)$$

where  $I_0$  is a scaling factor,  $w_{\text{ph}}$  is the frequency associated to the Raman peak maximum,  $\Gamma$  corresponds to the Full Width at Half Maximum (FWHM) of the Raman peak and  $q_F$  is the asymmetry parameter, which can be used to monitor the doping level of the sample under study. The lower the  $q_F$  parameter, the higher the doping level. Fano resonances for n-type c-Si samples has been also observed for electron concentrations above  $10^{20} \text{ cm}^{-3}$  [123].

Figure 6.15 shows the optical microscope images (left-hand side) and the corresponding Raman peak FWHM maps (right-hand side) of the three LFCs under study processed at 0.98 (a, b), 1.1 (c, d), and 1.43 W (e, f). The corresponding LFC diameters are 43.8, 54.5 and 74.2  $\mu\text{m}$ , respectively. For ensuring a good observation of the obtained data, the microscope images and the Raman maps of the three contacts have been represented with a slightly different scale. Also for clarity, the physical dimensions of the LFCs have been represented in Raman maps by a green dotted circle. As explained above, the FWHM of the first order Raman peak can be used to monitor the doping level of the sample under study. Hence, the zones that evidence an increase of the Raman peak width in Figure 6.15 (brighter zones) are qualitatively correlated to zones with a higher doping level. The LFC processed at 0.98 W evidences slightly higher levels of doping at the central part of the contact. In contrast, the contact processed at 1.1 W (Figure 6.15d) evidences a brighter concentric corona pointing out a wider Raman peak and consequently an increase of the doping level. Following the same trend, for the contact processed using the higher laser power (Figure 6.15f), the border of the contact is the area that evidences a higher level of doping. The different Raman maps illustrated in Figure 6.15 demonstrate that the laser power plays an important role on the distribution of the highly-doped regions inside the contacts. More precisely, results point out that for higher laser powers, the highly doped regions moves towards the border of the contact.

### 6.3. Doping profiles in laser-fired contacts

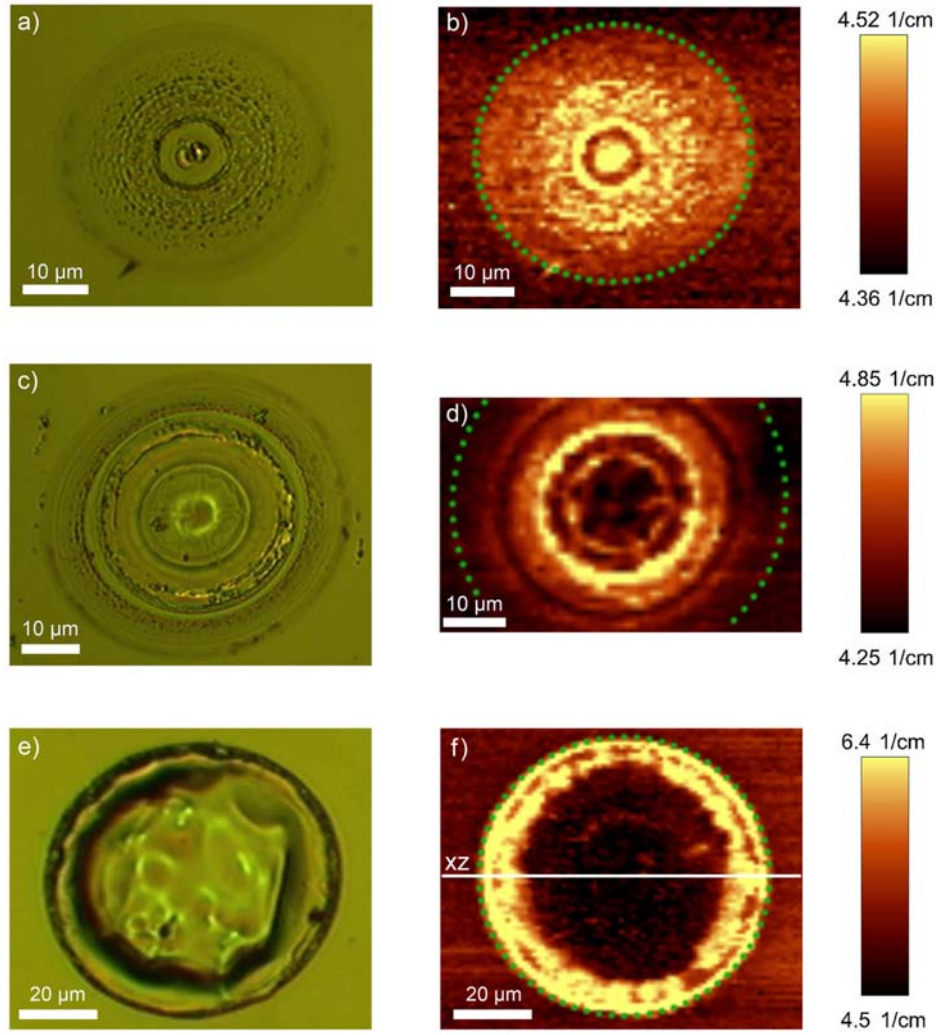


**Figure 6.15:** Optical microscope images (left-hand side) and Raman peak width maps (right-hand side) of the three LFCs under study processed at 0.98 (a, b), 1.1 (c, d) and 1.43 W (e, f). The physical dimensions of the different LFCs are delimited by dotted circles. Brighter zones in the Raman peak width maps correspond to zones with higher doping density. Horizontal line labeled as XZ defines the perpendicular plane (to the sample surface) across the Raman maps of Figure 6.16 were obtained.

### 6.3.2.2 Vertical XZ Raman maps

Due to the formation of the contact cavity, LFC morphology shows variations in height. In particular, as observed in the topography map of Figure 6.3 (see Section 6.2.2), LFCs processed at 1.43 W can show differences in height of at least  $3\text{ }\mu\text{m}$ . Since the Raman maps presented in this Section were recorded at a constant height by means of confocal microscopy, and the penetration depth of the incident 532 nm laser beam is approximately  $1\text{ }\mu\text{m}$ , we wanted to verify that height variations of LFCs have not had influence on the results shown by Raman maps of Figure 6.15. In order to confirm this, we have recorded vertical Raman maps across a 1.43 W LFC. Such vertical Raman maps that are perpendicular to the sample surface, have been recorded across the XZ horizontal line depicted in Figure 6.15f. The obtained vertical Raman maps are represented in Figure 6.16.

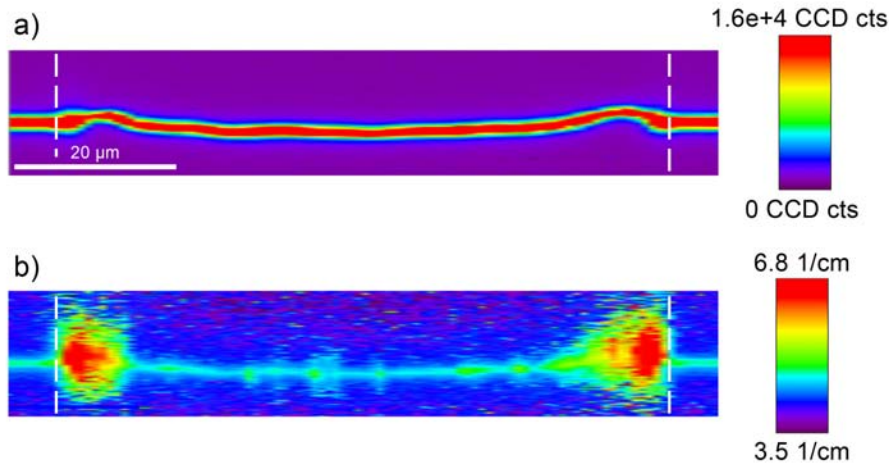


**Figure 6.16:** Confocal Raman maps recorded along the XZ plane of a LFC processed at 1.43 W (see Figure 6.15f). The good confocality allows the precise identification of the surface location in both the Raman peak intensity map (a) and the Raman peak width map (b). The white vertical dashed lines define the contact external limits.

The good confocality of the measurements is evidenced by the first order Si Raman peak intensity map (Figure 6.16a), where we can clearly identify the location of the sample surface by a drastic increase of the Raman signal. This large increase of the Raman signal draws the surface morphology, and in turn, helps to identify the complete contact morphology and the contact borders.

### 6.3. Doping profiles in laser-fired contacts

The contact limits are roughly depicted by the white vertical dashed lines. The location of the sample surface is also identified in the Raman peak FWHM map of Figure 6.16b by a slight increase in the peak width. As it can be seen, the peak further widens at the border of the contact, confirming that variations in Raman peak width observed in Figure 6.15 are not induced by variations in contact height.

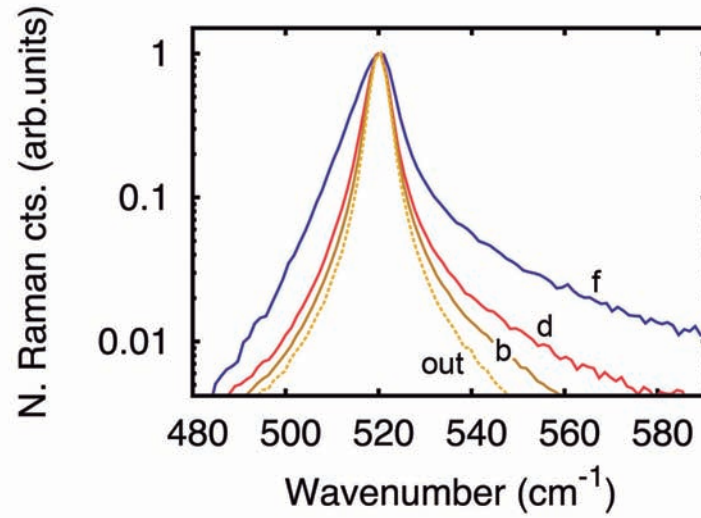


**Figure 6.17:** Averaged Raman spectra corresponding to the brighter zones of maps b, d, and f of Figure 6.15. For comparison, an averaged Raman spectra corresponding to an unprocessed surface area has been also represented (yellow dashed line).

Discarded the idea that the contact morphology affects the results obtained from confocal horizontal Raman maps, the correlation between the Raman peak widening observed in Figure 6.15 and the increase in doping density is confirmed by data shown in Figure 6.17. This figure shows the averaged Raman spectra corresponding to the brighter zones, i.e. zones with higher doping, of images b, d and f of Figure 6.15. An averaged spectrum corresponding to an unprocessed area (outer region of LFC) is also shown (yellow dashed line). As it can be observed, the Fano resonance is clearly identified for all Raman spectra except for the one obtained out of the LFC, which shows a symmetric Raman line shape. This qualitatively confirms that the brighter zones in maps of Figure 6.15 are correlated to areas with a higher doping level. In addition, we can also observe in Figure 6.17 that the LFCs processed with a

higher laser power have associated a higher Fano asymmetry. Hence, the use of higher laser powers results in LFCs with higher doping densities.

### 6.3.2.3 Crystalline fraction of LFCs

In order to get further insights about the LFCs formation, we depict in Figure 6.18 the Raman spectra recorded at three specific points (r1, r2, and r3) inside two LFCs processed at 1.1 W (r1, r2) and 1.43 W (r3). A fourth Raman spectrum corresponding to a non-processed surface area is also represented as a reference. As it can be observed, in addition to the first order c-Si Raman line positioned at  $520.9 \text{ cm}^{-1}$ , a second Raman line is also observed at lower

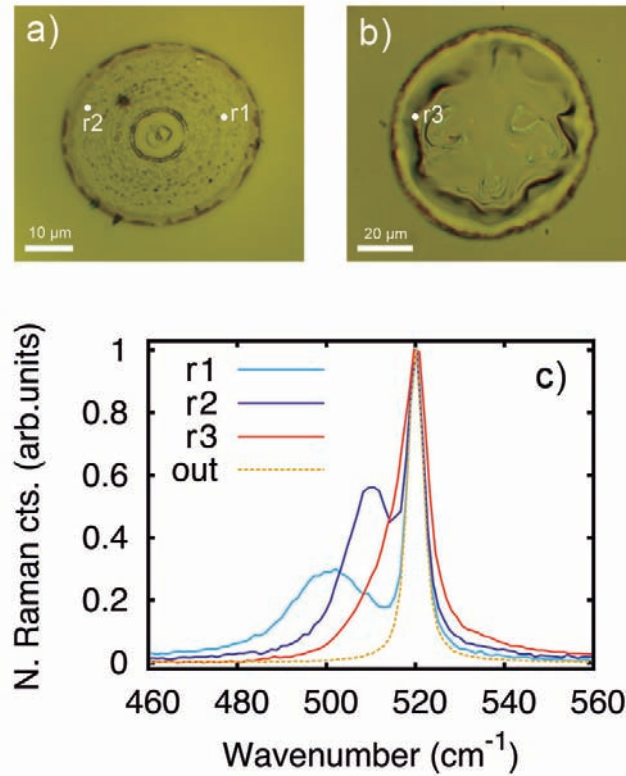


**Figure 6.18:** Raman spectra obtained at specific points inside LFCs processed at 1.1 W (r1, r2) (a) and 1.43 W (r3) (b). In addition to the first order Raman peak, a second peak characteristic of micro-crystalline silicon sets in at lower wavenumbers. For comparison, a Raman peak related to an unprocessed area (outer region of LFCs) is also depicted (c).

### 6.3. Doping profiles in laser-fired contacts

---

frequencies. This new Raman line that appears at frequencies in the range between 500 and 515  $\text{cm}^{-1}$  is characteristic of microcrystalline silicon [124, 125]. Its observation at specific points inside the LFCs suggests that melted Si material fraction solidify in micro-crystalline manner, at least at specific zones inside the contacted area. The first order c-Si Raman line is the main feature of Raman spectra of Figure 6.18, which confirms that the crystalline fraction is the main component in the analyzed material volume. The three micro-crystalline-related Raman lines show different features in terms of peak intensity and frequency. We correlate these variations to the presence of different crystalline fractions in the analyzed material volume.

The contribution of microcrystalline-Si components to the obtained Raman spectra is further confirmed by the fact that all averaged Raman spectra recorded inside the LFCs could be significantly better fitted using a rewriting of Equation (6.2) that considers a second Lorentzian function related to the contribution of the microcrystalline Si formation. In fact, the expression that has been used to fit the Raman data is:

$$I_{\text{ram}}(w) = I_0 \frac{[q_F + 2(w - w_{\text{max}})/\Gamma]^2}{1 + [2(w - w_{\text{max}})/\Gamma]^2} + \frac{A_{\text{mc}}}{1 + [2(w - w_{\text{mc}})/\Gamma]^2} \quad (6.3)$$

where  $A_{\text{mc}}$  corresponds to the Raman peak intensity related to the microcrystalline-like component and  $w_{\text{mc}}$  is related to the frequency of the microcrystalline-like peak maximum. It is worth to mention that the position of the second Lorentzian function was limited to values between 505 and 517  $\text{cm}^{-1}$ .

#### 6.3.2.4 Doping level quantification

As observed in Figure 6.19 for a LFC processed at 1.1 W, the fit of Raman spectra using Equation (6.3) shows very good adjustment paving the way to obtain a reliable quantification about the doping level inside the LFCs.

Table 6.3 shows the  $q_F$  asymmetry parameters resulting from the best fit of Equation (6.3) to the Raman spectra correlated to the highly-doped regions of the three LFCs under study. Data were calculated from at least two LFCs for each one of the three values of laser power. The obtained  $q_F$  parameters decrease with increasing laser power, and therefore, the use of higher laser powers leads to LFCs with higher doping densities. The quantification of the doping density associated to the obtained  $q_F$  parameters has been calculated from the calibration curve represented in Figure 6.20. This plot shows the relationship between the doping density and the measured  $q$  parameter



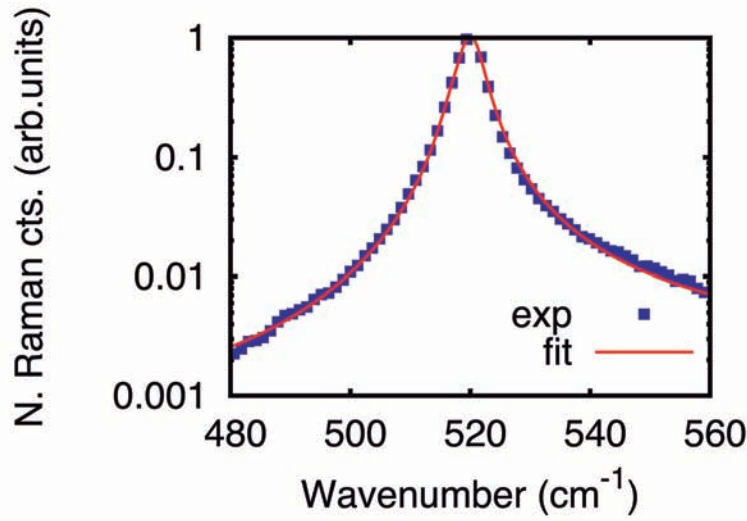


**Figure 6.19:** Fit of the Raman spectrum corresponding to the highly-doped region of a 1.1 W LFC using equation (6.3). The fit resulted in a  $q_F$  parameter of 61 which corresponds to a doping level of  $8.4 \times 10^{18} \text{ cm}^{-3}$ .

**Table 6.3:**  $q_F$  asymmetry parameter obtained from the fit of Equation (6.3) to the averaged Raman spectra corresponding to the highly-doped regions of the three LFCs under study. The resulting doping densities were calculated using the calibration curve shown in Figure 6.20.

laser power (W)	$q_F$ parameter (arb.units)	doping density ( $\times 10^{18} \text{ cm}^{-3}$ )
0.98	$90 \pm 7$	4.6 - 5.7
1.10	$61 \pm 4$	7.7 - 9.1
1.43	$16 \pm 2$	31.9 - 41.7

extracted from the reference calibration wafers showing different doping densities (see Section 6.3.1.1). The obtained curve is compared to calibration curves reported by Kunz *et al.* [118], Becker *et al.* [119] and Gundel *et al.* [126], which roughly show the same behavior. According to our calibration curve, we have obtained maximum doping levels in the range of  $4.6\text{-}5.7 \times 10^{18}$ ,  $7.7\text{-}9.1 \times 10^{18}$  and  $3.2\text{-}4.2 \times 10^{19} \text{ cm}^{-3}$  for the LFCs processed at 0.98, 1.10 and 1.43 W, respectively. It is important to remark that the intensity of the second Lorentzian peak related to the microcrystalline component was observed to increase with higher



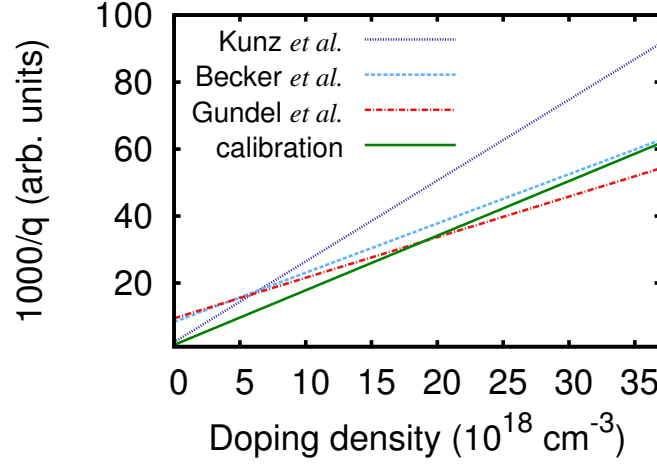


**Figure 6.20:** Relationship between the doping density and the  $q_F$  parameter. Our calibration curve was obtained from calibration reference wafers with distinct doping densities and is compared to different curves reported in the literature[118, 119, 126].

laser powers. This suggests that the use of higher laser powers decreases the crystalline fraction of the solidified Si volume.

#### 6.3.2.5 Induced stress at the laser processed region

As stated in Section 3.2.2, the shape of the first order c-Si Raman peak can suffer variations correlated to changes in the Si properties. For instance, a shift of the Raman peak maximum can be associated to the presence of stress in the Si structure. In this Section we study possible variations in the Si Raman peak position by monitoring the center of mass of the first order c-Si Raman peak. The center of mass of Raman peak ( $w_{cm}$ ) is obtained by calculating the weighted arithmetic mean of the Raman spectrum points according to:

$$w_{cm} = \frac{w_1 I_1 + w_2 I_2 + \dots + w_n I_n}{I_1 + I_2 + \dots + I_n}, \quad (6.4)$$

where  $w_1, w_2, \dots, w_n$  are the frequency points of the Raman spectrum range where the center of mass is calculated and  $I_1, I_2, \dots, I_n$  are the Raman intensity values correlated to the  $w_1, w_2, \dots, w_n$  frequency points.

Figure 6.21a shows the Raman spectra center of mass map of a LFC processed at 1.43 W. The Raman spectra of the selected points (s1, s2 and s3) are

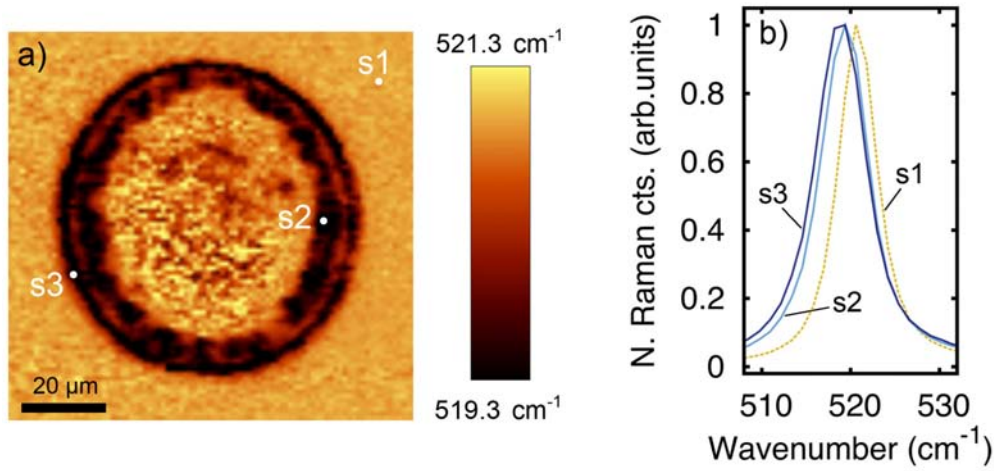


**Figure 6.21:** Raman spectra center of mass map of a LFC processed at 1.43 W (a). The specific Raman spectra associated to points s1, s2 and s3 are also plotted (b).

represented in Figure 6.21b. The center of mass was calculated considering a frequency range between 480 and 560  $\text{cm}^{-1}$ . Thus, as confirmed by Raman spectra of Figure 6.21b, variations of the center of mass can be correlated to the frequency shift suffered by the first order Si Raman peak. The first order Raman line of s1, s2 and s3 Raman spectra is centered at 520.8, 519.3 and 518.7  $\text{cm}^{-1}$ , respectively. Notice that the center of mass values represented by the color scale bar of Figure 6.21a are shifted towards higher frequencies respect the Raman peak position values mentioned above. This is induced by the contribution of the Fano resonance which moves the center of mass towards higher energies respect the peak maximum. As it can be seen, the Raman peak position suffers a blue shift of about 2  $\text{cm}^{-1}$  at the border of the contact. Interestingly, areas of the contact that show such a blue shift exactly match with areas of the 1.43 W LFC that evidence higher levels of doping (see Figure 6.15f). It has been reported, that Raman spectra obtained from samples with doping levels above  $5 \times 10^{18} \text{ cm}^{-3}$  not only exhibit the so-called Fano resonance, but also show a blue shift in the Raman peak maximum [68]. The expected theoretical peak shift induced by an increase in doping satisfies:

$$w = w_0 + \frac{\Delta\Gamma}{2q_F} \quad (6.5)$$

where  $w_0$  is the peak position of the bulk un-doped and stress free c-Si and  $\Delta\Gamma$  is the change in the Raman peak width due to doping. The expected theoretical

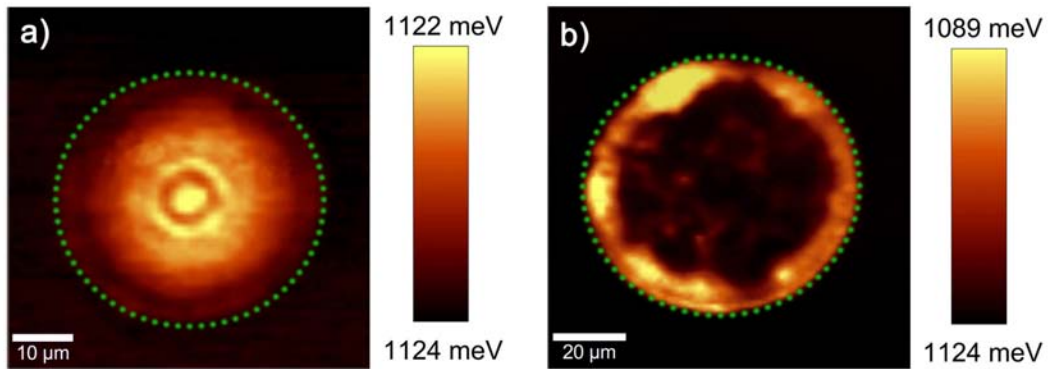
### 6.3. Doping profiles in laser-fired contacts

peak shift resulting from Equation (6.5) for a  $q_F$  parameter of 16 correlated to a 1.43 W LFC (see Table 6.3) takes values of about  $0.5 \text{ cm}^{-1}$ . This theoretical value is significantly lower than that observed in Figure 6.21, i.e. about  $2 \text{ cm}^{-1}$ . This fact suggests that in addition to the blue shift induced by an increase of the doping level, a second contribution in the Raman shift is also present. We correlate this second contribution to stress possibly induced by the laser process. LFCs processed at 0.98 and 1.1 W do not show any significant blue shift in the first order Raman peak maximum. Thus, the level of laser power used to process the LFCs probably plays an important role in the level of stress induced by the laser process.

#### 6.3.3 Doping profiles studied by micro-PL

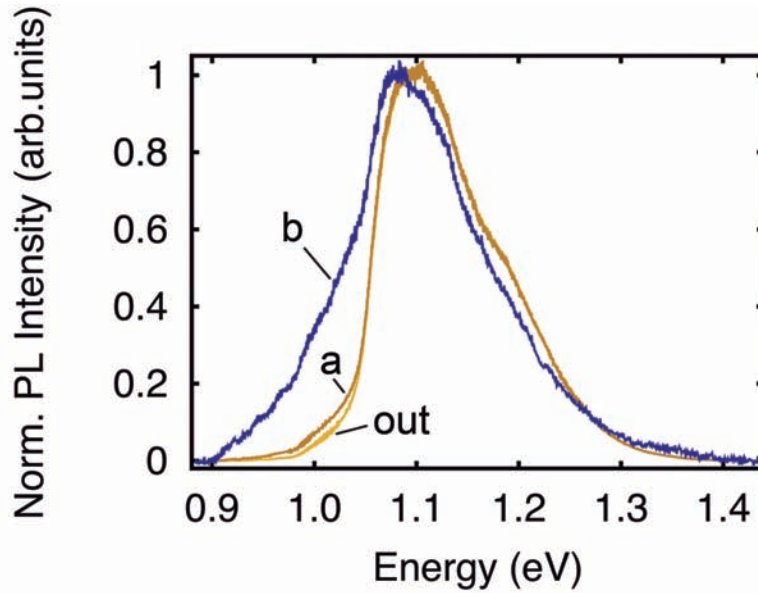
Band-to-band photoluminescence (PL) spectroscopy senses the radiative recombination between photo-generated electrons in the conduction band (CB) and the corresponding holes in the valence band (VB) (see Section 3.1). As an increase in doping density induces a reduction of the energy gap between CB and VB, PL has been proven as a reliable tool for monitoring the band-gap shift in heavily doped c-Si [127]. In this sense, micro-PL spectroscopy is also able to characterize the high doping levels expected inside the LFCs. For this purpose, we have studied the position and line shape of the PL emission line by monitoring the center of mass of the PL spectra recorded inside the LFCs.

Figure 6.22 shows the PL center of mass maps corresponding to the LFCs processed at 0.98 W (a) and 1.43 W (b). The averaged PL spectra obtained from



**Figure 6.22:** PL center of mass maps of LFCs processed at 0.98 W (a) and 1.43 W (b). The green dotted circles delimit the physical dimensions of the LFCs.

the brighter zones of the PL maps are illustrated in Figure 6.23. As it can be seen, the shift of the PL spectra center of mass revealed by the color scale bars of Figure 6.22 is linked to an increase of the PL intensity at lower energies. In particular, the PL spectrum related to the 0.98 W LFC evidences a slight increase of the left PL spectrum shoulder, whereas the PL spectrum related to the 1.43 W LFC shows a significantly higher increase of the left PL spectrum shoulder plus a blue shift in the PL emission maximum. We correlate this shift of the PL line to a Si band-gap renormalization induced by a strong increase of doping in the measured material volume.



**Figure 6.23:** Averaged PL spectra corresponding to the highly-doped regions, i.e. yellow colored regions, of PL center of mass maps a and b shown in Figure 6.22. Additionally, a PL spectra recorded out of the processed LFC regions is also represented.

The increase in doping is further confirmed by a strong reduction in PL intensity for the 1.43 W LFC respect the PL intensity of the 0.98 W LFC. In particular, PL intensity goes from 16700 counts for the 0.98 W to 945 counts for the LFC processed at 1.43 W (the PL intensity associated to a non-processed surface point is 43000 counts). The decrease in PL for the highly-doped areas is explained by the increase of the non-radiative recombination induced by the high density of doping impurities. The low PL intensity associated to the 1.43 W LFC is qualitatively observed in Figure 6.23 from the higher noise-to-signal

### 6.3. Doping profiles in laser-fired contacts

ratio of the 1.43 W normalized PL spectrum.

Interestingly, the two represented PL maps greatly correlate with the homologous Raman peak FWHM maps of Figure 6.15. For all these reasons, we confirm that the brighter zones of the PL maps of Figure 6.22 have associated a higher doping level. We consider these results a clear proof that both micro-Raman and micro-PL spectroscopies show an excellent sensitivity and reproducibility for studying doping-density variations above  $1 \times 10^{18} \text{ cm}^{-3}$ . This fact together with the high lateral resolution (down to  $1 \mu\text{m}$ ) achieved by our micro-configuration setup makes these techniques suitable for monitoring doping variations at such high spatial resolutions.

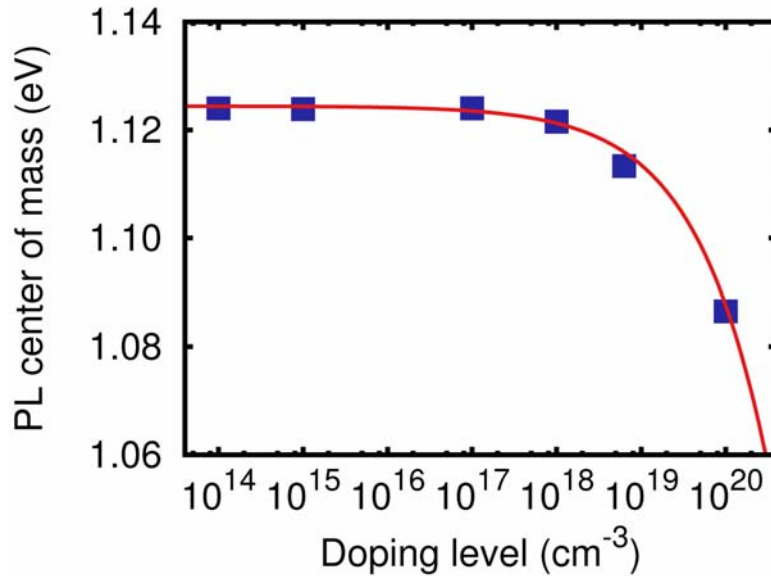


**Figure 6.24:** Dependence between doping density and center of mass of the PL spectra. Data points were obtained from the reference calibration wafers showing different doping. The obtained fit has been used to quantify the doping level corresponding to the highly doped regions of the PL center of mass maps represented in Figure 6.22.

In order to quantify the doping level from the PL data and to compare it with values obtained from the Raman data, we have obtained a calibration curve that represents the center of mass position of the PL emission line against the doping level. The calibration curve, that is represented in Figure 6.24, has been obtained from the calibration wafers showing different doping levels. As it can be observed, for low doping levels ( $< 1 \times 10^{17} \text{ cm}^{-3}$ ) the center of mass of

the PL spectra shows a constant value of about 1.125 meV. In contrast, for doping densities above around  $1 \times 10^{18} \text{ cm}^{-3}$ , the center of mass decreases steadily in energy. Data points fit well to a power function of the form:  $a x^b + c$ . From the fit equation we have been able to estimate the doping level associated to the brighter zones, i.e. zones with a higher doping level, of the two PL maps of Figure 6.22. For the highly-doped region of the LFC processed at 0.98 W, we obtain a doping density of about  $1.43 \times 10^{18} \text{ cm}^{-3}$ , whereas for the highly-doped area of the LFC processed at 1.43 W we obtain a doping level of  $4.9 \times 10^{19} \text{ cm}^{-3}$ . In the case of the 0.98 W LFC, the higher error expected from the small shift of the PL spectrum leads to a slightly lower doping value respect the one deduced from Raman data, i.e.  $4.6\text{-}5.7 \times 10^{18} \text{ cm}^{-3}$ . In contrast, for the 1.43 W LFC where the change in the PL spectrum are substantially larger, the estimated doping density agrees well with the doping level calculated from Raman measurements.

### 6.3.4 LFCs characterized by C-AFM measurements

Finally, the study of LFCs was completed by their characterization by means of c-AFM measurements. The aim of these studies is to analyze if the laser-processed material volume shows preferential conductive zones, and if that is the case, to study their correlation with the highly-doped regions deduced from Raman and PL data. C-AFM measurements have been divided in two groups. First, we have performed electrical maps of complete LFCs with the intention to qualitatively evidence differences in terms of electrical conductivity. In addition to the electrical maps, I-V measurements were also performed. These measurements were done in static mode at various locations onto the LFCs. In order to minimize the well-known light scattering effects from the AFM laser, which can induce local photoconductivity [128], the laser was turned-off for a brief moment before the I-V acquisition.

Representative c-AFM results obtained from a LFC processed at 1.43 W are shown in Figure 6.25a. The upper part of the image shows the topography map, whereas the lower part of the panel corresponds to the local resistance map recorded while applying a voltage of +2 V. In the latter, the darker zones indicate the areas with a low local resistance, i.e. high conductivity. In particular, the border of the contact shows the highest electrical conductivities which decrease as you move to the center of the contact. The highest local resistance was evidenced in outer region of the LFC (region that has not

### 6.3. Doping profiles in laser-fired contacts

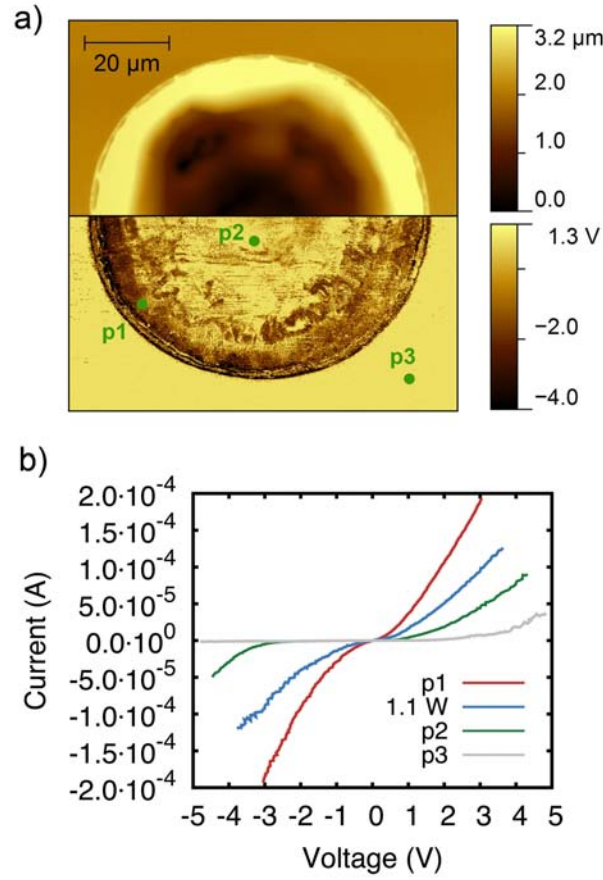


**Figure 6.25:** Topography (upper half) and local resistance (lower half) maps of a LFC processed at 1.43 W (a). The I-V characteristics of the selected points t1, t2 and t3 are represented (b). Additionally, an I-V curve (in blue) corresponding to a highly-conductive area in a LFC processed at 1.1 W is also shown.

been processed). C-AFM data is in great agreement with Raman and PL data showed in the first part of the work, where highly-doped regions of the contact processed at 1.43 W were detected at the border of the contact (see Figures 6.15f and 6.22b).

The I-V curves corresponding to the three points (p1, p2 and p3) depicted in the local resistance map of Figure 6.25a are represented in Figure 6.25b. The curves have been calculated from an average of at least 20 curves per point. Figure 6.26 illustrates a sketch of the C-AFM measurements on the hypothetical cross-section of a 1.43 W LFC as deduced from Raman and PL data. The right hand side of the sketch also represents an equivalent electrical circuit of such C-AFM measurements. Since the resistance assigned to the tip contact



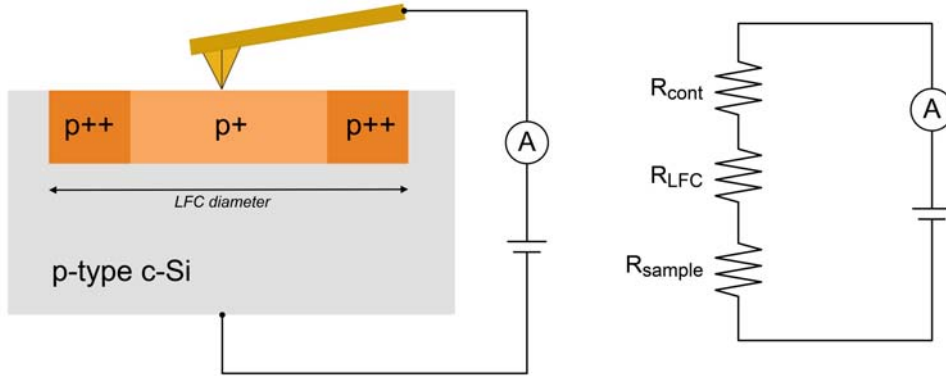


**Figure 6.26:** Sketch illustrating the experimental setup of C-AFM measurements. The hypothetic highly-doped regions of an 1.43 W LFC as deduced from Raman and PL data are indicated. The equivalent circuit of the C-AFM setup is also shown.

( $R_{\text{cont}}$ ) (which depends on the tip contact force), and the resistance associated to the sample ( $R_{\text{sample}}$ ) can be considered constant during measurements, the resulting C-AFM signal will mainly depend on the resistance linked to the LFCs ( $R_{\text{LFC}}$ ). As expected from the resistivity map, the curve recorded at point p1 is the one that shows a higher conductivity. It also shows a good linearity evidencing an ohmic contact behavior between the diamond tip and the sample. In contrast, the I-V curve recorded at point p2 (central part of the contact) evidences lower conductivity than that obtained at point p1. In addition, p2 curve shows a rectifying behavior. This can be explained by a higher potential barrier between the diamond tip and the less doped Si region. Of course, this scenario is even more evident for the I-V curve measured on the unprocessed region (p3). The potential barrier between the diamond tip and the non-processed surface (with a related doping density of about  $5 \times 10^{15} \text{ cm}^{-3}$ ) enlarges, creating a schottky-like contact. In order to strengthen the consistency of the measurements, another I-V curve obtained onto the highly-doped region of a contact processed at 1.1 W is also shown. As it was expected, the I-V curve shows a lower conductivity than the curve related to the LFC processed at 1.43 W. Again, the symmetry of the curve confirms the ohmic-like behavior of the contact between the tip and the highly-doped sample region.



## 6.4 Chapter summary

In the first part of this chapter, we took advantage of the high spatial resolution and the passivation-quality-sensitivity capabilities of micro-PL spectroscopy in order to study the effect of laser firing process on the efficiency of the passivation layer around the contacts. A reduction of the passivation performance has been observed up to a distance of 100  $\mu\text{m}$  from the contact border correlated to the laser power. The use of UV lasers for LFC processing was observed to produce a higher impact on the passivation layer. In contrast, the deposition of a  $\text{SiC}_x$  capping layer was observed to minimize the impact of the laser processing on the passivation layer. The impact of the laser processing around the LFCs was also confirmed by monitoring the effective surface recombination velocities ( $S_{\text{eff}}$ ) in laser processed surfaces showing different pitch values. In particular, we have observed that for short values of pitch,  $S_{\text{eff}}$  resulted in higher values than those predicted by conventional models which only consider the recombination velocity at the contacts and the recombination velocity at the non-processed surface.

In the second part of the chapter, we presented results concerning the doping profiles in LFCs processed between 0.98 and 1.43 W in  $\text{Al}_2\text{O}_3$ -passivated p-type c-Si wafers, studied by means of micro-Raman and micro-PL spectroscopy. The laser power used to process the LFCs was found to play an important role in the distribution of the highly-doped regions. At powers around 0.98 W, the highly-doped regions that reach doping levels of about  $5 \times 10^{18} \text{ cm}^{-3}$  are preferentially located at the center of the LFCs. In contrast, for higher laser power values, the level of doping increases (doping densities of around  $5 \times 10^{19} \text{ cm}^{-3}$  were observed for contacts processed at 1.43 W), and the location of the highly-doped regions moves towards the border of the contacts. An important result is the observation of microcrystalline-like features in the Raman spectra recorded at specific points inside the LFCs, which suggests that the locally melted Si fraction solidify in microcrystalline manner. Highly-doped regions revealed by Raman measurements have been further confirmed by micro-PL spectroscopy. Regions with a higher doping density evidenced a blue shift of the PL emission line, which we correlate to the Si band-gap renormalization induced by the strong increase in doping. Finally, both Raman and PL data were further confirmed by local I-V curves recorded through conductive-AFM. I-V characteristics obtained on highly-doped areas feature an ohmic-like behavior, whereas I-V curves recorded at regions non-processed by laser, i.e. regions

with lower doping level, revealed a schottky-like behavior.

# 7

## Conclusions and future work

In this Thesis, we have investigated the applicability of different high-resolution experimental techniques for the comprehensive study and characterization of various PV systems and devices. The techniques used are: Kelvin Probe Force Microscopy (KPFM), Atomic Force Microscopy (AFM), conductive-AFM, micro-Raman spectroscopy, and micro-photoluminescence (PL), among others. Mainly, the experiments were applied to study the rear passivation layer, and rear local base contacts of p-type c-Si solar cells.

### 7.1 Conclusions

#### 7.1.1 Kelvin Probe Force Microscopy

KPFM technique was successfully applied for the study of potential profiles across Al/SiO<sub>2</sub>/c-Si Metal-Oxide-Semiconductor (MOS) junctions.

- This technique was demonstrated to be able to characterize important MOS features such as the semiconductor band bending at the MOS junction, as well as the amount of charge associated to the oxide layer. Hence, the obtained results demonstrate the potential of this technique in order to characterize MOS junctions with spatial resolution at the nanoscale.

- We presented a suitable measurement procedure to carry out these type of measurements. One of the most important requirements is the proper cleavage of the MOS junction.

### 7.1.2 Low-temperature micro-PL

Low-temperature micro-PL was applied for the study of  $\text{Al}_2\text{O}_3$ -passivated c-Si wafers.

- Unexpectedly, we identified the formation of the so-called Electron-Hole Liquid (EHL), despite the use of low optical pumping for which the condensed phase is not typically observed. The elevated focalization linked to the use of a micro-setup configuration, favored the formation of the condensed phase. Thus, we found an easy way to observe EHL condensation without the necessity to use elevated optical pumping.
- We found that the EHL PL intensity is correlated to the net electric field at the  $\text{Al}_2\text{O}_3$ /c-Si interface. This finding opens the possibility to use this approach to monitor local variations in the surface and sub-surface interface properties.

### 7.1.3 Micro-PL for the study of LFCs

Micro-PL spectroscopy was successfully applied to study for the first time, the impact of the laser processing at the surrounding regions of LFCs.

- A reduction of the passivation quality, was observed up to a distance of 100  $\mu\text{m}$  from the contact border correlated to the laser power. This observation demonstrates the significant effect of laser processing approaches on the passivation layer.
- The quantification of the local reduction in PL intensity was used to semi-quantify the impact on the passivation performance of the laser processing. This method was used to compare and study different LFC processing parameters and different passivation systems. Hence, it represents an important tool to optimize the processing parameters of LFC approach that induce a lower damage to the passivation layer.
- The use of UV lasers for LFC processing has been observed to produce a higher impact on the passivation layer. In contrast, the deposition of a

## 7.2. Future work

---

SiC<sub>x</sub> capping layer has been observed to minimize the impact of the laser processing on the passivation layer.

- Conventional analytical models that not consider the observed affected data around the LFCs, were observed to result in overestimated values of effective surface recombination velocity at the processed surface. Since the contribution of the affected area is proportionally higher for lower pitches, such overestimation is higher for lower values of pitch. In this sense, 3D models that include the observed reduction of passivation around the contacts would be necessary to correctly predict the surface recombination velocity at the laser-processed surfaces.

### 7.1.4 Micro-Raman for the study of LFCs

Micro-Raman was successfully applied to study the doping level as well as the distribution of the highly-doped region formed below the LFCs.

- This is the first time that such a study is carried out, and represents an important tool to optimize the LFC approach in terms of the highly-doped region features.
- The laser power used to process the LFCs was found to play an important role in the distribution of the highly-doped regions. With our processing parameters, for lower laser powers (around 1 W), the highly-doped regions are preferentially located at the center of the LFCs. In contrast, for higher laser power values up to 1.4 W, the location of the highly-doped regions moves towards the border of the contacts.
- Other important insight about the LFCs formation was the observation of microcrystalline-like features in the Raman spectra recorded inside the LFCs. This suggests that the locally melted Si fraction solidify in microcrystalline manner.

## 7.2 Future work

The experimental techniques used in this Thesis were demonstrated to be versatile tools for studying different parts and features of current PV devices. As we will see, a clear example of this versatility is demonstrated by the study presented in the appendix of this work. In this appendix, AFM and micro-Raman

spectroscopy are applied to study the molecular distribution across organic thin films for Organic Photovoltaics (OPV) and Organic Light Emitting Diode (OLED) applications. This study demonstrates that high-resolution techniques can be applied for an enormous number of different purposes and studies.

In terms of c-Si-based PV devices, some possible studies are described in the following lines:

- Cross-sectional KPFM measurements could be applied for studying potential profiles across different junctions of solar cell devices. For a proper application of the method, an appropriate previous step would be to develop new KPFM measurements to further investigate those specific features we did not understand in the results obtained in Chapter 4. For instance, the non-saturation of surface potential signal above threshold voltage.
- It would be interesting to take advantage of the PL profiles recorded across LFCs in order to improve conventional analytical models that are used to predict the surface recombination velocity of surfaces processed by laser. Since obtained micro-PL profiles showed an exponential decay across the affected-area, an interesting approximation would be to develop a 3D model that would consider an exponential transition between the surface recombination velocity of the non-affected surface and the surface recombination velocity at the contacts.
- Another interesting study would be the application of micro-Raman spectroscopy for the study of selective emitters. Selective emitters are considered a promising concept to further develop technologically feasible high-efficiency c-Si solar cells. The doping-sensitivity capabilities of micro-Raman spectroscopy make this technique a suitable tool to obtain relevant information about the features of the highly-doped regions of selective emitters.

# Bibliography

- [1] R. Heede, "Tracing anthropogenic carbon dioxide and methane emissions to fossil fuel and cement producers, 1854-2010," *Climate Change*, vol. 122, pp. 229–241, 2014.
- [2] S. Anwar, H. Efstathiadis, and S. Qazi, eds., *Handbook of research on solar energy systems and technologies*. IGI Global, 2013. (p. 169).
- [3] "Solar photovoltaic energy. Technology roadmap," tech. rep., International Energy Agency (IEA), 2014.
- [4] M. A. Green, "The path to 25% silicon solar cell efficiency: History of silicon cell evolution," *Progress in Photovoltaics: Research and Applications*, vol. 17, pp. 183–189, 2009.
- [5] T. Tiedje, E. Yablonovitch, G. D. Cody, and B. G. Brooks, "Limiting efficiency of silicon solar cells," *IEEE Transactions on Electron Devices*, vol. ED-31, pp. 711–716, 1984.
- [6] S. W. Glunz, R. Preu, and D. Biro, "Crystalline silicon solar cells. State-of-the-art and future developments," *Comprehensive Renewable Energy*, vol. 1 (Book Chapter 1.16), pp. 1–62, 2012.
- [7] S. W. Glunz, "Crystalline silicon solar cells with high efficiency," *Advanced Concepts in Photovoltaics (RSC Energy and Environment Book Series)*, vol. 1 (Book Chapter), pp. 1–29, 2014.
- [8] J. Mandelkorn and J. H. Lamneck, "A new electric field effect in silicon solar cells," *Journal of Applied Physics*, vol. 44, pp. 4785–4787, 1973.
- [9] A. G. Aberle, "Surface passivation of crystalline silicon solar cells: A review," *Progress in Photovoltaics: Research and Applications*, vol. 8, pp. 473–487, 2000.

- 
- [10] A. W. Blakers, A. Wang, A. M. Milne, J. Zhao, and M. A. Green, "22.8% efficient silicon solar cell," *Applied Physics Letters*, vol. 55, pp. 1363–1365, 1989.
- [11] Z. Wang, P. Han, H. Lu, H. Qian, L. Chen, Q. Meng, N. Tang, F. Gao, Y. Jiang, J. Wu, W. Wu, H. Zhu, J. Ji, Z. Shi, A. Sugianto, L. Mai, B. Hallam, and S. Wenham, "Advanced PERC and PERL production cells with 20.3% record efficiency for standard commercial p-type silicon wafers," *Progress in Photovoltaics: Research and Applications*, vol. 20, pp. 260–268, 2012.
- [12] M. A. Green, J. Zhao, A. Wang, and S. R. Wenham, "Progress and outlook for high-efficiency crystalline silicon solar cells," *Solar Energy Materials and Solar Cells*, vol. 65, pp. 9–16, 2001.
- [13] S. R. Wenham, J. Zhao, X. Dai, A. Wang, and M. A. Green, "Surface passivation in high efficiency silicon solar cells," *Solar Energy Materials and Solar Cells*, vol. 65, pp. 377–384, 2001.
- [14] H. Schlangenotto, H. Maeder, and Gerlach, "Temperature dependence of the radiative recombination coefficient in silicon," *Physica Status Solidi A*, vol. 21, p. 357, 1974.
- [15] T. Trupke, M. A. Green, P. Würfel, P. P. Altermatt, A. Wang, J. Zhao, and R. Corkish, "Temperature dependence of radiative recombination coefficient of intrinsic crystalline silicon," *Journal of Applied Physics*, vol. 94, pp. 4930–4937, 2003.
- [16] A. Hangleiter and R. Hacker, "Enhancement of band-to-band Auger recombination by electron-hole correlations," *Physical Review Letters*, vol. 65, p. 215, 1990.
- [17] M. S. Tyagi and R. van Overstraeten, "Minority carrier recombination in heavily-doped silicon," *Solid-State Electronics*, vol. 26, p. 577, 1983.
- [18] W. Shockley and W. T. Read, "Statistics of the recombination of holes and electrons," *Physical Review*, vol. 87, p. 935, 1952.
- [19] R. N. Hall, "Electron-hole recombination in germanium," *Physical Review*, vol. 87, p. 387, 1952.



## Bibliography

---

- [20] D. Schroder, *Semiconductor material and device characterization*. John Wiley & Sons Inc., 2006. p. 393.
- [21] G. Dingemans and E. Kessels, "Status and prospects of  $\text{Al}_2\text{O}_3$ -based surface passivation schemes for silicon solar cells," *Journal of Vacuum Science and Technology A: Vacuum, Surfaces and Films*, vol. 30, p. 040802, 2012.
- [22] M. L. Reed and J. D. Plummer, "Chemistry of Si-SiO<sub>2</sub> interface trap annealing," *Journal of Applied Physics*, vol. 63, pp. 5776–5793, 1988.
- [23] M. J. Kerr and A. Cuevas, "Very low bulk and surface recombination in oxidized silicon wafers," *Semiconductor Science and Technology*, vol. 17, pp. 35–38, 2002.
- [24] N. M. Nursam, Y. Ren, and K. J. Weber, "PECVD silicon nitride passivation on boron emitter: The analysis of electrostatic charge on the interface properties," *Advances in Optoelectronics*, vol. 2010, pp. 1–9, 2010.
- [25] A. J. M. van Erven, R. C. M. Bosch, and M. D. Bijker, "Textured silicon surface passivation by high-rate expanding thermal plasma deposited SiN and thermal SiO<sub>2</sub>/SiN stacks for crystalline silicon solar cells," *Progress in Photovoltaics: Research and Applications*, vol. 16, pp. 615–627, 2008.
- [26] P. Saint-Cast, D. Kania, M. Hofmann, J. Benick, J. Rentsch, and R. Preu, "Very low surface recombination velocity on p-type c-Si by high-rate plasma-deposited aluminum oxide," *Applied Physics Letters*, vol. 95, p. 151502, 2009.
- [27] J. Schmidt, A. Merkle, R. Brendel, B. Hoex, M. C. M. van de Sanden, and W. M. M. Kessels, "Surface passivation of high-efficiency silicon solar cells by atomic-layer-deposited  $\text{Al}_2\text{O}_3$ ," *Progress in Photovoltaics: Research and Applications*, vol. 16, pp. 461–466, 2008.
- [28] B. Hoex, J. J. H. Gielis, M. C. M. van de Sanden, and W. M. M. Kessels, "On the c-Si surface passivation mechanism by the negative-charge-dielectric  $\text{Al}_2\text{O}_3$ ," *Journal of Applied Physics*, vol. 104, p. 113703, 2008.
- [29] B. Hoex, J. Schmidt, P. Pohl, M. C. M. van de Sanden, and W. M. M. Kessels, "Silicon surface passivation by atomic layer deposited  $\text{Al}_2\text{O}_3$ ," *Journal of Applied Physics*, vol. 104, p. 044903, 2008.

- 
- [30] F. Werner, B. Veith, V. Tiba, P. Poodt, F. Roozeboom, R. Brendel, and J. Schmidt, "Very low surface recombination velocities on p- and n-type c-Si by ultrafast spatial atomic layer deposition of aluminum oxide," *Applied Physics Letters*, vol. 97, p. 162103, 2010.
- [31] R. Hezel and K. Jaeger, "Low-temperature surface passivation of silicon solar cells," *Journal of the Electrochemical Society*, vol. 136, pp. 518–523, 1989.
- [32] B. Hoex, S. B. S. Heil, E. Langereis, M. C. M. van de Sanden, and W. M. M. Kessels, "Ultralow surface recombination of c-Si substrates passivated by plasma-assisted atomic layer deposited  $\text{Al}_2\text{O}_3$ ," *Applied Physics Letters*, vol. 89, p. 042112, 2006.
- [33] G. Agostinelli, A. Delabie, P. Vitanov, Z. Alexieva, H. F. W. Dekkers, S. De Wolf, and G. Beaucarne, "Very low surface recombination velocities on p-type silicon wafers passivated with a dielectric with fixed negative charge," *Solar Energy Materials and Solar Cells*, vol. 90, pp. 3438–3443, 2006.
- [34] J. Robertson, "Interfaces and defects of high-k oxides on silicon," *Solid-State Electronics*, vol. 49, pp. 283–293, 2005.
- [35] J. R. Weber, A. Janotti, and C. Van De Walle, "Native defects in  $\text{Al}_2\text{O}_3$  and their impact on iii-v/ $\text{Al}_2\text{O}_3$  metal-oxide-semiconductor-based devices," *Journal of Applied Physics*, vol. 109, p. 033715, 2011.
- [36] D. Liu, S. J. Clark, and J. Robertson, "Oxygen vacancy levels and electron transport in  $\text{Al}_2\text{O}_3$ ," *Applied Physics Letters*, vol. 96, p. 032905, 2010.
- [37] G. Dingemans, R. Seguin, P. Engelhart, M. C. M. van de Sanden, and W. M. M. Kessels, "Silicon surface passivation by ultrathin  $\text{Al}_2\text{O}_3$  films synthesized by thermal and plasma atomic layer deposition," *Physica Status Solidi RRL*, vol. 4, pp. 10–12, 2010.
- [38] G. Dingemans, A. Clark, J. A. van Delft, M. C. M. van de Sanden, and W. M. M. Kessels, " $\text{Er}^{3+}$  and Si luminescence of atomic layer deposited Er-doped  $\text{Al}_2\text{O}_3$  thin films on Si(100)," *Journal of Applied Physics*, vol. 109, p. 113107, 2011.

- [39] F. Werner, B. Veith, D. Zielke, L. Kühnemund, C. Tegenkamp, M. Seibt, R. Brendel, and J. Schmidt, "Electronic and chemical properties of the c-Si/ $\text{Al}_2\text{O}_3$  interface," *Journal of Applied Physics*, vol. 109, p. 113701, 2011.
- [40] G. Dingemans, N. M. Terlinden, D. Pierreux, H. B. Profijt, M. C. M. van de Sanden, and W. M. M. Kessels, "Influence of the oxidant on the chemical and field-effect passivation of Si by ALD  $\text{Al}_2\text{O}_3$ ," *Electrochemical and Solid-State Letters*, vol. 14, no. 1, pp. H1–H4, 2011.
- [41] J. Benick, A. Richter, T.-T. A. Li, N. E. Grant, K. R. McIntosh, Y. Ren, K. J. Weber, M. Hermle, and S. W. Glunz, "Effect of a post-deposition anneal on  $\text{Al}_2\text{O}_3$ /Si interface properties," *Proceedings of the 35th IEEE Photovoltaic Specialists Conference*, pp. 891–896, 2010.
- [42] A. Stesmans and V. V. Afanas'ev, "Si dangling-bond-type defects at the interface of (100)Si with ultrathin layers of  $\text{SiO}_x$ ,  $\text{Al}_2\text{O}_3$ , and  $\text{ZrO}_2$ ," *Applied Physics Letters*, vol. 80, pp. 1957–1959, 2002.
- [43] G. Dingemans, W. Beyer, M. C. M. van de Sanden, and W. M. M. Kessels, "Hydrogen induced passivation of Si interfaces by  $\text{Al}_2\text{O}_3$  films and  $\text{SiO}_2$ / $\text{Al}_2\text{O}_3$  stacks," *Applied Physics Letters*, vol. 97, p. 152106, 2010.
- [44] G. Dingemans, F. Einsele, W. Beyer, M. C. M. van de Sanden, and W. M. M. Kessels, "Influence of annealing and  $\text{Al}_2\text{O}_3$  properties on the hydrogen-induced passivation of the Si/ $\text{SiO}_2$  interface," *Journal of Applied Physics*, vol. 111, p. 093713, 2012.
- [45] E. Schneiderlöchner, R. Preu, R. Lüdemann, and S. W. Glunz, "Laser-fired rear contacts for crystalline silicon solar cells," *Progress in Photovoltaics: Research and Applications*, vol. 10, pp. 29–34, 2002.
- [46] D. Kray and S. Glunz, "Investigation of laser-fired rear-side recombination properties using an analytical model," *Progress in Photovoltaics: Research and Applications*, vol. 14, pp. 195–201, 2006.
- [47] M. M. Hilali, J. M. Gee, and P. Hacke, "Bow in screen-printed back-contact industrial silicon solar cells," *Solar Energy Materials and Solar Cells*, vol. 91, pp. 1228–1233, 2007.
- [48] P. Ortega, A. Orpella, I. Martin, M. Colina, G. Lopez, C. Voz, M. I. Sanchez, C. Molpeceres, and R. Alcubilla, "Laser-fired contact optimiza-

- tion in c-Si solar cells," *Progress in Photovoltaics: Research and Applications*, vol. 20, pp. 173–180, 2012.
- [49] M. Moors, K. Baert, T. Caremans, F. Duerinckx, A. Cacciato, and J. Szlufcik, "Industrial PERL-type solar cells exceeding 19% with screen-printed contacts and homogeneous emitter," *Solar Energy Materials and Solar Cells*, vol. 106, pp. 84–88, 2012.
- [50] S. Glunz, A. Grobe, M. Hermle, M. Hofmann, S. Janz, T. Roth, O. Schultz, M. Vetter, I. Martin, R. Ferre, S. Bermejo, W. Wolke, W. Warta, and R. Willeke, "Comparison of different dielectric passivation layers for application in industrially feasible high-efficiency crystalline silicon solar cells," *Proceedings of the 20th EUPVSEC*, pp. 572–577, 2005.
- [51] P. Ortega, I. Martin, G. Lopez, M. Colina, A. Orpella, C. Voz, and R. Alcubilla, "P-type c-Si solar cells based on rear side laser processing of  $\text{Al}_2\text{O}_3/\text{SiC}_x$  stacks," *Solar Energy Materials and Solar Cells*, vol. 106, pp. 80–83, 2012.
- [52] Z. Hameiri, L. Mai, A. Sproul, and S. R. Wenham, "18.7% efficient laser-doped solar cell on p-type Czochralski silicon," *Applied Physics Letters*, vol. 97, p. 222111, 2010.
- [53] B. Fischer, *Loss analysis of crystalline silicon solar cells using photoconductance and quantum efficiency measurements*. PhD thesis, Universitat Konstanz, 2003.
- [54] T. Trupke, R. A. Bardos, and M. D. Abbott, "Self-consistent calibration of photoluminescence and photoconductance lifetime measurements," *Applied Physics Letters*, vol. 87, p. 184102, 2005.
- [55] S. Herlufsen, J. Schmidt, D. Hinken, K. Bothe, and R. Brendel, "Photoconductance-calibrated photoluminescence lifetime imaging of crystalline silicon," *Physica Status Solidi RRL*, vol. 2, pp. 245–247, 2008.
- [56] P. Gundel, M. C. Schubert, F. D. Heinz, R. Woehl, J. Benick, J. A. Giesecke, D. Suwito, and W. Warta, "Micro-spectroscopy on silicon wafers and solar cells," *Nanoscale Research Letters*, vol. 6, pp. X1–8, 2011.
- [57] P. Gundel, M. C. Schubert, W. Kwapil, J. Schoen, M. Reiche, H. Savin, M. Yli-Koski, J. A. Sans, G. Martinez-Criado, W. Seifert, W. Warta, and

- E. R. Weber, "Micro-photoluminescence spectroscopy on metal precipitates in silicon," *Physica Status Solidi RRL*, vol. 3, pp. 230–232, 2009.
- [58] P. Gundel, F. D. Heinz, M. C. Schubert, J. A. Giesecke, and W. Warta, "Quantitative carrier lifetime measurement with micron resolution," *Journal of Applied Physics*, vol. 108, p. 033705, 2010.
- [59] M. A. Green, "Improved value for the silicon free exciton binding energy," *AIP Advances*, vol. 3, p. 112104, 2013.
- [60] D. Abou-Ras, T. Kirchartz, and U. Rau, *Advanced characterization techniques for thin film solar cells*. Wiley-VCH, 2011.
- [61] C. V. Raman, "A new radiation," *Indian Journal of Physics*, vol. 2, pp. 387–398, 1928.
- [62] J. P. Russell, "Raman scattering in silicon," *Applied Physics Letters*, vol. 6, pp. 223–224, 1965.
- [63] J. H. Parker, J. D. Feldman, and M. Ashkin, "Raman scattering by silicon and germanium," *Physical Review*, vol. 155, pp. 712–714, 1967.
- [64] T. R. Hart, R. L. Aggarwal, and B. Lax, "Temperature dependence of Raman scattering in silicon," *Physical Review B*, vol. 1, pp. 638–642, 1970.
- [65] W. S. Yoo, J. H. Kim, and S. M. Han, "Multiwavelength Raman characterization of silicon stress near through-silicon vias and its inline monitoring applications," *Journal of Micro/Nanolithography, MEMS, and MOEMS*, vol. 13, p. 011205, 2014.
- [66] L. Gao, N. P. Lu, L. G. Liao, A. L. Ji, and Z. X. Cao, "Nanocrystalline Si:H thin films grown at room temperature with plasma-enhanced chemical vapour deposition at a very high pressure," *Journal of Physics D: Applied Physics*, vol. 45, p. 335104, 2012.
- [67] D. Wei, S. Xiao, S. Huang, C. Chan, H. Zhou, L. Xu, Y. Guo, J. Chai, S. Wang, and S. Xu, "Low-temperature deposition of micro c-Si:H thin films by a low-frequency inductively coupled plasma for photovoltaic applications," *Journal of Physics D: Applied Physics*, vol. 46, p. 215501, 2013.

- 
- [68] R. Agaiby, M. Becker, S. Thapa, U. Urmoneit, A. Berger, A. Gawlik, G. Sarau, and S. Christiansen, "Stress and doping uniformity of laser crystallized amorphous silicon in thin film silicon solar cells," *Journal of Applied Physics*, vol. 107, p. 054312, 2010.
- [69] E. Anastassakis, A. Pinczuk, E. Burstein, F. H. Pollak, and M. Cardona, "Effect of static uniaxial stress on the Raman spectrum of silicon," *Solid State Communications*, vol. 8, pp. 133–138, 1970.
- [70] M. S. Liu, L. A. Bursill, S. Prawer, K. W. Nugent, Y. Z. Tong, and G. Y. Zhang, "Temperature dependence of Raman scattering in single crystal GaN films," *Applied Physics Letters*, vol. 74, pp. 3125–3127, 1999.
- [71] L. Kronik and Y. Shapira, "Surface photovoltage phenomena: Theory, experiment, and applications," *Surface Science Reports*, vol. 37, pp. 1–206, 1999.
- [72] M. Nonnenmacher, M. P. Oboyle, and H. K. Wickramasinghe, "Kelvin probe force microscopy," *Applied Physics Letters*, vol. 58, pp. 2921–2923, 1991.
- [73] K. L. Sorokina and A. L. Tolstikhina, "Atomic force microscopy modified for studying electric properties of thin films and crystals. Review," *Crystallography Reports*, vol. 49, pp. 476–499, 2004.
- [74] V. Palermo, M. Palma, and P. Samori, "Electronic characterization of organic thin films by Kelvin probe force microscopy," *Advanced Materials*, vol. 18, pp. 145–164, 2006.
- [75] G. Benstetter, R. Biberger, and D. Liu, "A review of advanced scanning probe microscope analysis of functional films and semiconductor devices," *Thin Solid Films*, vol. 517, pp. 5100–5105, 2009.
- [76] W. Melitz, J. Shen, A. C. Kummel, and S. Lee, "Kelvin probe force microscopy and its application," *Surface Science Reports*, vol. 66, pp. 1–27, 2011.
- [77] S. J. Cho, S. Dogan, S. Sabuktagin, M. A. Reshchikov, D. K. Johnstone, and H. Morkoc, "Surface band bending in as-grown and plasma-treated n-type GaN films using surface potential electric force microscopy," *Applied Physics Letters*, vol. 84, pp. 3070–3072, 2004.

- [78] G. H. Buh, H. J. Chung, J. H. Yi, I. T. Yoon, and Y. Kuk, "Electrical characterization of an operating Si pn-junction diode with scanning capacitance microscopy and Kelvin probe force microscopy," *Journal of Applied Physics*, vol. 90, pp. 443–448, 2001.
- [79] H. Hoppe, T. Glatzel, M. Niggemann, A. Hinsch, M. C. Lux-Steiner, and N. S. Sariciftci, "Kelvin probe force microscopy study on conjugated polymer/fullerene bulk heterojunction organic solar cells," *Nano Letters*, vol. 5, pp. 269–274, 2005.
- [80] A. Doukkali, S. Ledain, C. Guasch, and J. Bonnet, "Surface potential mapping of biased pn junction with kelvin probe force microscopy: Application to cross-section devices," *Applied Surface Science*, vol. 235, pp. 507–512, 2004.
- [81] T. Glatzel, H. Steigert, S. Sadewasser, R. Klenk, and M. C. Lux-Steiner, "Potential distribution of  $\text{Cu(In,Ga)(S,Se)}_2$ -solar cell cross-sections measured by kelvin probe force microscopy," *Thin Solid Films*, vol. 480-481, pp. 177–182, 2005.
- [82] J. Lee, J. Kong, H. Kim, S.-O. Kang, and K. Lee, "Direct observation of internal potential distributions in a bulk heterojunction solar cell," *Applied Physics Letters*, vol. 99, p. 243301, 2011.
- [83] R. A. Sinton, A. Cuevas, and M. Stuckings, "Quasi-steady-state photoconductance, a new method for solar cell material and device characterization," *Proceedings 25th IEEE Photovoltaic Specialists Conference*, pp. 457–460, 1996.
- [84] R. A. Sinton and A. Cuevas, "Contactless determination of current-voltage characteristics and minority-carrier lifetimes in semiconductors from quasi-steady-state photoconductance data," *Applied Physics Letters*, vol. 69, pp. 2510–2512, 1996.
- [85] C. C. Hu, *Modern semiconductor devices for integrated circuits*. Prentice Hall, Inc., 2010.
- [86] J. A. Dillon Jr. and H. E. Farnsworth, "Work function and sorption properties of silicon crystals," *Journal of Applied Physics*, vol. 29, pp. 1195–1202, 1958.

- 
- [87] Y.-C. Yeo, T.-J. King, and C. Hu, "Metal-dielectric band alignment and its implications for metal gate complementary metal-oxide-semiconductor technology," *Journal of Applied Physics*, vol. 92, pp. 7266–7271, 2002.
- [88] K. Ziegler, "Distinction between donor and acceptor character of surface states in the Si-SiO<sub>2</sub> interface," *Applied Physics Letters*, vol. 32, pp. 249–251, 1978.
- [89] C. D. Jeffries, "Electron hole condensation in semiconductors," *Science*, vol. 189, pp. 955–964, 1975.
- [90] L. V. Keldysh, "The electron-hole liquid in semiconductors," *Contemporary Physics*, vol. 27, pp. 395–428, 1986.
- [91] L. V. Keldysh *Proceedings 9th International Conference on Physics of Semiconductors*, p. 1303, 1968.
- [92] G. A. Thomas, T. G. Phillips, T. M. Rice, and J. C. Hensel, "Temperature-dependent luminescence from the electron-hole liquid in Ge," *Physical Review Letters*, vol. 31, pp. 386–389, 1973.
- [93] P. Vashishta, S. G. Das, and K. S. Singwi, "Thermodynamics of the electron-hole liquid in Ge, Si, and GaAs," *Physical Review Letters*, vol. 33, pp. 911–914, 1974.
- [94] M. A. Tamor and J. P. Wolfe, "Spatial distribution of electron-hole droplets in silicon," *Physical Review B*, vol. 21, pp. 739–742, 1980.
- [95] T. Moriya and T. Kushida, "Luminescence due to metallic electron-hole liquid in GaAs," *Solid State Communications*, vol. 14, pp. 245–248, 1974.
- [96] M. Ganser, M. Seelmann-Eggebert, and R. P. Huebener, "Exciton and electron-hole liquid luminescence of germanium in an electric field," *Physica Status Solidi B*, vol. 111, pp. 131–140, 1982.
- [97] M. A. Vouk and E. C. Lightowers, "Two-phonon assisted free exciton recombination radiation from intrinsic silicon," *Journal of Physics C: Solid State Physics*, vol. 10, pp. 3689–3699, 1977.
- [98] M. Tajima and S. Ibuka, "Luminescence due to electron-hole condensation in silicon-on-insulator," *Journal of Applied Physics*, vol. 84, pp. 2224–2228, 1998.



- [99] Y.-C. Cheng, C.-Y. Sun, E. Sun, and M.-J. Chen, "Enhanced photoluminescence from condensed electron-hole pairs in trench Si," *Journal of Applied Physics*, vol. 108, p. 124305, 2010.
- [100] O. Demichel, F. Oehler, P. Noé, V. Calvo, N. Pauc, P. Gentile, T. Baron, D. Peyrade, and N. Magnea, "Photoluminescence of confined electron-hole plasma in core-shell silicon/silicon oxide nanowires," *Applied Physics Letters*, vol. 93, p. 213104, 2008.
- [101] O. Demichel, V. Calvo, N. Pauc, A. Besson, P. Noé, F. Oehler, P. Gentile, and N. Magnea, "Recombination dynamics of spatially confined electron-hole system in luminescent gold catalyzed silicon nanowires," *Nano Letters*, vol. 9, pp. 2575–2578, 2009.
- [102] N. Pauc, V. Calvo, J. Eymery, F. Fournel, and N. Magnea, "Two-dimensional electron-hole liquid in single Si quantum wells with large electronic and dielectric confinement," *Physical Review Letters*, vol. 92, p. 236802, 2004.
- [103] L. M. Smith and J. P. Wolfe, "Time-resolved study of electron-hole plasmas near the liquid-gas critical point in Si: Evidence for a second condensed phase," *Physical Review B*, vol. 51, pp. 7521–7543, 1995.
- [104] C.-F. Lin, M.-J. Chen, E.-Z. Liang, W. T. Liu, and C. W. Liu, "Reduced temperature dependence of luminescence from silicon due to field-induced carrier confinement," *Applied Physics Letters*, vol. 78, pp. 261–263, 2001.
- [105] J. Shah, M. Combescot, and A. H. Dayem, "Investigation of exciton-plasma mott transition in Si," *Physical Review Letters*, vol. 38, pp. 1497–1500, 1977.
- [106] A. R. Goñi, P. Giudici, F. A. Reboredo, C. R. Proetto, C. Thomsen, K. Eberl, and M. Hauser, "Evidence of spontaneous spin polarization in the two-dimensional electron gas," *Physical Review B*, vol. 70, p. 195331, 2004.
- [107] W. C. Dash and R. Newman, "Intrinsic optical absorption in single-crystal germanium and silicon at 77 K and 300 K," *Physical Review*, vol. 99, pp. 1151–1155, 1955.

- 
- [108] R. B. Hammond, T. C. McGill, and J. W. Mayer, "Temperature dependence of the electron-hole-liquid luminescence in Si," *Physical Review B*, vol. 13, pp. 3566–3575, 1976.
- [109] B. Bergersen, P. Jena, and A. J. Berlinsky, "Electron-hole liquid in heavily doped n-type Ge and Si," *Journal of Physics C: Solid State Physics*, vol. 8, pp. 1377–1386, 1975.
- [110] B. Bergersen, J. A. Rostworowski, M. Eswaran, R. R. Parsons, and P. Jena, "Electron-hole droplets and impurity band states in heavily doped Si(P): Photoluminescence experiments and theory," *Physical Review B*, vol. 14, pp. 1633–1648, 1976.
- [111] B. Liao, R. Stangl, T. Mueller, F. Lin, C. S. Bhatia, and B. Hoex, "The effect of light soaking on crystalline silicon surface passivation by atomic layer deposited  $\text{Al}_2\text{O}_3$ ," *Journal of Applied Physics*, vol. 113, p. 024509, 2013.
- [112] J. J. H. Gielis, B. Hoex, M. C. M. van de Sanden, and W. M. M. Kessels, "Negative charge and charging dynamics in  $\text{Al}_2\text{O}_3$  films on Si characterized by second-harmonic generation," *Journal of Applied Physics*, vol. 104, p. 073701, 2008.
- [113] A. Raghavan, T. A. Palmer, and T. Debroy, "Evolution of laser-fired aluminum-silicon contact geometry in photovoltaic devices," *Journal of Applied Physics*, vol. 111, p. 024903, 2012.
- [114] G. D. Gilliland, "Photoluminescence spectroscopy of crystalline semiconductors," *Materials Science and Engineering Reports*, vol. 18, pp. 99–400, 1997.
- [115] T. Trupke, R. A. Bardos, M. C. Schubert, and W. Warta, "Photoluminescence imaging of silicon wafers," *Applied Physics Letters*, vol. 89, p. 044107, 2006.
- [116] G. López, P. R. Ortega, C. Voz, I. Martín, M. Colina, A. B. Morales, A. Orpella, and R. Alcubilla, "Surface passivation and optical characterization of  $\text{Al}_2\text{O}_3/\text{a-SiC}_x$  stacks on c-Si substrates," *Beilstein Journal of Nanotechnology*, vol. 4, pp. 726–731, 2013.
- [117] V. Magidson and R. Beserman, "Fano-type interference in the Raman spectrum of photoexcited Si," *Physical Review B*, vol. 66, pp. 1952061–1952066, 2002.

- [118] T. Kunz, M. T. Hessmann, S. Seren, B. Meidel, B. Terheiden, and C. J. Brabec, "Dopant mapping in highly p-doped silicon by micro-Raman spectroscopy at various injection levels," *Journal of Applied Physics*, vol. 113, p. 023514, 2013.
- [119] M. Becker, U. Gösele, A. Hofmann, and S. Christiansen, "Highly p-doped regions in silicon solar cells quantitatively analyzed by small angle beveling and micro-Raman spectroscopy," *Journal of Applied Physics*, vol. 106, p. 074515, 2009.
- [120] U. Fano, "Effects of configuration interaction on intensities and phase shifts," *Physical Review*, vol. 124, pp. 1866–1878, 1961.
- [121] F. Cerdeira, T. A. Fjeldly, and M. Cardona, "Effect of free carriers on zone-center vibrational modes in heavily doped p-type Si. ii. optical modes," *Physical Review B*, vol. 8, pp. 4734–4745, 1973.
- [122] F. Cerdeira, T. A. Fjeldly, and M. Cardona, "Raman study of the interaction between localized vibrations and electronic excitations in boron-doped silicon," *Physical Review B*, vol. 9, pp. 4344–4350, 1974.
- [123] M. Chandrasekhar, J. B. Renucci, and M. Cardona, "Effects of interband excitations on Raman phonons in heavily doped n-Si," *Physical Review B*, vol. 17, pp. 1623–1633, 1978.
- [124] S. Veprek, F.-A. Sarott, and Z. Iqbal, "Effect of grain boundaries on the Raman spectra, optical absorption, and elastic light scattering in nanometer-sized crystalline silicon," *Physical Review B*, vol. 36, pp. 3344–3350, 1987.
- [125] Z. Iqbal, S. Veprek, A. P. Webb, and P. Capezzuto, "Raman scattering from small particle size polycrystalline silicon," *Solid State Communications*, vol. 37, pp. 993–996, 1981.
- [126] P. Gundel, M. C. Schubert, F. D. Heinz, J. Benick, I. Zizak, and W. Warta, "Submicron resolution carrier lifetime analysis in silicon with fano resonances," *Physica Status Solidi RRL*, vol. 4, pp. 160–162, 2010.
- [127] J. Wagner, "Band-gap narrowing in heavily doped silicon at 20 and 300 K studied by photoluminescence," *Physical Review B*, vol. 32, pp. 1323–1325, 1985.

- [128] M. Ledinský, A. Fejfar, A. Vetushka, J. Stuchlík, B. Rezek, and J. Kocka, "Local photoconductivity of microcrystalline silicon thin films measured by conductive atomic force microscopy," *Physica Status Solidi RRL*, vol. 5, pp. 373–375, 2011.



## Surface vs bulk phase transitions in organic PV thin films

*AFM and micro-Raman spectroscopy are applied to obtain unique and exclusive information of organic thin films for Organic Light Emitting Diode (OLED) and Organic Photovoltaic (OPV) applications. With this, we intend to demonstrate that such high-resolution experimental techniques not only can be used for the study of Si-based PV devices, but also are versatile tools that can be applied for the study of a wide range of material systems and devices. In this study in particular, we present a novel way to characterize the crystallization transition temperature of a widely studied luminescent polymer such as poly(9,9-dioctylfluorene) (PFO), and the workhorse system for OPV, consisting on poly(3-hexylthiophene) (P3HT) and [6,6]-phenyl C<sub>61</sub>-butyric acid methyl ester (PCBM) blends. The proposed experimental method is based on performing real-time AFM and Raman spectroscopy measurements during heating of organic thin films. In the case of AFM, the crystallization temperature has been studied by monitoring the surface roughness, whereas in the case of micro-Raman, it has been determined by monitoring the C=C Raman peak intensity.*

## A.1 Introduction

Semiconducting polymer thin films and their use in Organic Photovoltaics (OPV) and Organic Light Emitting Diode (OLED) applications have attracted increasing attention during the last two decades due to interesting properties that make them suitable candidates for a broad range of novel application possibilities. Attractive properties like low cost, flexibility, semi-transparency and the possibility to produce devices with very large effective area using the so-called continuous polymeric printing techniques (i.e. roll to roll, ink jet printing) bring to organic materials in a very promising and interesting position into the PV and LED industry [1, 2].

Precisely, from the fabrication point of view, we found one of the most important and relevant differences between inorganic and organic PV materials. The possibility to deposit and obtain OPV thin films from solution leads the opportunity to process devices in a very easy and economic manner respect to inorganic systems. However, certain fundamental and physical differences of organic materials in front of their inorganic counterparts such as a higher exciton binding energy and a lower carrier mobility, lead to the fact that efficiency of organic-based PV systems is still far from that observed for inorganic-based devices. A clear consequence of this fact, as mentioned in Section 2.1, is that nowadays PV market is widely dominated by inorganic materials. Indeed, probably, OPV materials should not be considered as competitors for inorganic ones, but also as an interesting alternative to enlarge PV application possibilities.

### A.1.1 Semiconducting properties

Semiconducting properties of organic materials are basically related to the carbon bounds in their molecules. Interactions between double and triple bounds split the 2p energy levels in the so called  $\pi$  (bounding) and  $\pi^*$  (antibounding). Therefore, 2p electrons will occupy HOMO (Highest Occupied Molecular Orbital) level while LUMO (Lowest Unoccupied Molecular Orbital) level will rest without electronic occupation. Thus, as we can observe in Figure A.1, when different carbon atoms are bounded, the formation of the so-called  $\pi$  orbitals results in delocalized electrons which are distributed above and below of the  $\sigma$  bounding plane.

## A.1. Introduction

---

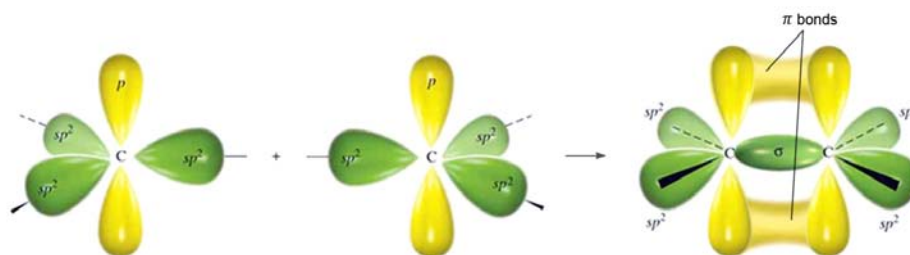


**Figure A.1:** Schematic representation of the  $\pi$ -orbitals formation when different carbon atoms are bounded.

### A.1.2 Morphology: the key feature

In contrast to Inorganic Photovoltaic (IPV) devices, which are based on the junction of a p-type and a n-type layer (see Section 2.1), OPV devices are based on the mixture of a p-type and a n-type component. As mentioned above, one of the most relevant differences between OPV and IPV systems is the value of their exciton binding energy. Inorganic materials evidence a smaller exciton binding energy which results in a rapid exciton dissociation and thus a most effective transfer of electron and holes to their respective electrodes. This is one of the main features that provides a high power conversion efficiency (PCE) to inorganic-based devices. Conversely, organic materials evidence a much higher exciton binding energy, and as illustrated in the detail of Figure A.2, excitons must encounter a high energetic point, for instance the p-n interface, to dissociate. The exciton diffusion length in organic materials is typically in the order of 10-20 nm [3, 4]. Thus, OPV systems must show p-type and n-type phases with a characteristic domain size smaller than the mentioned exciton diffusion length. Once the excitons are dissociated, the resulting electrons and holes have to reach their respective electrodes. Thus, a proper microstructure that allows efficient transport mechanisms between organic molecules is also necessary. For all these reasons, morphologic features related to the phase separation degree, domain size and molecular distribution are key parameters that can highly determine the performance of OPV devices.

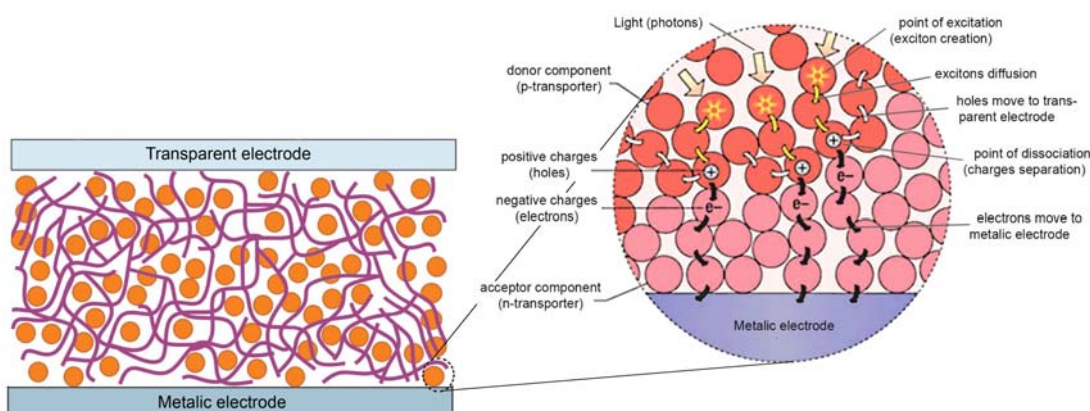


**Figure A.2:** Representation of an OPV thin film microstructure that is formed by a mixture of a p-type and a n-type component. The detail shows the different fundamental steps required to convert incoming photons into electricity.

### A.1.3 Post-deposition annealing treatments

As organic thin films are deposited from solution, molecules crystallize from the melt and appear in a glassy state. In this sense, post-deposition annealing treatments that induce the so-called cold crystallization transition, are one of the most effective methods to enhance the performance and response of organic-based devices [5, 6]. Heating processes lead to the reorganization of polymer molecules causing an increase of the polymer interchain interactions. Thus, the better ordination of molecules and a better  $\pi$ -orbitals overlap induce a higher photon absorption [7] as well as an improvement on charge transport [8]. In this sense, thermally-induced morphological changes such as phase transitions can be considered key phenomena which can have a determinant influence on the final properties and stability of the organic-based devices.

### A.1.4 Geometric confinement

Thermodynamic properties of the thin polymer films formation can be strongly affected by geometric confinement and interface effects. This is, local variations induced by the proximity of the free-surface or the substrate interface can induce changes on molecular mobility and/or molecular packing resulting in changes on the final film morphology. Due to the close link between morphology and device efficiency it is important to study these possible effects, which



would result in morphological differences across the film thickness. The interest on this phenomenon increases steadily due to the fact that most of nowadays advances in organic electronic and photovoltaic technology are based on decreasing length scales of thin films. Several studies have proven that polymer thin films can exhibit different phase transition temperatures depending on film thickness and even across film thickness. For instance, this behavior has also been widely observed in materials such as poly(9,9-dioctylfluorene) (PFO).

### A.1.5 Aim of the study

In the present work, we propose a novel way to study surface vs bulk phase transitions of organic thin films by means of characterizing the crystallization transition temperature of a widely studied luminescent polymer such as poly(9,9-dioctylfluorene) (PFO) and the workhorse system for OPV, namely bulk-heterojunction (BHJ), consisting on poly(3-hexylthiophene) (P3HT) and [6,6]-phenyl C61-butyric acid methyl ester (PCBM) blends. The experimental method proposed here is based on performing in-situ atomic force microscopy (AFM) and Raman spectroscopy measurements during heating of organic thin films in order to characterize the crystallization transition at the surface (probed with AFM) and at the bulk (probed with Raman). AFM measurements are used to study the roughness evolution and the topographic changes suffered by the material surface upon heating which is representative of the crystalline polymeric domain size and thus related to the degree of crystallinity. On the other hand, in-situ Raman scattering experiments are performed in order to analyze the behavior of the molecular interactions of the material in the bulk, which allow the study of thermally-induced morphological changes that are related to phase transitions of the entire film. The close combination of AFM and Raman spectroscopy techniques is expected to be a powerful tool in order to observe morphologic differences between the film surface and the bulk of the film.

## A.2 Methodology

### A.2.1 Sample preparation

Poly(9,9-dioctylfluorene) (PFO) (Sigma-Aldrich) was dissolved in chloroform (CF) (20 g/l) and the resulting solution was stirred overnight in a fume hood. Molecular structure of PFO is depicted in Figure A.3. PFO films were deposited directly onto glass substrates which were ultrasonically cleaned in isopropanol and acetone for 20 minutes and dried under nitrogen flow. Deposition was done by spin-coating at 1500 rpm for 80 s.

Regioregular P3HT (Rieke Metals, 96% of regioregularity) and PCBM (Sigma-Aldrich) were dissolved in chlorobenzene (CB) at a ratio of 1:1 and 1:3 wt/wt. Molecular structure of both materials are depicted in Figure A.3. The solution (40 g/l) was stirred overnight in a fume hood to ensure the complete

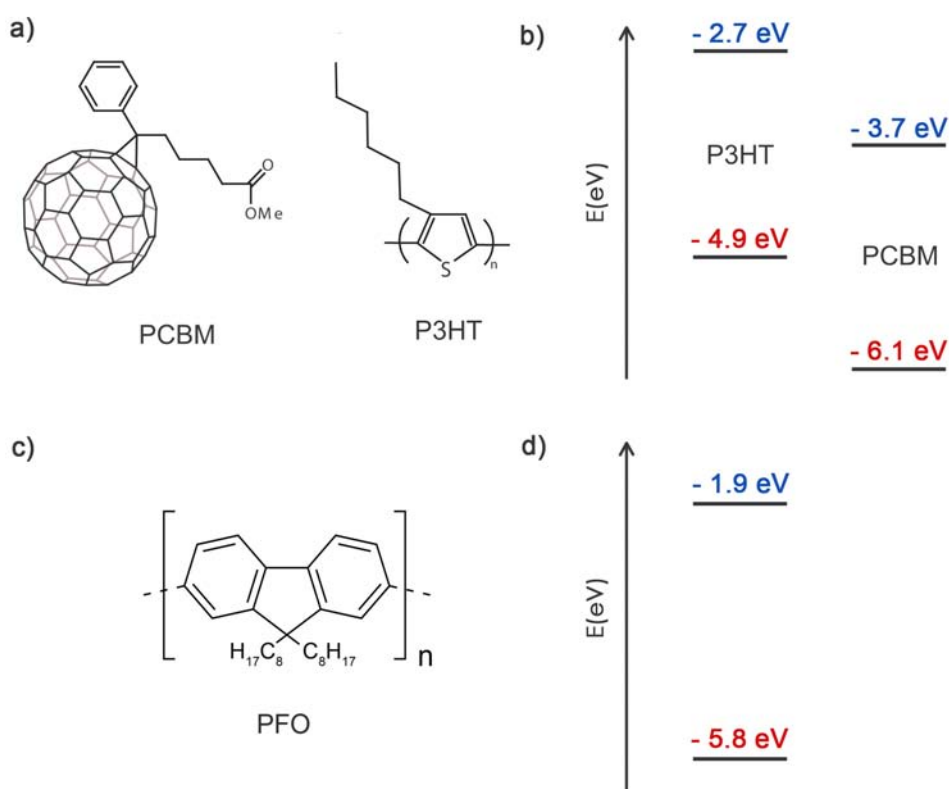


**Figure A.3:** Molecular structures of P3HT, PCBM and PFO (left) and corresponding HOMO and LUMO levels (right).

## A.2. Methodology

dissolution of both components. P3HT:PCBM films were deposited onto three different substrates: glass, Indium Tin Oxide (ITO) coated glass (Vision Tek System) and PEDOT:PSS/ITO/glass. For the last type of substrates, poly(3,4-ethylenedioxythiophene)poly(styrenesulfonate) (PEDOT:PSS) (H. C. Starck) was spin coated onto ITO coated glass substrates before the subsequent polymer: fullerene layer deposition. Glass and ITO/glass substrates were ultrasonically cleaned in isopropanol and acetone for 20 minutes and dried under nitrogen flow. Additionally, for PEDOT:PSS depositions, substrates were also cleaned into an Ultraviolet Ozone (UVO) oven for 30 minutes after the solvent cleaning. PEDOT:PSS layers were spin-coated at 3000 rpm for 60 s and the resulting deposited films were heated at 130 °C for 30 minutes. All P3HT:PCBM layers were spin coated at 2500 rpm for 60 s.

### A.2.2 Experimental techniques

#### A.2.2.1 Temperature-dependent AFM

Temperature-dependent AFM is based on recording conventional topography AFM measurements in real-time during annealing of the sample. As depicted in Figure A.4, heat application during experiments was carried out using a standard hot sample plate in which heat was transferred to the sample through a metallic resistance placed at the center part of the plate where the sample stands on. Temperature-dependent AFM measurements are performed exclu-

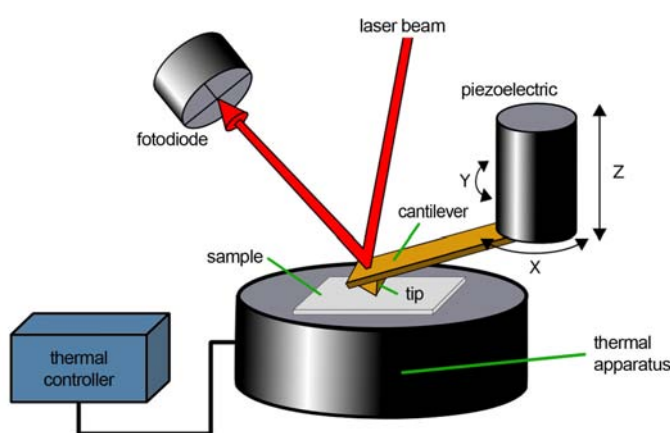


**Figure A.4:** Scheme of the AFM setup for perform in-situ temperature dependent measurements.

sively in this thesis for monitoring phase transition of organic thin films. In particular, by controlling the surface roughness, the recrystallization transition of the material under study can be identified as a result of a drastic increase of the surface roughness. Surface roughness is usually determined by the Root Mean Square (RMS), also known as quadratic mean, of the height variations of the scanned surface area. Thus, in case of a set of  $n$  values  $x_1+x_2+...+x_n$  corresponding to the heights of the different points of the sample surface area, the RMS surface roughness ( $R_{\text{RMS}}$ ) is determined by:

$$R_{\text{RMS}} = \sqrt{\frac{1}{n} (x_1^2 + x_2^2 + \dots + x_n^2)} . \quad (\text{A.1})$$

Temperature-dependent AFM measurements were performed with an Agilent 5500 SPM (Molecular Imaging). In order to diminish the presence of oxygen during heating and hence to avoid material surface oxidation, T-AFM measurements were done in a controlled environmental chamber with rich argon atmosphere. Topographical images were recorded by means of dynamic mode (tapping mode) operation using uncoated Si cantilevers (Nanosensors). A temperature controller (Lakeshore) drives the applied heating ramp which was fixed to 5 degrees/minute. The temperature was kept constant during 5 minutes at each temperature value prior to the data acquisition.

#### **A.2.2.2 Temperature-dependent micro-Raman**

Real-time temperature-dependent Raman spectroscopy measurements were recorded with a LabRam HR 800 Raman spectrometer (Horiba Jobin Yvon). Monochromatic laser light of 514 and 488 nm (2.41 and 2.54 eV, respectively) in wavelength from an  $\text{Ar}^+$  laser were employed for the optical excitation of the sample. Two optical objectives (20x and 50x) were used to focus the laser beam on the sample surface resulting in a diameter spot size of 10 and 4  $\mu\text{m}$  respectively. Heat treatment was performed using exactly the same hot sample plate and the same heating ramp than that employed for the AFM experiments. The sample was located into a home-built silicone cell which was covered with a boron-silicate glass. An argon flow was applied through the cell in order to avoid the appearance of temperature induced oxidation on the illuminated part of the sample surface.

### A.3 PFO films phase transition

PFO is one of the most representative compounds of the polyfluorene family. It presents an excellent charge transport and the possibility of modifying its absorption and emission depending on the microstructure [5]. Figure A.5 depicts the evolution versus temperature of the RMS surface roughness (blue squares) and the normalized Raman intensity of the  $\sim 1603\text{ cm}^{-1}$  peak (green circles). The latter is related to the in-plane stretching vibration of the phenylene rings in the polymer backbone [9]. The data were obtained from real-time AFM and Raman spectroscopy experiments recorded during heating of a spin-coated PFO film deposited onto glass. RMS roughness values which were calculated from  $1.5\text{ }\mu\text{m}^2$  AFM images evidence a significant signal increase between 70 and  $100\text{ }^{\circ}\text{C}$ . As observed in Figure A.6 this local increase of roughness is linked to an increase of crystalline polymer domains size induced by the crystallization transition.

In parallel to RMS roughness increment, peak intensity values that have been calculated from a Gaussian lineshape fit of the Raman data also show a clear increment between 55 and  $100\text{ }^{\circ}\text{C}$  approximately. In agreement with previously reported data [10], simultaneously to the intensity increment, the

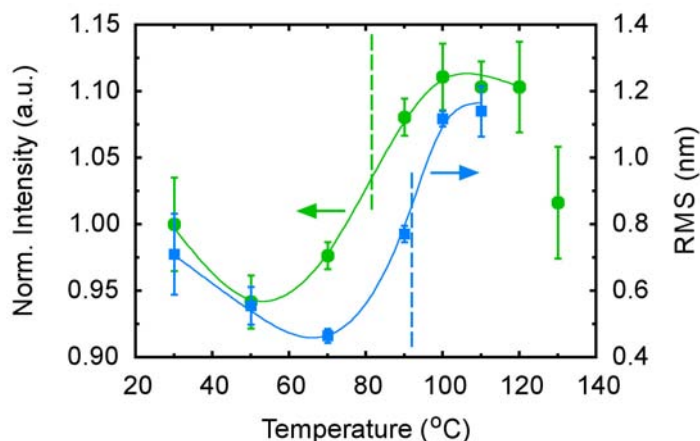


**Figure A.5:** RMS surface roughness evolution (blue squares) and normalized Raman intensity variation of the  $\sim 1603\text{ cm}^{-1}$  peak (green circles) as a function of temperature of a spin coated PFO film. Vertical dashed lines indicate the inflection point (change of the spline slope) of the fitted curve and represent the phase transition temperature.

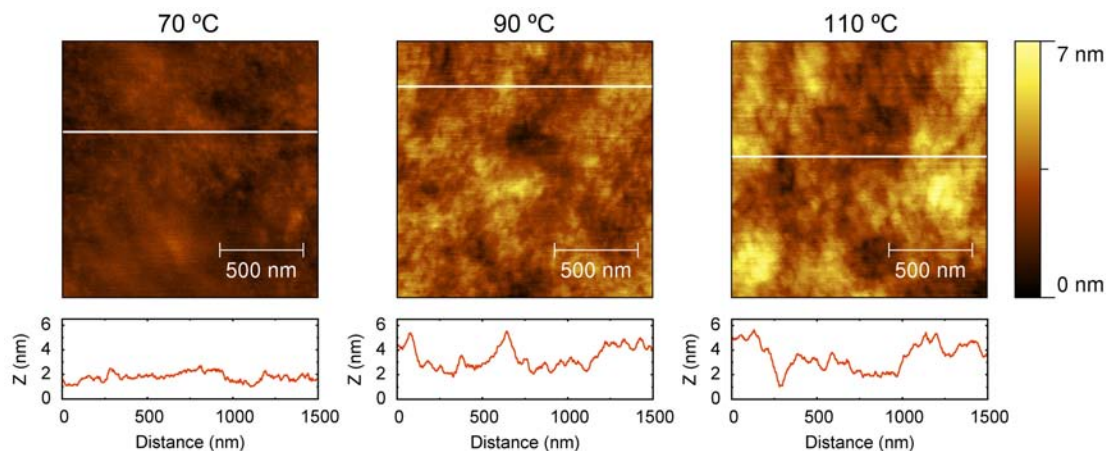


**Figure A.6:** Topography evolution deduced from AFM images obtained at 70, 90 and 110 °C during heating of a PFO film deposited onto a glass substrate. Note that all images are depicted with the same color bar range.

center position (see Table A.1) and the Full Width at Half Maximum (FWHM) of the Raman peak (figure A.7) also suffer changes from 60 until 100 °C. Since PFO is not a highly crystalline system, it shows a relative small Raman frequency shift ( $-1.5 \text{ cm}^{-1}$ ). We will show later that P3HT:PCBM blends which evidence a much higher degree of crystallinity shows a much higher Raman frequency shift upon crystallization. Moreover, note that both Raman peak position (not shown) and intensity values remain constant from 100 until 120 °C where they begin to decrease probably due to the subsequent melt-transition located at 150 °C that begins to affect the microstructural behavior of the material. A downward Raman shift is generally induced by the extension of the effective conjugation length along the polymer backbone [11]. Furthermore, an intensity enhancement of the peaks is associated to a more ordered structure which increases the Raman cross section. Thus, both blue shift and intensity enhancement phenomena are induced by changes in morphology related to the polymer crystallization transition.

In order to find the temperature at which the phase transition takes place splines fitted to the points have been added to the plots. Vertical dashed lines represent the change of the splines slope (inflection point), which we consider the central point of the transition similarly to the peak maxima in Differential Scanning Calorimetry (DSC) experiments. Identification of crystallization transition at around 82 °C by Raman data closely agrees with several previ-

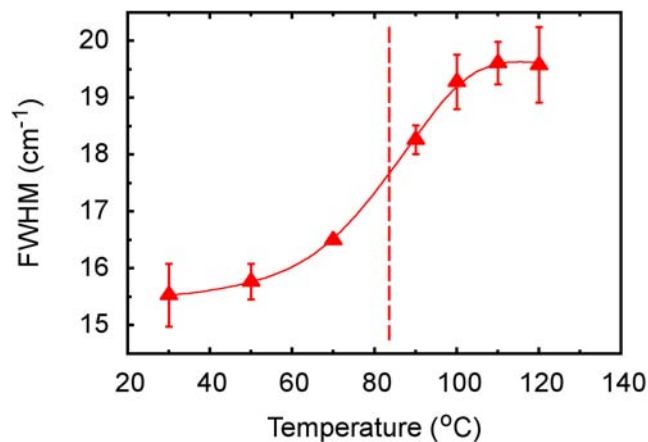


**Figure A.7:** FWHM evolution of the  $\sim 1603 \text{ cm}^{-1}$  Raman peak as a function of temperature during heating of a spin coated PFO film.

ously published values [12, 13, 14] where alternative bulk measurements of the transition temperature including DSC, spectroscopic ellipsometry and photoluminescence (PL), have been employed. This proves that Raman can also be used for this purpose.

The most interesting observation is, perhaps, the existence of a temperature difference of about  $10^\circ\text{C}$  between the crystallization transition point identified by AFM and Raman measurements. Taking into account that AFM characterization provides information about the film surface and Raman spectroscopy probes all the bulk material of the film, the observed temperature difference suggests the existence of a morphology gradient along the film that induces differences on the phase transition temperature between the surface and the bulk. This is also consistent with previous reports that showed by means of ellipsometry experiments that crystallization transition temperature in PFO thin films is highly influenced by the thickness of the film [12].

## A.4 P3HT:PCBM blend films phase transition

To further investigate in other organic material systems the observed differences between the surface and the bulk crystallization transition temperature, we have also carried out real-time AFM and Raman scattering experiments in P3HT:PCBM blend films. The well known 'bulk heterojunction'

(BHJ) based on P3HT:PCBM mixtures [15, 16, 6] is one of the most promising materials for organic solar cells. Regio-regular P3HT acts in the system as the hole-conducting (electron-donor) component which is blended with an electron-conducting (electron-accepting) high soluble fullerene derivative such as PCBM. This binary system features simple eutectic phase behavior [15] resulting in a biphasic microstructure formed by PCBM domains surrounded by a polymer matrix of P3HT crystals.

Figure A.8 shows the topography evolution during heating monitored by real-time AFM measurements of a P3HT:PCBM thin film (1:1 ratio) deposited

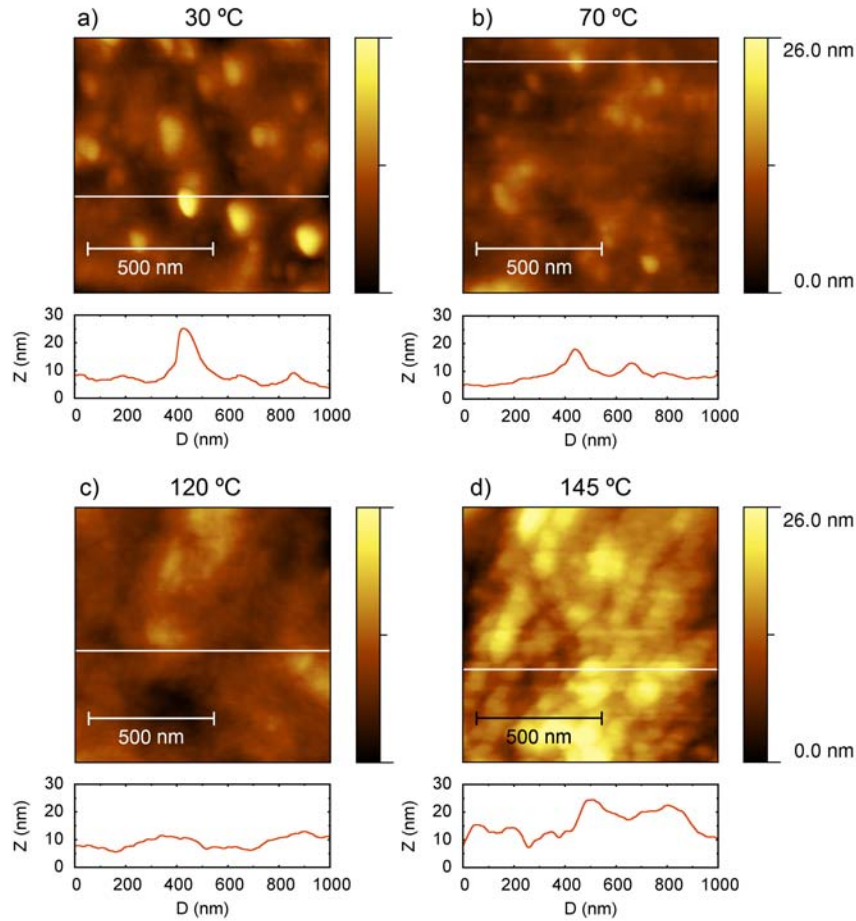


**Figure A.8:** Real-time AFM topography images obtained during heating of a P3HT:PCBM (1:1) blend deposited onto an ITO/glass substrate. All images are presented with the same color bar range.



#### A.4. P3HT:PCBM blend films phase transition

---

onto an ITO/glass substrate. The most relevant and evident change in the sequence is the crystallization of P3HT observed by a clear domain size increase between 120 and 145 °C (images c and d respectively). This is directly related to an increase of the size of the polymer crystals. Polymer crystallization which is considered a key phenomenon for P3HT:PCBM blends, involves the self reorganization of the P3HT molecules, and results in a size enhancement of the P3HT regioregular domains [16]. The higher degree of crystallinity induces a higher interchain molecular interaction that results in more delocalized conjugated  $\pi$  electrons, lowering the band gap and causing a more effective photon absorption [17]. Moreover, the growth of PCBM crystals is also present during the heating-induced molecular reorganization [18] which induces an increase on the electron charge transport capabilities. At low temperature (Figures A.8a and A.8b) surface topography is characterized by well defined spike-like features. Note that topography profile of Figure A.8a shows clearly one of these spike-like features. Since ITO surface usually evidence randomly distributed abrupt spikes and organic layer was deposited directly onto an ITO coated glass substrate, thin film roughness is clearly influenced by ITO surface features which limit the access to the actual P3HT:PCBM layer topography. At the time that the applied temperature rises, molecular mobility and hence P3HT molecular domains size increase progressively. Thus, P3HT domains become progressively larger until they overcome ITO spikes-induced morphology which completely disappear at 120°C. As we discuss below, the general observation of the crystallization temperature is also confirmed in films deposited directly onto glass (see Figure A.10a).

As done previously for PFO in order to complement AFM data, in-situ Raman spectroscopy experiments on P3HT:PCBM blends have also been performed. Figure A.9 shows Raman spectra recorded using an Ar<sup>+</sup> 488 nm laser line during heating of a P3HT:PCBM film (1:1 ratio) deposited onto an ITO/glass substrate. In order to remove the background and noise contributions of the results, Raman data were fitted using a Gaussian line-shape. Spectra on the left panel show a zoom of the first P3HT characteristic Raman peak ( $\sim 730\text{ cm}^{-1}$ ) which is related to the C-S-C stretching vibration [19, 20]. Spectra on the right side show in detail the second and third P3HT characteristic Raman peaks positioned at  $\sim 1380\text{ cm}^{-1}$  and  $\sim 1450\text{ cm}^{-1}$  which are related to the C-C skeletal stretching vibration and the C=C ring stretching vibration, respectively [19, 20]. Figure A.9 shows that three peaks evidence certain intensity variations but only the C=C ring stretching vibration-related peak suffers

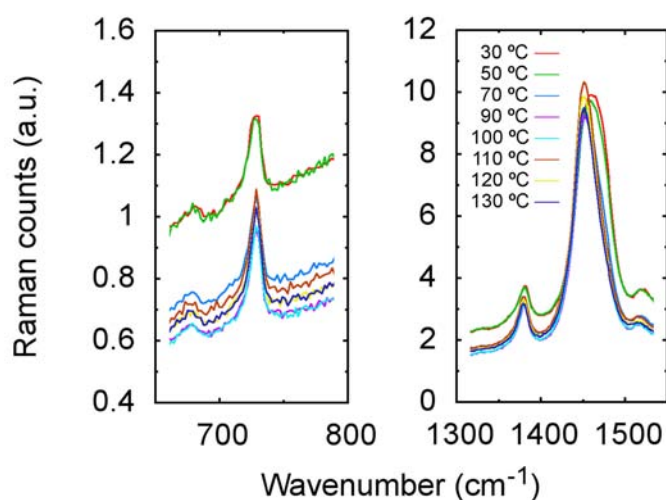


**Figure A.9:** Detail of Raman peaks at  $\sim 730 \text{ cm}^{-1}$  (left),  $\sim 1380 \text{ cm}^{-1}$  and  $\sim 1450 \text{ cm}^{-1}$  (right) recorded with a 488 nm laser line at different temperatures during heating of P3HT:PCBM (1:1) film deposited onto glass substrate.

a significant peak position variation.

Figure A.10 is depicted for comparison of AFM and Raman experiments. On the one hand, Figure A.10a shows the RMS surface roughness evolution of a P3HT:PCBM thin film (1:1 ratio) deposited onto an ITO/glass substrate. On the other hand, Figure A.10b shows the normalized intensity (with respect to its room temperature value) of the  $\sim 1450 \text{ cm}^{-1}$  peak as a function of temperature. RMS roughness evolution sequence was calculated from  $1 \mu\text{m}^2$  AFM images and evidence a clear enhancement from  $140^\circ\text{C}$  approximately, which is induced by P3HT crystallization. Previously to the crystallization transition onset, a constant roughness around 2 nm is observed. As mentioned above, this roughness value remains constant due to the effect of the original ITO surface roughness. In order to confirm the effect of ITO roughness on the layer topography, we have also performed another in-situ AFM experiment of a P3HT:PCBM film deposited directly onto glass. As we can observe on the inset of Figure A.10a, since the effect of the irregular ITO roughness is not present in this case, it is possible to detect a smooth increase on roughness from room temperature until the onset point of the crystallization transition, which is also detected around  $140^\circ\text{C}$ . The vertical dashed line positioned approximately at the middle of the temperature range transition ( $150^\circ\text{C}$ ) is used to estimate the

#### A.4. P3HT:PCBM blend films phase transition

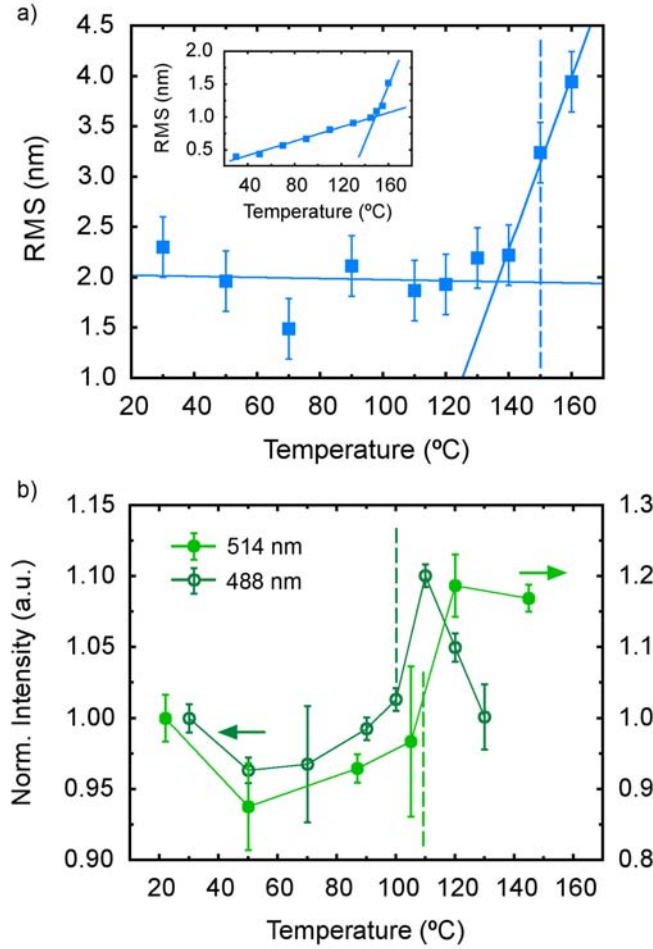


**Figure A.10:** RMS roughness evolution (a) monitored during heating of a spin coated P3HT:PCBM film deposited on ITO/glass. Roughness values were calculated from  $1 \mu\text{m}^2$  AFM images. The inset plot shows the roughness evolution of a P3HT:PCBM film deposited directly on glass. Moreover, the evolution of the normalized intensity of the  $\sim 1450 \text{ cm}^{-1}$  Raman peak (b) as a function of temperature is also represented. The bright green line with filled circles shows the results obtained with a 514 nm laser line excitation, whereas the dark green line with open circles shows the results of using a 488 nm laser line.

phase transition temperature which agrees with C. Muller *et al.* who observed by DSC the crystallization temperature of P3HT:PCBM at  $145^\circ\text{C}$  [15].

In addition, similarly to the PFO case, the Raman signal for P3HT:PCBM films shows a clear intensity enhancement of the C=C stretching vibration related Raman peak as a consequence of the crystallization transition (Figure

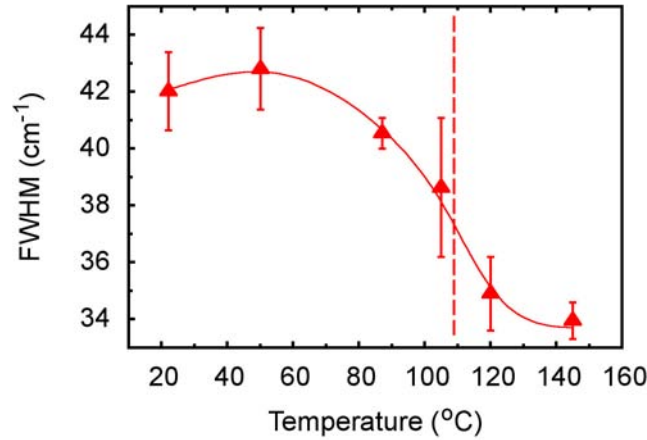


**Figure A.11:** FWHM evolution monitored by Raman during heating of a spin coated P3HT:PCBM film deposited on ITO/glass. The FWHM values were calculated from a Gaussian lineshape fit of the Raman data.

A.10b). As observed in previous studies [21], Raman signal also suffers variations on both peak frequency (see Table A.1) and peak FWHM, as we can observe in Figure A.11. Roughly, a large temperature shift (around 40 °C) is observed between the crystallization transition deduced from AFM and Raman measurements.

Comparing the results shown in Figure A.10b, we observe that the crystallization transition appears at lower temperatures for the experiments that have been performed with the 488 nm laser line. Experiments with the 488 nm laser line were performed on a 1:1 P3HT:PCBM sample and experiments with the 514 nm laser line were made on a 1:3 P3HT:PCBM sample. Since we are using excitation wavelengths which fall at the resonant Raman region and the absorption coefficient is higher in a 1:1 sample ( $13.2 \cdot 10^{-3} \text{ cm}^{-1}$  against  $8.7 \cdot 10^{-3} \text{ cm}^{-1}$  for the 1:3 sample [6]), this slightly lower temperature may be explained by an increased local heating of the material as a consequence of the laser light irradiation. The observed results are qualitatively consistent with this assumption. Another relevant phenomenon observed in the Raman data recorded using the 488 nm line is that after reaching its highest value the peak intensity decreases. This is probably caused by a local sample degradation as a result of an excessive energy absorption by the illuminated organic material. If we now consider the 514 nm data, we observe that the crystallization temperature is determined around 10 °C higher and the peak intensity remains

## A.5. Appendix summary

---

stable once the peak has reached its highest value. Thus, both phenomena evidence that results obtained using the 488 nm laser line are influenced by a laser-induced local heating of the sample. Obviously this local heating is reduced when using the 514 nm wavelength, however we cannot confirm that no local heating occurs in this case. Since optical absorption is reduced and local heating effects are minimized, Raman experiments that use wavelengths at the non-resonant Raman region might be more accurate for the determination of the bulk phase transition temperatures. Consequently, although the shift of about 40 °C observed between the crystallization temperature deduced by AFM and Raman (514 nm) experiments is an upper limit to the real value, this very large observed difference suggests that, as for PFO, films of P3HT:PCBM also exhibit morphologic differences between the surface and the bulk.

## A.5 Appendix summary

With the aim to summarize and compare materials and techniques presented in this work, Table A.1 shows all the key values obtained from the present study. Note that in the case of PFO, in which Raman experiments were made outside the resonant Raman region, the results are consistent and in excellent agreement with literature values. In addition, despite P3HT:PCBM results seem to follow the same tendency than those obtained for PFO, the fact of measuring in the resonant Raman region probably affects the obtained results. The fact that for P3HT:PCBM only the crystallization transition point deduced from roughness of AFM images agrees with literature is qualitatively consistent with this assumption.

In summary, we can conclude that the crystallization transition temperature shift observed by means of in-situ AFM and Raman spectroscopy experiments suggests that bulk and surface morphology evidence differences in relation to parameters like molecular mobility, crystallinity and/or conjugation length. The close relation between morphology and device performance make that the study of this confinement phenomenon observed in organic thin films is of strong interest in order to control the final device efficiency.

	Intensity (arb.units)	Shift ( $\text{cm}^{-1}$ )	FWHM ( $\text{cm}^{-1}$ )	RMS (nm)	$T_{\text{Raman}}$ ( $^{\circ}\text{C}$ )	$T_{\text{AFM}}$ ( $^{\circ}\text{C}$ )	$T_{\text{DSC}}$ ( $^{\circ}\text{C}$ )
PFO as-cast	$15090 \pm 528$	$1604.17 \pm 0.8$	$15.54 \pm 0.54$	$0.71 \pm 0.12$	-	-	-
$\Delta$ PFO transition	$2554 \pm 679$	$-1.63 \pm 1.3$	$6.33 \pm 0.82$	$0.67 \pm 0.05$	$\sim 82$	$\sim 92$	$\sim 85$
P3HT:PCBM as-cast	$2668 \pm 88$	$1460.40 \pm 0.8$	$42.01 \pm 1.39$	$2.30 \pm 0.3$	-	-	-
$\Delta$ P3HT:PCBM transition	$830 \pm 170$	$-9.4 \pm 1.3$	$-8.85 \pm 2.51$	$2.45 \pm 0.6$	$\sim 110$	$\sim 150$	$\sim 145$

**Table A.1:** Values of intensity, frequency shift and FWHM of Raman peaks ( $\sim 1603 \text{ cm}^{-1}$  for PFO and  $\sim 1450 \text{ cm}^{-1}$  for P3HT:PCBM) deduced from real-time Raman experiments, and RMS roughness values obtained from real-time AFM measurements of PFO and P3HT:PCBM thin films during heating. For each material system the Table shows both the as-cast values at room temperature (before the application of heating treatment) and the transition variation values that were calculated from the maximum and minimum values difference during the transition. As shown in Figure A.5, the transition temperatures for PFO have been calculated by the inflection point of the spline fits. We note that P3HT:PCBM data are less precise and probably influenced by external parameters such as local heating due to laser irradiation. Hence, transition temperature values are only illustrative and have been calculated by the middle point of the steeper slope region within the transition range.  $T_{\text{DSC}}$  were obtained from previous reported data [12, 15].

# Bibliography

- [1] G. Dennler, M. C. Scharber, and C. J. Brabec, "Polymer-fullerene bulk-heterojunction solar cells," *Advanced Materials*, vol. 21, pp. 1323–1338, 2009.
- [2] P. W. M. Blom, V. D. Mihailetschi, L. J. A. Koster, and D. E. Markov, "Device physics of polymer:fullerene bulk heterojunction solar cells," *Advanced Materials*, vol. 19, pp. 1551–1566, 2007.
- [3] R. R. Lunt, N. C. Giebink, A. A. Belak, J. B. Benziger, and S. R. Forrest, "Exciton diffusion lengths of organic semiconductor thin films measured by sps spectra resolved photoluminescence quenching," *Journal of Applied Physics*, vol. 105, p. 053711, 2009.
- [4] O. V. Mikhnenko, H. Azimi, M. Scharber, M. Morana, P. W. M. Blom, and M. A. Loi, "Exciton diffusion length in narrow bandgap polymers," *Energy & Environmental Science*, vol. 5, pp. 6960–6965, 2012.
- [5] M. Ariu, D. G. Lidzey, M. Sims, A. J. Cadby, P. A. Lane, and D. D. C. Bradley, "The effect of morphology on the temperature-dependent photoluminescence quantum efficiency of the conjugated polymer poly(9, 9-dioctylfluorene)," *Journal of Physics: Condensed Matter*, vol. 14, pp. 9975–9986, 2002.
- [6] M. Campoy-Quiles, T. Ferenczi, T. Agostinelli, P. G. Etchegoin, Y. Kim, T. D. Anthopoulos, P. N. Stavrinou, D. D. C. Bradley, and J. Nelson, "Morphology evolution via self-organization and lateral and vertical diffusion in polymer:fullerene solar cell blends," *Nature Materials*, vol. 7, pp. 158–164, 2008.
- [7] G. Janssen, A. Aguirre, E. Goovaerts, P. Vanlaeke, J. Poortmans, and J. Manca, "Optimization of morphology of P3HT/PCBM films for organic

- solar cells: Effects of thermal treatments and spin coating solvents," *European Physical Journal - Applied Physics*, vol. 37, pp. 287–290, 2007.
- [8] V. D. Mihailetschi, H. X. Xie, B. deBoer, L. J. A. Koster, and P. W. M. Blom, "Charge transport and photocurrent generation in poly(3-hexylthiophene):methanofullerene bulk-heterojunction solar cells," *Advanced Functional Materials*, vol. 16, pp. 699–708, 2006.
- [9] H. Liem, P. Etchegoin, and D. D. C. Bradley, "Anomalous Raman scattering from the surface of conjugated polymer melts," *Physical Review B*, vol. 64, pp. 1442091–1442095, 2001.
- [10] H. Liem, J. Cabanillas-Gonzalez, P. Etchegoin, and D. D. C. Bradley, "Glass transition temperatures of polymer thin films monitored by Raman scattering," *Journal of Physics: Condensed Matter*, vol. 16, pp. 721–728, 2004.
- [11] B. Tian, G. Zerbi, and K. Mullen, "Electronical and structural properties of polyparaphenylenevinylene from the vibrational spectra," *Journal of Chemical Physics*, vol. 95, pp. 3198–3207, 1991.
- [12] M. Campoy-Quiles, M. Sims, P. G. Etchegoin, and D. D. C. Bradley, "Thickness-dependent thermal transition temperatures in thin conjugated polymer films," *Macromolecules*, vol. 39, pp. 7673–7680, 2006.
- [13] M. Sims, K. Zheng, M. Campoy-Quiles, R. Xia, P. N. Stavrinou, D. D. C. Bradley, and P. Etchegoin, "On the use of optical probes to monitor the thermal transitions in spin-coated poly(9,9-dioctylfluorene) films," *Journal of Physics: Condensed Matter*, vol. 17, pp. 6307–6318, 2005.
- [14] M. Campoy-Quiles, P. G. Etchegoin, and D. D. C. Bradley, "Exploring the potential of ellipsometry for the characterisation of electronic, optical, morphologic and thermodynamic properties of polyfluorene thin films," *Synthetic Metals*, vol. 155, pp. 279–282, 2005.
- [15] C. Muller, T. A. M. Ferenczi, M. Campoy-Quiles, J. M. Frost, D. D. C. Bradley, P. Smith, N. Stingelin-Stutzmann, and J. Nelson, "Binary organic photovoltaic blends: A simple rationale for optimum compositions," *Advanced Materials*, vol. 20, pp. 3510–3515, 2008.
- [16] Y. Kim, S. Cook, S. M. Tuladhar, S. A. Choulis, J. Nelson, J. R. Durrant, D. D. C. Bradley, M. Giles, I. McCulloch, C.-S. Ha, and M. Ree, "A



- strong regioregularity effect in self-organizing conjugated polymer films and high-efficiency polythiophene:fullerene solar cells," *Nature Materials*, vol. 5, pp. 197–203, 2006.
- [17] D. E. Motaung, G. F. Malgas, C. J. Arendse, S. E. Mavundla, C. J. Oliphant, and D. Knoesen, "Thermal-induced changes on the properties of spin-coated P3HT:C<sub>60</sub> thin films for solar cell applications," *Solar Energy Materials and Solar Cells*, vol. 93, pp. 1674–1680, 2009.
- [18] A. Swinnen, I. Haeldermans, P. Vanlaeke, J. D'Haen, J. Poortmans, M. D'Olieslaeger, and J. V. Manca, "Dual crystallization behaviour of polythiophene/fullerene blends," *European Physical Journal - Applied Physics*, vol. 36, pp. 251–256, 2006.
- [19] S. Miller, G. Fanchini, Y.-Y. Lin, C. Li, C.-W. Chen, W.-F. Su, and M. Chhowalla, "Investigation of nanoscale morphological changes in organic photovoltaics during solvent vapor annealing," *Journal of Materials Chemistry*, vol. 18, pp. 306–312, 2008.
- [20] Y.-C. Huang, Y.-C. Liao, S.-S. Li, M.-C. Wu, C.-W. Chen, and W.-F. Su, "Study of the effect of annealing process on the performance of P3HT/PCBM photovoltaic devices using scanning-probe microscopy," *Solar Energy Materials and Solar Cells*, vol. 93, pp. 888–892, 2009.
- [21] J.-J. Yun, J. Peet, N.-S. Cho, G. C. Bazan, S. J. Lee, and M. Moskovits, "Insight into the Raman shifts and optical absorption changes upon annealing polymer/fullerene solar cells," *Applied Physics Letters*, vol. 92, p. 251912, 2008.



# List of publications

## Referred journal papers

- [1] A. Roigé, M. Campoy-Quiles, J. O. Ossó, M. I. Alonso, L. F. Vega, and M. Garriga, *Surface vs bulk phase transitions in semiconducting polymer films for OPV and OLED applications*, Synthetic Metals, **161**, pp. 2570-2574, 2012.
- [2] A. Roigé, J. Fernández-Tejero, J. O. Ossó, A. R. Goni, I. Martín, C. Voz, R. Alcubilla, and L. F. Vega, *On the observation of electron-hole liquid luminescence under low excitation in Al<sub>2</sub>O<sub>3</sub>-passivated c-Si wafers*, Physica Status Solidi RRL, **14**, p.112, 2014.
- [3] A. Roigé, J. Álvarez, J.-P. Kleider, I. Martín, R. Alcubilla, and L. F. Vega, *Microscale spatially-resolved characterization of highly-doped regions in laser-fired contacts for high-efficiency crystalline Si solar cells*, submitted to the IEEE Journal of Photovoltaics.
- [4] A. Roigé, J. O. Ossó, I. Martín, C. Voz, P. Ortega, R. Alcubilla, and L. F. Vega, *Accurate determination of passivation reduction and recombination velocity in c-Si solar cell laser fired base contacts*, submitted to Solar Energy Materials and Solar Cells.

## Conference contributions

A. Roigé, J. O. Ossó, M. Campoy-Quiles, and L. F. Vega, *Nanoscale in-situ characterization of thermally-induced morphological changes of polymer:fullerene thin films during annealing*, In E-MRS Spring Meeting, Poster contribution, May 9-13, 2011, Nize (France)

A. Roigé, J. O. Ossó, C. Voz, R. Alcubilla, and L. F. Vega, *Kelvin probe force microscopy for photovoltaic materials characterization*, In CFN Summer School on Nano-Energy (Karlsruhe Institute of Technology), Poster contribution, September 14-17, 2012, Bad Herrenalb (Germany)

A. Roigé, J. O. Ossó, I. Martín, C. Voz, P. Ortega, R. Alcubilla, and L. F. Vega, *Towards the optimization of laser fired contacts by the microscale characterization of the laser-induced local impact*, In 29<sup>th</sup> European Photovoltaic Solar Energy Conference (EUPVSEC), Poster contribution, September 22-26, 2014, Amsterdam (The Netherlands).

## List of acronyms

a-Si	amorphous-Silicon
AFM	Atomic Force Microscopy
ALD	Atomic Layer Deposition
AM	Amplitude Modulation
AR	Anti-Reflection
BE	Bound Exciton
BHJ	Bulk-Heterojunction
BSF	Back Surface Field
c-AFM	conductive-Atomic Force Microscopy
c-Si	crystalline-Silicon
CB	Conduction Band
CCD	Charge-Coupled Device
CPD	Contact Potential Difference
C-V	Capacitance-Voltage
CW	Continuous Wave
DSC	Differential Scanning Calorimetry
EDX	Energy-Dispersive X-ray
EHL	Electron-Hole Liquid
FB	Free-Bound
FE	Free Exciton
FSF	Front Surface Field
FWHM	Full Width at Half Maximum

FZ	Float-Zone
GHGs	Green House Gases
HBD	Highly-Boron Doped
HF	Hydrofluoric acid
HOMO	Highest Occupied Molecular Orbital
HV	High-Vacuum
ICs	Integrated Circuits
IR	Infra-Red
ITO	Indium Tin Oxide
I-V	Intensity-Voltage
KPFM	Kelvin Probe Force Microscopy
LFCs	Laser Fired Contacts
LUMO	Lowest Unoccupied Molecular Orbital
MFM	Magnetic Force Microscopy
MOS	Metal-Oxide-Semiconductor
MOSFET	Metal-Oxide-Semiconductor Field-Effect Transistor
NA	Numerical Aperture
OLED	Organic Light Emitting Diode
OPV	Organic Photovoltaic
OSC	Organic Solar Cell
PC	Photo-Conductance
PCE	Power Conversion Efficiency
PECVD	Plasma Enhanced Chemical Vapor Deposition
PERC	Passivated Emitter and Rear Cell
PERL	Passivated Emitter and Rear Locally-diffused
PL	Photoluminescence
PV	Photovoltaic
QSSPC	Quasi Steady State Photo-Conductance
RMS	Root Mean Square
SEM	Scanning Electron Microscopy
SHG	Second Harmonic Generation

## List of acronyms

---

SNOM	Scanning Near-field Optical Microscopy
SOI	Silicon-On-Insulator
SP	Surface Potential
SPM	Scanning Probe Microscopy
SRH	Schockley Read Hall
SRV	Surface Recombination Velocity
SSL	Solid-State Laser
STM	Scanning Tunneling Microscopy
TA	Transverse-Acoustical
T-AFM	Temperature-dependent Atomic Force Microscopy
TO	Transverse-Optical
UV	Ultra-Violet
UVO	Ultra-Violet Ozone
VB	Valence Band





# List of symbols

$A_{mc}$	Amplitude of multi-crystalline Si Raman peak
$\alpha$	Absorption coefficient
$B$	Radiative recombination coefficient ( $1 \times 10^{-14}$ - $5 \times 10^{-15} \text{ cm}^3 \text{ s}^{-1}$ )
$C$	Capacitance
$C_{ox}$	Oxide capacitance
$C_n, C_p$	Electron and hole Auger coefficients
$\chi$	Electron affinity
$D$	Accumulation region depth
$D_e$	Electron diffusion coefficient
$D_{it}$	Energy-dependent interface trap density
$d$	Electron-hole liquid depth
$E_a$	Transition activation energy
$E_{BE}$	Bound-Exciton transition energy
$E_{bx}$	Bound-Exciton binding energy
$E_F$	Fermi level energy
$E_{Fp}$	Quasi-Fermi level energy of holes
$E_{FB}$	Free-Bound transition energy
$E_{FE}$	Free-Exciton transition energy
$E_g$	Band gap
$E_i$	Intrinsic energy level
$E_t$	Energy level of a defect
$E_{VAC}$	Vacuum level energy

$E_x$	Exciton binding energy
$\eta_{PL}$	PL efficiency
$f_{abs}$	Fraction of absorbed irradiation photons
$f_c$	Contacted area fraction
$G$	Generation rate
$\Gamma$	Full width at half maximum of Raman peak
$I_{av}$	Averaged illumination intensity
$I_{PL}$	Photoluminescence intensity
$I_{ram}$	Raman intensity
$k_B$	Boltzmann constant ( $8.617 \times 10^{-5}$ eV K <sup>-1</sup> )
$L_{length}$	Charge carrier diffusion length
$\lambda$	Wavelength
$\mu_n, \mu_p$	Electron and hole mobilities
$N_A, N_D$	Donor and acceptor densities
$N_t$	defect concentration per unit volume
$N_{st}$	defect concentration per unit area
$n_i$	Intrinsic carrier densities
$n, p$	Electron and hole densities
$n_0, p_0$	Electron and hole densities at equilibrium
$n_s, p_s$	Electron and hole densities at the surface
$\Delta n, \Delta p$	Electron and hole excess carrier density (since $\Delta n = \Delta p$ , $\Delta n$ is often used for both cases)
$p$	Pitch between laser-fired contacts
$\Phi$	Photon flux
$\varphi_F$	Fermi potential
$\varphi_{metal}$	Metal work function
$\varphi_{ms}$	Metal-semiconductor work function difference
$\varphi_s$	Band bending
$\varphi_{sample}$	Sample work function
$\varphi_{sc}$	Semiconductor work function
$\varphi_{tip}$	AFM tip work function

## List of symbols

---

$Q_{\text{eff}}$	Effective oxide charge
$Q_f$	Fixed charge density
$Q_g$	Gate charge
$Q_m$	Mobile charge density
$Q_t$	Trapped charge density
$q$	fundamental charge
$q_F$	Fano asymmetry parameter
$R_{\text{RMS}}$	Root mean square of surface roughness
$R_s$	Base series resistance
$R_f$	Wafer reflectivity
$r$	Radius of laser-fired contacts
$\rho$	Wafer resistivity
$\rho_c$	Critical density for electron-hole liquid condensation
$S$	Surface recombination velocity
$S_0$	Surface recombination velocity at the non-processed front surface
$S_{\text{cont}}$	Surface recombination velocity at the laser-fired contacts
$S_{\text{eff}}$	Effective surface recombination velocity
$S_{n0}, S_{p0}$	Fundamental surface recombination velocities of electrons and holes
$S_{\text{pas}}$	Surface recombination velocity at the surface non-processed by laser
$S_{\text{rear}}$	Surface recombination velocity at the laser-processed rear surface
$S_{\text{sur}}$	Surface recombination velocity at the contact vicinity affected by laser-processing
$\Delta\sigma$	Photo-conductance
$\sigma_n, \sigma_p$	Defect capture cross-sections of electron and holes
$T$	Temperature
$\tau$	Lifetime
$\tau_{\text{Aug}}$	Auger recombination lifetime
$\tau_{\text{bulk}}$	Bulk lifetime
$\tau_{\text{eff}}$	Effective lifetime
$\tau_{\text{exc}}$	Exciton lifetime
$\tau_{\text{int}}$	Intrinsic lifetime

$\tau_{\text{rad}}$	Radiative recombination lifetime
$\tau_{\text{s}}$	Lifetime at the surface
$\tau_{\text{SRH}}$	Recombination via defects lifetime
$U$	Recombination rate
$U_{\text{Aug}}$	Auger recombination rate
$U_{\text{bulk}}$	Bulk recombination rate
$U_{\text{eff}}$	Effective recombination rate
$U_{\text{rad}}$	Radiative recombination rate
$U_{\text{s}}$	Recombination rate at the surface
$U_{\text{SRH}}$	Recombination rate via defects
$V_{\text{CPD}}$	Contact potential difference electrostatic force
$V_{\text{fb}}$	Flat-band voltage
$V_{\text{fb0}}$	Ideal Flat-band voltage (without oxide charge effect)
$V_{\text{g}}$	Gate voltage
$V_{\text{th}}$	Threshold voltage
$v_{\text{th}}$	thermal velocity of charge carriers
$W$	Wafer thickness
$w$	Raman frequency
$w_{\text{cm}}$	Frequency of the Raman peak center of mass
$w_{\text{mc}}$	Frequency of the multi-crystalline Raman peak maximum
$w_{\text{max}}$	Frequency of the Raman peak maximum